

**INFLUENCE OF ROTATING TIRE DYNAMICS ON
VEHICLE SYSTEM VIBRATIONS**

KHODABAKHSH SAEEDI

A THESIS

IN THE DEPARTMENT OF

MECHANICAL AND INDUSTRIAL ENGINEERING

PRESENTED IN PARTIAL FULFILLMENT OF THE REQUIREMENTS

FOR THE DEGREE OF DOCTOR OF PHILOSOPHY AT

CONCORDIA UNIVERSITY

MONTREAL, QUEBEC, CANADA

AUGUST 2012

© KHODABAKHSH SAEEDI, 2012

CONCORDIA UNIVERSITY
SCHOOL OF GRADUATE STUDIES

This is to certify that the thesis prepared

By: **Khodabakhsh Saeedi**

Entitled: **Influence of Rotating Tire Dynamics on Vehicle System Vibrations**

and submitted in partial fulfillment of the requirements for the degree of

DOCTOR OF PHILOSOPHY (Mechanical Engineering)

complies with the regulations of the University and meets the accepted standards with respect to originality and quality.

Signed by the final examining committee:

_____ Chair
Dr. A. Hanna

_____ External Examiner
Dr. D. Necsulescu

_____ External to Program
Dr. A. Aghdam

_____ Examiner
Dr. J. Dargahi

_____ Examiner
Dr. R. Sedaghati

_____ Thesis Supervisor
Dr. R.B. Bhat

Approved by _____
Dr. A. Dolatabadi, Graduate Program Director

August 6, 2012

Dr. Robin A.L. Drew, Dean
Faculty of Engineering and Computer Science

ABSTRACT

Influence of Rotating Tire Dynamics on Vehicle System Vibrations

Khodabakhsh Saeedi

Concordia University, 2012

In the present study, a new two-dimensional hybrid quarter-car model has been developed. The hybrid model takes into account the inertia of the discrete vehicle body mounted on suspension and the dynamics of the rotating tire modeled as a continuous ring. The contact force between the tire and road is defined as a function of the bounce vibration of the vehicle as well as a function of the radial and tangential displacements and accelerations of the tire. The effects of the vibrating system on the contact force are investigated. Three different types of solution are presented: the Galerkin method, the finite element method, and the exact analytical method. Different solutions are used to validate the accuracy of the results. The mode shapes of the center-fixed rotating ring are used as admissible functions in the Galerkin method. In the finite element method, a curved beam is used as the element. The equations are derived in a non-rotating coordinate system. In other words, the nodes do not rotate. However, the material of the ring does rotate by flowing through the non-rotating nodes. The analytical study presents the closed-form solutions of the horizontal displacement and of the vertical displacement of the center of the tire (unsprung mass) as well as the displacement of the vehicle body (sprung mass). This method also provides the radial displacement and the tangential

displacement of the rotating ring in the non-rotating coordinate system, all the displacements of the ring being measured with respect to the center of the ring. The results obtained by the different methods are compared and discussed. The natural frequencies of this hybrid system are compared with those obtained for a center-fixed ring. Also the damped frequencies of the system are obtained for different velocities of the vehicle. The mode shapes of the hybrid model are complex because of the rotating tire. Moreover, the response of the hybrid model to the random excitation caused by the road is studied. Results show that the rotation of the tire and the bounce vibration of the vehicle body affect the dynamic forces at the contact point. These results are compared with those of the conventional 2-DOF quarter-car model.

ACKNOWLEDGEMENTS

This research would not have been possible without the support of many people. I would like to express my gratitude to my supervisor, Dr. Rama B. Bhat, whose expertise, understanding, and patience added considerably to my graduate experience. I appreciate his vast knowledge and skill in many areas, and his assistance in writing this thesis.

I would like to thank the other members of my committee, Dr. Ramin Sedaghati, Dr. Javad Dargahi, Dr. Amir Aghdam, and Dr. Dan Neculescu for the assistance they provided at all levels of the research project.

I would also like to acknowledge the collaboration of my friends in the CONCAVE Research Center, particularly the assistance of Dr. Mohammad Saber Fallah in modeling the McPherson suspension system and the generous spirit of Mr. Raghdan Alkhoury, who contributed to the debates and the exchanges of knowledge and skills during the earlier stages of the research.

I would like to express my love and gratitude to my beloved family for the support they have provided me throughout my entire life. In particular, I would also like to acknowledge the understanding and endless love of my wife Nafiseh, throughout the duration of my studies.

I would also like to thank Mr. B. Peterson for his editing assistance. He helped me continuously in writing papers, reports, and the thesis. Appreciation also goes to my employer, Mr. M. Kahrobaei. He taught me how to handle the projects flexibly and to finish them in a timely manner.

In conclusion, I recognize that this research would not have been possible without the financial assistance provided by the School of Graduate Studies at Concordia University (Concordia Graduate Fellowship, Tuition Remission, and Conference and Exposition Award) and that also provided by the Department of Mechanical and Industrial Engineering at Concordia University (Teaching Assistantships, ENCS Graduate Scholarship). I wish to express my deep gratitude to those agencies.

TABLE OF CONTENTS

LIST OF FIGURES -----	ix
LIST OF TABLES-----	xiv
LIST OF SYMBOLS-----	xvi
CHAPTER 1 INTRODUCTION-----	1
1.1. MOTIVATION -----	2
1.2. LITERATURE REVIEW -----	3
Vehicle System -----	3
Tire Dynamics -----	7
Imperfect Ring -----	21
Combined Models -----	23
1.3. OBJECTIVES AND SCOPES -----	26
CHAPTER 2 CENTER-FIXED RING-----	29
2.1. INTRODUCTION -----	29
2.2. FREE VIBRATION OF A CENTER-FIXED RING IN ROTATING COORDINATE SYSTEM -----	30
2.3. FREE VIBRATION OF A CENTER-FIXED RING IN NON-ROTATING COORDINATE SYSTEM -----	38

2.4. CONCLUDING REMARKS-----	45
CHAPTER 3 HYBRID QUARTER-CAR MODEL-----	47
3.1. INTRODUCTION -----	47
3.2. MODELING-----	48
3.3. SUMMARY -----	55
CHAPTER 4 APPROXIMATE SOLUTIONS BY GALERKIN METHOD AND FEM-----	57
4.1. INTRODUCTION -----	57
4.2. GALERKIN SOLUTION-----	58
4.3. FINITE ELEMENT METHOD-----	72
4.4. CONCLUDING REMARKS-----	81
CHAPTER 5 ANALYTICAL SOLUTION OF THE HYBRID MODEL -----	82
5.1. INTRODUCTION -----	82
5.2. METHODOLOGY OF ANALYTICAL SOLUTION -----	83
5.3. FREE VIBRATION RESPONSE-----	90
5.4. CONCLUDING REMARKS-----	107
CHAPTER 6 VEHICLE RESPONSE TO ROAD EXCITATION-----	108
6.1. INTRODUCTION -----	108
6.2. MODAL ANALYSIS -----	109
6.3. RANDOM VIBRATION ANALYSIS -----	114
6.4. CONCLUDING REMARKS-----	130
CHAPTER 7 CONCLUSIONS AND SUGGESTIONS FOR FUTURE STUDIES -----	131
7.1. SUMMARY -----	131
7.2. SUGGESTIONS FOR FUTURE STUDIES -----	137
REFERENCES-----	140

LIST OF FIGURES

Figure 2.1: Schematic of the 2-D model of a tire: ring rotating about a fixed center.....	30
Figure 2.2: The bifurcating natural frequencies (less than 2000 <i>rad/s</i>) of the center-fixed ring in the rotating system of coordinates vs. different angular velocities.	36
Figure 2.3: The bifurcating natural frequencies (higher than 2000 <i>rad/s</i>) of the center-fixed ring in the rotating system of coordinates vs. different angular velocities.....	37
Figure 2.4: The bifurcating natural frequencies (less than 2000 <i>rad/s</i>) of the center-fixed ring in the non-rotating system of coordinates vs. different angular velocities.....	43
Figure 2.5: The bifurcating natural frequencies (higher than 2000 <i>rad/s</i>) of the center-fixed ring in the non-rotating system of coordinates vs. different angular velocities.....	44
Figure 2.6: The radial displacement of a center-fixed ring for $n=0$ (left) and for $n=2$ (right)	45
Figure 3.1: Schematic of a 2-D model of a vehicle: a rotating ring with the center that moves horizontally and vertically.....	49
Figure 3.2: The undeformed ring (left) and the deformed ring with a free center (right)	50

Figure 4.1: Schematic of a McPherson suspension system	62
Figure 4.2: The convergence rate of the natural frequencies of a hybrid quarter-car model with a non-rotating ring vs. the number of functions applied in the Galerkin method (frequencies lower than 1000 <i>rad/s</i>)	67
Figure 4.3: The convergence rate of the natural frequencies of a hybrid quarter-car model with a non-rotating ring vs. the number of functions applied in the Galerkin method (frequencies higher than 1000 <i>rad/s</i>)	68
Figure 4.4: The convergence rate of the natural frequencies of a quarter-car model with a rotating ring $\bar{\omega}=100$ <i>rad/s</i> vs. the number of functions applied in the Galerkin method (frequencies lower than 1000 <i>rad/s</i>)	70
Figure 4.5: The convergence rate of the natural frequencies of a quarter-car model with a rotating ring $\bar{\omega}=100$ <i>rad/s</i> vs. the number of functions applied in the Galerkin method (frequencies higher than 1000 <i>rad/s</i>)	71
Figure 4.6: A curved beam element for the circular ring.....	73
Figure 5.1: The schematic of a 2-D model of a vehicle: Forces and moments at the contact area	84
Figure 5.2: The natural frequencies of the hybrid quarter-car model for different angular velocities of the ring.....	93
Figure 5.3: Comparison of the natural frequencies obtained by using different methods (a) non rotating ring (b) rotating ring $\bar{\omega}=100$ <i>rad/s</i>	94
Figure 5.4: The first mode of the hybrid quarter-car model with a non-rotating tire. The radial displacement of tire U (top) and the tangential displacement of tire V (below). $\omega=8.3803$ <i>rad/s</i> , $Z_s=-4.552$, $Z_u=-1$, $X_u=0$	96

Figure 5.5: The second mode of the hybrid quarter-car model with a non-rotating tire. The radial displacement of the tire U (top) and the tangential displacement of tire V (below). $\omega=52.7044 \text{ rad/s}$, $Z_s=0.0335$, $Z_u=-1$, $X_u=0$ 98

Figure 5.6: The third mode of the hybrid quarter-car model with a non-rotating tire. The radial displacement of tire U (top) and the tangential displacement of tire V (below). $\omega=140.0543 \text{ rad/s}$, $Z_s=0$, $Z_u=0$, $X_u=0.1783$ 99

Figure 5.7: The fourth mode of the hybrid quarter-car model with a non-rotating tire. The radial displacement of the tire U (top) and the tangential displacement of the tire V (below). $\omega=282.2011 \text{ rad/s}$, $Z_s=3.5357 \times 10^{-5}$, $Z_u=-0.0313$, $X_u=-2.1152 \times 10^{-8}$ 100

Figure 5.8: The first mode of the hybrid quarter-car model with a rotating tire $\bar{\omega}=100 \text{ rad/s}$. The radial displacement U (top) and tangential displacement V (below). $\omega=8.4712 \text{ rad/s}$, $Z_s=-4.9300-0.2114i$, $Z_u=-0.9991-0.0428i$, $X_u \approx 0$ 101

Figure 5.9: The imaginary parts of the displacements of the rotating ring at the first mode $\bar{\omega}=100 \text{ rad/s}$. $\omega=8.4712 \text{ rad/s}$ radial displacement (left) and tangential displacement (right) 102

Figure 5.10: The second mode of the hybrid quarter-car model with a rotating tire $\bar{\omega}=100 \text{ rad/s}$. The real and imaginary parts of the radial displacement of the ring U (top) and real and imaginary parts of the tangential displacement of the ring V (below). $\omega=54.7260 \text{ rad/s}$, $Z_s=0.0298 + 0.0085i$, $Z_u=-0.9618 - 0.2736i$, $X_u=-0.0021 + 0.0072i$ 103

Figure 5.11: The third mode of the hybrid quarter-car model with a rotating tire $\bar{\omega}=100 \text{ rad/s}$. The real and imaginary parts of the radial displacement of the ring U (top) and the real and imaginary parts of the tangential displacement of the ring V (below).

$\omega=134.5266 \text{ rad/s}$, $Z_s=1.6857 \times 10^{-5} - 8.7983 \times 10^{-6}i$, $Z_u= -0.0034 + 0.0018i$, $X_u= -0.1028 - 0.1970i$ 104

Figure 5.12: The fourth mode of the hybrid quarter-car model with a rotating tire $\bar{\omega}=100 \text{ rad/s}$. The real and imaginary parts of the radial displacement U (top) and the real and imaginary parts of the tangential displacement V (below). $\omega=283.9394 \text{ rad/s}$,

$Z_s=5.5252 \times 10^{-6} - 3.8434 \times 10^{-5}i$, $Z_u= - 0.0049 - 0.0344i$, $X_u= -0.0061 + 0.0009i$ 105

Figure 5.13: the fifth mode of the hybrid quarter-car model with a rotating tire $\bar{\omega}=100 \text{ rad/s}$. The real and imaginary parts of the radial displacement U (top) and the real and imaginary parts of the tangential displacement V (below). $\omega= 416.7889 \text{ rad/s}$, $Z_s=$

$1.3268 \times 10^{-6} - 2.7162 \times 10^{-6}i$, $Z_u=-0.0026 + 0.0052i$, $X_u=-0.0033 - 0.0016i$ 106

Figure 6.1: Schematic of a hybrid quarter-car model of a vehicle subjected to road roughness 109

Figure 6.2: The spectral density of road roughness experienced by a passenger of a vehicle moving at $v= 69 \text{ km/h}$ and tire angular velocity $\bar{\omega}=60 \text{ rad/s}$ 115

Figure 6.3: The spectral density of the vertical contact force of the hybrid quarter-car model..... 117

Figure 6.4: The spectral density of the vertical contact force of a 2-DOF quarter-car model..... 118

Figure 6.5: The spectral density of the horizontal contact force of the hybrid quarter-car model..... 119

Figure 6.6: The spectral density of the vertical displacement of the center of tire for the hybrid quarter-car model..... 120

Figure 6.7: The spectral density of the vertical displacement of the unsprung mass (center of tire) for the 2DOF quarter-car model	121
Figure 6.8: The spectral density of the horizontal displacement of the center of the tire for the hybrid quarter-car model.....	122
Figure 6.9: The spectral density of the vertical displacement of the passenger for the hybrid quarter-car model.....	125
Figure 6.10: The spectral density of the vertical displacement of the passenger for the traditional 2DOF quarter-car model.....	126
Figure 6.11: The spectral density of the vertical acceleration of the passenger for the hybrid quarter-car model.....	127
Figure 6.12: The spectral density of the vertical acceleration of the passenger for the traditional 2-DOF quarter-car model	128
Figure 7.1: Schematic of a 2-D model of a vehicle. The contact area is assumed as a beam	138
Figure 7.2: Two rotating tires combined with the vehicle body and the suspension system of the vehicle.....	139

LIST OF TABLES

Table 2.1: The natural frequencies of a non-rotating center-fixed ring.....	33
Table 2.2: The natural frequencies of a center-fixed ring rotating with angular velocity $\bar{\omega}=100 \text{ rad/s}$ in the rotating coordinate system.....	33
Table 2.3: The natural frequencies of a center-fixed ring rotating with an angular velocity $\bar{\omega}=100 \text{ rad/s}$ in the non-rotating coordinate system	40
Table 4.1: The natural frequencies of the hybrid quarter-car model with a non-rotating ring $\bar{\omega}=0$ for the different number of functions employed in the Galerkin Method.....	66
Table 4.2: The natural frequencies of the hybrid quarter-car model with a rotating ring with $\bar{\omega}=100 \text{ rad/s}$, for a different number of functions employed in the Galerkin Method	69
Table 4.3: The natural frequencies of the hybrid quarter-car model with a non-rotating ring ($\bar{\omega}=0$) obtained by FEA.....	79
Table 4.4: The natural frequencies of the hybrid quarter-car model with a rotating ring ($\bar{\omega}=100 \text{ rad/s}$) obtained by FEA.....	80

Table 5.1: The natural frequencies of the hybrid quarter-car model at different angular velocities	91
Table 5.2 The conversion of the angular velocity of the tire to the forward speed of the vehicle.....	91
Table 6.1: Comparison of the damped frequencies of the hybrid quarter-car model at different velocities	113
Table 6.2: Comparison of the mean value of the responses to road excitation at different velocities	129

LIST OF SYMBOLS

Symbols	Descriptions	Units
<i>A</i>	<i>Area of the Cross Section of the Ring</i>	m^2
C	<i>Damping Matrix</i>	
<i>E</i>	<i>Modulus of Elasticity of the Tire Material</i>	<i>Pa</i>
$E(T_x)$	<i>Mean Square of Horizontal Contact Force between the Tire and the Road</i>	N^2
$E(T_z)$	<i>Mean Square of Vertical Contact Force between the Tire and the Road</i>	N^2
$E(X_u)$	<i>Mean Square of Horizontal Displacement of Tire Center</i>	m^2
$E(Z_u)$	<i>Mean Square of Vertical Displacement of Tire Center</i>	m^2
$E(Z_s)$	<i>Mean Square of Horizontal Displacement Force between the Tire and the Road</i>	m^2

$H_{Tz}(\omega)$	<i>Frequency Response of Vertical Force to Harmonic Road Excitation</i>	N/m
I	<i>Second Moment of the Area ring Cross Section</i>	m^4
K	<i>Kinetic energy of the Hybrid Quarter Car Model</i>	J
L_0	<i>Initial Length of Suspension Spring at McPherson Suspension System</i>	m
L	<i>Length of Stretched Suspension Spring at McPherson Suspension System</i>	m
\mathbf{K}	<i>Stiffness Matrix</i>	
\mathbf{M}	<i>Mass Matrix</i>	
N	<i>Number of Elements in Finite Element Analysis</i>	
\hat{N}	<i>Number of Admissible Functions in the Galerkin Method</i>	
N_0	<i>Initial tension caused by rotation and inflation pressure on the circumference of the ring</i>	N
P	<i>Potential Energy of the Hybrid Quarter Car Model</i>	J
$S(T_x)$	<i>Spectral Density of Horizontal Contact Force between the Tire and the Road</i>	N^2s
$S(T_z)$	<i>Spectral Density of Vertical Contact Force between the Tire and the Road</i>	N^2s
$S(X_u)$	<i>Spectral Density of Horizontal Displacement of Tire Center</i>	m^2s
$S(Z_u)$	<i>Spectral Density of Vertical Displacement of Tire Center</i>	m^2s
$S(Z_s)$	<i>Spectral Density of Horizontal Displacement Force between the Tire and the Road</i>	m^2s
T_x	<i>Horizontal Contact Force between the Tire and the Road</i>	N
T_x	<i>Vertical Contact Force between the Tire and the Road</i>	N

U	<i>Radial displacement of the Ring</i>	m
V	<i>Tangential displacement of the Ring</i>	m
$X_u(t)$	<i>Horizontal Displacement of the Tire Center</i>	m
$Z_u(t)$	<i>Vertical Displacement of the Tire Center</i>	m
$Z_s(t)$	<i>Vertical Displacement of the Vehicle Body</i>	m
a	<i>Ring Radius</i>	m
b	<i>Tire Width</i>	m
c	<i>Suspension Damping Coefficient</i>	Ns/m
g	<i>Gravitational Acceleration</i>	m/s^2
h	<i>Ring Thickness</i>	m
k	<i>Stiffness of the Suspension System</i>	N/m
l_c	<i>Length of Control Arm at McPherson Suspension System</i>	m
m_s	<i>Mass of the Vehicle Body (Sprung Mass)</i>	kg
m_w	<i>Mass of the Wheel</i>	kg
p	<i>Tire Inflation Pressure</i>	Pa
t	<i>Time</i>	s
u	<i>Radial Displacement of Tire in Rotating System of Coordinates</i>	m
u_0	<i>Stationary Radial Displacement of Tire</i>	m
v	<i>Tangential Displacement of Tire in Rotating System of Coordinates</i>	m
δ	<i>Variation Operator</i>	
$\delta(\varphi - \varphi_0)$	<i>Dirac delta Function</i>	

θ	<i>Angular Position Defined in Rotating System of Coordinates</i>	<i>rad</i>
ρ	<i>Density of Tire Material</i>	<i>kg/m³</i>
φ	<i>Angular Position Defined in Non-Rotating System of Coordinates</i>	<i>rad</i>
ω	<i>Natural Frequency</i>	<i>rad/s</i>
$\bar{\omega}$	<i>Angular Velocity of Tire</i>	<i>rad/s</i>

CHAPTER 1 INTRODUCTION

Tire dynamics has been of interest to researchers in recent years in view of its impact on vehicle ride vibrations. The effects of tire design on the vibration transmitted to a vehicle body and on the noise produced and transmitted have been studied extensively by researchers. Tire is part of the vehicle suspension system and the vibrations transmitted to the vehicle, driver, and the passengers depend on tire vibrations also. In addition to the ride vibrations, the noise produced contributes to the road traffic noise prevalent in crowded communities. The road traffic noise is a crucial issue and the two major contributors to this noise are engine noise and tire-road noise. For riders and for others in the vicinity, the tire-road noise becomes a serious problem particularly at higher driving speeds. Two different mechanisms for the tire-road noise generation are the vibration of the tire body and the air flow around the tire body.

Tires are composite structures made of steel and rubber. As such it is necessary to apply theory of composite mechanics in order to analyze the displacements and accelerations of

the continuum. Since tires are always in contact with the road and the forces are applied through the contact surface, a third crucial issue is the contact mechanics and deformation.

1.1. MOTIVATION

Studies done in the past treated the vehicles as multi degree of freedom vibrating systems where tires form part of the vehicle suspension system. In these studies the tire rotation dynamics is not considered. However, when tires are studied separately, the tire rotation dynamics is considered. In earlier studies, tire contact mechanics has been studied by considering the tire as a ring or shell, but the relationship between vehicle dynamics and tire dynamics has not been combined. The contact surface between the tire and the road has been analyzed by using different methods. Finite element models as well as mathematical models have usually taken into account the deflection in both the tire and the road. In numerous studies, different models of tire including ring and shell models have been considered. These studies have also taken into account the effects of the tread band, of the rotation, of the Coriolis acceleration, and of the centrifugal acceleration.

The present study proposes a new model by replacing the position of the constraint in the tire. In the conventional ring or shell type model, the center of the tire is fixed. It is assumed that the tire body rotates around it. Then the contact forces are applied or the amount of stationary deformation due to the static loads is noted. In the present model, the location of the constraint is chosen to be at the tire-road contact region. The center is allowed to move vertically and horizontally. The vehicle body undergoing the bouncing motion is supported by the suspension system. Moreover, contact with the road restricts

the tire dynamics. Hence, the contact force is obviously dependent on the dynamic response of the tire as well as on the motion of the vehicle body.

1.2. LITERATURE REVIEW

The aim is to study the dynamics of the vehicle including the suspension and the dynamics of the rotating tires. The literature survey is carried out keeping the following three categories in mind:

- Vehicle as a component that is mounted on the suspension. This model does not include the rotating tires and the contact forces.
- Tire as a single component, both non-rotating and rotating where the dynamics of the vehicle is not taken into account.
- The combination of the vehicle body and the tire and the contact in which the effects of the kinetics of the vehicle body is combined with the effect of the vibration of the rotating tire.

Vehicle System

Several past studies have attempted to develop a realistic equivalent model for on-road vehicles. In the late 1980s and 1990s, the design of an active suspension system raised the importance of having an accurate model [1, 2].

In 1999, Kim et al. [3] used a model built in ADAMS to evaluate the parameters of an equivalent quarter-car model with two degrees of freedom. They compared the results of three different suspension models: one was simulated by ADAMS; the second was a

nominal quarter-car model with two degrees of freedom. The parameters of this nominal model were equal to the mass of the vehicle body, the mass of the tire, the stiffness of the tire, and the spring constant of the suspension system. The third type of model was identified as a model with two degrees of freedom and with parameters obtained after system identification. To achieve this identification, the results of the ADAMS model were analyzed in such a way as to obtain equivalent parameters. The system identification enabled Kim et al. to study different layouts of the suspension system. In other words, they changed the suspension system parameters such as the strut-inclination angle, the swing-arm length, and the lower-strut mounting-point. They compared the equivalent systems of both double-wishbone suspension and Macpherson suspension. They discovered deviations between the nominal model and the identified model both in double-wishbone suspension and in Macpherson suspension. The deviation of the double-wishbone suspension is more significant.

In a report published in 2002 [4], Lu Sun used a three-degree-of-freedom model of a vehicle to optimize the suspension parameters. This model is called a walking-beam model. A spring, a mass, and a damper in combination form the right wheel. The left wheel is composed of a similar combination. A third mass-spring-damper combination is used to represent the driver and the driver seat. Sun first calculated the Frequency Response Functions for both the driver and the tire. Then he used the Power Spectral Density (PSD) of a standard road profile [5, 6]. He did this in order to calculate and then to optimize driver comfort and tire loads. In the transformation of the road profile into a system excitation profile, the effect of the vehicle velocity was taken into account. The

results showed that the pavement loads are the primary concern of vehicle suspension design.

Hong et al. [7, 8] used a linear model of Macpherson suspension in which the rotation of the control arm as well as of the upper strut was allowed. The model had two degrees of freedom. The linear model was used as a part of a quarter-car model to design a skyhook controller. In this design, the vehicle speed and the road characteristics were used as parameters having a significant effect on the response. Hence, the variables of the skyhook controller were designed accordingly. Using a robust control scheme, M. S. Fallah et al. [9, 10, 11, 12, 13] studied the control of a model similar to that of Hong et al. [7]. The focus of their study was on the ride comfort and the stability of vehicles.

The vehicle chassis as a continuous system and its influence on the vehicle system vibration have been considered in several studies. The vehicle chassis can be considered as a beam with suspended masses representing the engine and the driver [14]. System identification was used to find the transfer function of a chassis by Seba et al. [15]. They designed an H_{∞} controller to reduce the low frequency noise of the engine. Olsson used a robust control approach to isolate the engine vibration from the vehicle body vibration [16, 17]. Moreover, a magnetorheological damper was used to reduce the vibration of a flexible structure caused by engine excitation or road excitation [18, 19].

The study of Dekker in 2009 [20] is one of the rare studies in which the influence of the flexibility of buggies on the dynamic response of non-rigid bodies is addressed. Although the subject of this study is the railway, the results and models can be used for the study on vehicles, too. The model of Dekker shows that, at certain velocities, the frequencies of

the non-rigid body vibration may be similar to the frequencies based on the road profile. Therefore, resonance is possible.

Studies report the effects of the deformation of soil on the dynamics of vehicles. In 1997, Fassbender [21] et al. reported the self-excitation of vehicle wheels on soft soil. This effect becomes severe if the residual soil-deformation caused by the front wheel excites the second wheel of the vehicle, too.

Park et al. [22] also studied the influence of soil deformation on heavy off-road vehicle dynamics. They used three different models of the vehicle:

(1) A conventional quarter-car model with a point contact on rigid ground

(2) A quarter-car model with a rigid wheel moving on deformable ground. This model consisted of the following:

a spring and a damper, which represented the suspension system,
a mass representing the vehicle body, and
a rigid cylindrical object as the tire.

(3) A quarter-car model with only a rigid tread band in contact with deformable ground. In this model, the soil was modeled as an elasto-plastic material. The tire could move vertically because it was modeled with a mass and a spring, but the tire surface was a circular rigid object. Park et al. discovered that the first model (a point-contact model) was good for the light vehicles on paved roads. However, the accuracy of this model was reduced by increasing the mass of vehicles and the elasticity of the ground. For heavy

vehicles working off-road, the ground should be considered elastic and the tire of the vehicle, rigid.

The vehicle vibration response is the result of the interaction of the vehicle with the road roughness. In addition to the studies carried out to develop accurate models for vehicles, numerous studies are available where the profile of the road is focused. Yong and Foda have studied the stress distribution in the contact patch between a tire and a deformable road [23]. Yong and Eiyu [24] have investigated the response of a pneumatic tire rolling on a rough, non-deformable road. They used an ultrasonic distance detector to measure the road profile. Then, they performed frequency domain analysis to represent the theoretical relationship between the road and the tire as a multi-degree-of-freedom (MDOF) system. Their results showed that the tractive efficiency was reduced by increasing both the traveling speed and the road roughness. Also, the higher inflation pressure provided better tractive efficiencies at the expense of reducing ride quality. The PSD of the road roughness in the study of Yong and Eiyu [24] appeared to be a straight line. However, in 1992, Xu et al. [25] presented a new method for measuring road surface roughness. In their method, a pulse was transmitted to the road and the echo was received by a non-contact acoustical transducer. The transmission time was used in the road profile measurement. The authors discovered that the PSD of the road roughness on a logarithmic scale deviated from a perfect line.

Tire Dynamics

In one of the earliest and most famous studies, Soedel [26] considered the tire as a non-rotating thin circular structure. The contact with the road was neglected, but it was

assumed that the contact force was rotating around the tire. The natural modes and frequencies of the non-contacting tire were then calculated. These results were used to approximate the response of the tire to a vertical contact load by defining the three-dimensional dynamic Green functions.

In subsequent studies by Soedel et al. [27, 28], a similar model was assumed, but in this case the lowest point of the tire was fixed on the ground such that it did not move vertically. In other words, another constraint had been added to the center-fixed structure thereby restricting the radial displacement at the contact point to zero. The same method as that used in Soedel [26] was used to find the natural frequencies of the tire. The results show a significant increase in the natural frequencies of the tire. Distorted mode shapes are reported and compared with the experimental results as well, thereby explaining the importance of the ground contact.

Hunckler et al. [29] introduced a finite element model in which the nonlinear geometry of the tire cross section was considered. The tire used in their analysis was modeled as a non-rotating shell. The center of the tire was fixed, and the road contact was neglected. Also the static deformation due to the inflation pressure of the tire was taken into account as a large nonlinear deformation, and the corresponding potential energy is taken into account mathematically. The axisymmetric modes and frequencies were presented. Later, the results of this study were used by Chang et al. [30] in order to find, first, the frequency response of a ring type shell under a point harmonic load excitation and, secondly, the steady state response of a ring type shell to travelling loads, which can either be a rotating point load or a rotating distributed load. Another study Chang et al. [31] used the same model to study the response of tires to the travelling load induced by

road roughness. That study investigated the effects of harmonic force and random force, both of which are functions of the velocity of the vehicle. Finally, Kung et al. [32] used the finite element approach to estimate the cross section profile of the tire. Kung et al. presented the natural frequencies and mode shapes of the tire, which they verified experimentally.

The effects of Coriolis and centrifugal accelerations are included by Huang and Soedel [33] in their discussion of the dynamic response of a rotating ring. Their study shows that it is reasonable to assume that the internal pressure of tires act as an elastic foundation. Also, for the first time, the researchers in the same study take into account the resultant force due to the centrifugal acceleration in the equations of motion. Moreover, two different cases of extensional and in-extensional ring theories are also compared, and it is indeed shown that the latter is not applicable to the model of a rotating ring. It is inapplicable since higher natural frequencies of the ring are missed when the in-extensional ring model is applied. Also the practical model of a rotating ring with a stationary point load is compared with the simplified model of a stationary ring with a travelling load, which has been the subject of previous studies. It is observed that in the case of a rotating ring with a stationary point load, there is no critical speed whereas the second model results in a critical speed due to rotation. Moreover, as the Coriolis acceleration increases, the results of the two models differ significantly, especially when the damping ratio is higher. The study also reported the bifurcation of natural frequencies and the on-going mode shapes for the rotating ring. In a later study [34], the harmonic response of the model with the rotating ring is compared with that of the stationary ring with travelling force. Huang and Su [35] modeled the tire belt as a rotating ring that is

supported by an elastic foundation with radial and tangential stiffnesses. This elastic foundation represents the sidewall. In-extensional ring theory is used to study the eigen-properties of the tire. They set up the model with the wheel axle fixed in space. Huang and Su simulated the road contact by constraining the displacements in both radial and tangential directions instead of representing the road contact by a simulated external load. The results show an increase in the natural frequencies of the rolling tire due to ground contact. However, they decrease at higher rotational speeds.

Stutts and Soedel [36] modeled the tire as a tension band on a viscoelastic foundation. They obtained the analytical solution for the model by not taking into account the bending stiffness and instead by analyzing the effects of the rotation as well as the contact region. In their work, they discovered the existence of a stationary contact region and that this region is a function of the rotating speed. The results show that the ground region shifts forward in the rolling direction.

Working on the same problems but using a finite element model instead, Padovan [37] found the natural frequencies of a rotating shell. In that study, he investigated the Coriolis acceleration, pre-stress loads, and material anisotropy by using the same model and verified the results by the analytical model presented in [38]. It was observed that bifurcation in the natural frequencies was caused by the angular velocity of the shell.

Padovan [39] carried out the finite element analysis of a rotating ring that was supported on an elastic foundation (modeled as a spring) and subjected to a stationary contact load. The radial force was applied at the contact point in order to model the weight of the vehicle. The radial displacement was analyzed at different rotating speeds. Later, this

study was expanded to include the transient response due to a rotating force on a center fixed ring [40].

Padovan et al. [41, 42, 43] investigated the steady state response and the transient response of a nonlinear viscoelastic structure by introducing a new finite element model. This model was used to study how rolling and contact affect a center-fixed 2-D ring or a center-fixed 3-D shell that are subject to a traveling load. The response of the system to bumps and impacts was also modeled.

Brockman et al. [44] introduced a new semi-analytical method which combines the finite element method on the cross section of the tire with the sinusoidal basis functions in the circumferential direction. Reducing the amount of calculation by turning a three-dimensional problem to a two dimensional problem, this method allows one to consider the static deformation of the inflation pressure.

Zegelaar and Pacejka [45] used a center-fixed inextensible ring model to study the in-plane response of a tire to a rectangular bump. In their model, the vehicle moves at a velocity of 3 km/h. The tire in their model rotates at such a very low rotational speed that the effect of rotation can be neglected. The results from their model are compared with those from their experiments on a center-fixed tire rotating over a big wheel. At higher velocities, the center-fixed inextensible tire is replaced by a four-degree-of-freedom model.

The study by Iwao and Yamazaki [46] describes the mechanism of tire and road noise generation. As stated in the report, about one third of vehicle noise is caused by tire-road contact. The most important parameters in this noise generation are the surface roughness

of the road, the pattern of the tread in contact with the road, and the torque that exists during acceleration. The results, measured by a laser displacement meter, show that the noise generated by different portions of a tire has different characteristics. The noise in the range of 400 to 600 Hz is mainly radiated from the side-wall, whereas the higher frequency noise, between 800 to 1600 Hz, corresponds to the tread vibration. Moreover, the wheel housing helps the lower frequency waves resonate more than it does the higher frequency waves. In other words, the contribution of the housing is less for higher frequency waves.

Kim et al. [47] reported the use of a microphone in order to measure the structure-borne noise inside a vehicle. The test set-up consisted of a stationary vehicle excited by a dynamic shaker, with a random signal input. The focus of the study was on the waves below 1 KHz. Excited by the tread-road interaction, the side-wall vibration generated the waves below 1 KHz. The study identified the tread pattern of the tire, the non-uniformity of the tire, the tire-road contact, and the road roughness as the major sources of the tire side-wall vibration and consequently of the generated noise. The study presented the influences of the tread vibration, the side-wall vibration, and the rim vibration on the vehicle interior noise.

Pinnington and Briscoe [48] described tire dynamics by using a one-dimensional wave equation. In their study, the tire belt was modeled as a Timoshenko beam. As functions of the bending stiffness of the beam, the axial tension in the tread, and the rotary inertia of the tire cross section, the different modes of vibration were categorized into those related to tension waves, bending waves, rotational waves, and longitudinal waves. Pinnington and Briscoe realized that the majority of the waves with frequencies below 100 Hz are

mostly tension waves, whereas above 200 Hz, the majority of the waves are shear waves. In the mid-frequencies, the majority of the waves are bending waves.

Dihua et al. [49, 50] presented a geometric model of the tire-road contact. That model took into account the radial force and the tangential force in the contact area. These forces were derived from the radial and tangential displacements. The effects of rotation were not taken into account in that study. The authors described the enveloping phenomenon, in other words, the ability of the tire to follow the road-obstacle profile while it rolls with adequate rotational speed over the obstacle. To achieve that, they simulated the vertical force and the longitudinal force at the axle of the tire. Dihua et al. used the experimental modal parameters presented by Yam et al. [51] to carry out the simulation. The results were similar to those presented by Zegelaar and Pacejka [45]. Dihua and Chengjian [52] investigated the effects of the cutoff frequency range and of the side-wall nonlinear stiffness in a subsequent study.

In 2003, Muggleton et al. [53] reported a study in which a plate was used as the tread and another plate as the sidewall. They assumed that both plates vibrate out of plane, and solved the problem by using wave propagation analysis. The compatibility equations between the two plates were employed to join these two plates. However, the effects of the contact were ignored in the solution. The analytical results were compared with those from an experiment, where the tire was fixed at the center and then excited. The study concluded that at lower frequencies, the response was controlled by sidewall properties, and at higher frequencies, the response was more dependent on tread properties.

Bashmal et al. [54, 55, 56, 57, 58] investigated the in-plane vibration of circular annular disks and the generated sound. They modeled a railway wheel as a disk that has combination of different boundary conditions at the inner and outer edges. They used the Rayleigh-Ritz method to obtain the frequency parameters for the required number of modes for a wide range of radius ratios and Poisson's ratios of annular disks under clamped, free, or flexible boundary conditions. Although the focus of that study is on railway wheels, the results can be used to investigate the vibrations of the tire-rim assembly.

Bolton et al. [59, 60] investigated the effect of rotation on wave propagation and on the natural frequencies of an inflated circular shell, which they used as a model of the tire. In their study, they assumed that the center of the shell is fixed and the body rotates around it. The equations of motion were written by defining non-rotating system of coordinates, namely, Eulerian coordinates. Employing a wave-like solution for the free vibration analysis of the assumed model, they solved for the natural frequencies, which showed that the effect of rotation was not significant. Then, in the next step, the response of the system to a harmonic force at the contact point was obtained by employing the basis functions. It was shown that the natural frequencies of a rotating shell with fixed coordinates were divided into those corresponding to positive-going waves and negative-going waves. This behavior is in contrast with the behavior of a stationary shell. The Coriolis acceleration creates a difference between the natural frequencies of the positive-going and negative-going waves and the natural frequencies of the waves of the non-rotating shell. In another study, where the tire was considered as a shell, Jia et al. [61] approximated the geometry of a pneumatic tire cross section by using Bezier functions.

They applied the theory of composite materials to calculate the kinetic and potential energies of the shell. The finite element method was employed in that study to investigate the effects of the tread patterns, the inflation pressure, and the ply-angles of the steel belts. Since the shell in their study is fixed in the center, there is no translational motion to be studied. The rotation and the contact are not investigated.

In 2007, Civalek [62] presented a three-dimensional analytical solution for a rotating laminated cylindrical shell. This composite shell rotated around the symmetric axis, which was considered fixed in space. Transformed reduced stiffness matrices of different layers were used to build up the stiffness terms of the equations of motion. The centrifugal and Coriolis accelerations were also included in the equations of motion. Trigonometric functions were employed to find the solution to these equations. The effects of different types of laminations were discussed. Civalek and Gürses presented a new technique for that problem in 2009. [63]

Rustighi and Elliott [64] used the same tire model proposed by Huang and Soedel [33] to investigate the response of a tire to stochastic excitation from the road. The Rustighi and Elliott study took into account the stiffness of the sidewalls and the inflation pressure. However, this model did not take into account the effects of the rotation such as the centrifugal and Coriolis accelerations. Hence, the Doppler shift caused by the Coriolis term did not occur. The stiffness of the suspension system was also neglected. A simplified contact model was used in the study mentioned above. The study considered that the contact patch was stationary, and the tire was always in touch with the road. After applying a standard road profile, Rustighi and Elliott used a discretization method to study the Root Mean Square (RMS) of the kinetic energy, RMS of the radial

displacement of the tire, and RMS of both vertical and horizontal forces, which are at the center of the ring. The investigation is further extended to three-dimensions by using finite element model [65].

Kim et al. [66] used three different models to investigate the frequencies of a tire. At frequencies below 80 Hz, they used a spring-mass system, the side-wall acting as a spring and the tread acting as a mass. In the frequency range of 80-300 Hz, since the significant modes were the bending waves in the tread, Model 2, a beam supported on an elastic foundation was used. At the frequencies above 300 Hz, the modes turned from one-dimensional waves to two-dimensional waves. Consequently Kim et al. used a shell model with a cylindrical shape.

In 2008, Delamotte et al. [67] carried out analytical and experimental research on a center-fixed ring. As their report states, a closed-form analysis was performed in order to explain the irregular wear on the tire as well as its critical rotating speed, and the noise radiation. The model included a center-fixed ring, which was allowed to undergo two-dimensional in-plane displacements. There was a force that rotated around the ring. The equations of motion were solved without taking into account the Coriolis and centrifugal accelerations. Delamotte et al. studied the influence of the internal pressure on the free and forced vibrations of their model. The analytical solution presented in this paper was new. However, it did not reveal any new information about the dynamic response of the tire. A model, similar to that of Delamotte et al. [67], was used by Kindt et al. in 2009 [68]. Kindt et al. combined the ring model of a tire with the dynamics of the wheel to study the modes and frequencies below 300 Hz.

Another study carried out by Wullens and Kropp [69], concentrated on a three-dimensional model of a contact area between a rotating tire with a rigid surface. The formulation of the problem in the time domain was carried out after taking into account the local deformation caused by the road roughness as well as by the radial contact forces. This contact model was used by Wullens and Kropp to find a wave-based solution to the problem of the natural frequencies of the tire [70]. The Green functions of a center-fixed rolling tire are used to find the dynamic response of the tire to the contact forces.

Since the contact surface and the contact forces have a significant effect on the ride quality, the generated noise, and the vibration of the tire body, many experimental studies have been carried out on the tire-ground contact issue. In a study that appeared in 2002, Perisse [71] investigated the mechanism of tire-road noise by setting up a center-fixed tire rolling above a large wheel drum in a laboratory. Because the diameter of the drum was large enough, the contact patch was considered to be flat. A smooth tire was used to eliminate the vibration caused by the tread pattern. Experimental measurements were performed to find the acceleration on both tread band and sidewall at different angular velocities. Spectral analysis showed that most of the energy in the system was concentrated in the waves below 500 Hz. Moreover, the response on the tread was larger than the response on the sidewall, especially at higher frequencies. The radial displacement was also obtained by integrating the acceleration to provide two different types of responses: the stationary deformation caused by the vehicle weight; the bending vibration caused by the tire-ground interaction forces.

Since it is difficult to model the contact deformation, and to model the complicated geometrical and structural properties of the tire, many researchers have used the finite

element method to analyze tire dynamics. The study of these contact forces has been combined with the study of the dynamics of the rotating tire. Brinkmeier et al. investigated the eigen-solutions of the three-dimensional finite element model of a tire and the noise produced as a result of road roughness [72]. In the Brinkmeier study [73], the contact surface is approximated by the *Arbitrary Lagrangian Eulerian* (ALE) formulation proposed by Nackenhorst. The ALE is based on the mathematical concept of kinematics, on the curvature of both surfaces, on the balance of mass, and on the balance of momentum. Brinkmeier et al. decomposed the problem into three parts: a stationary rolling case, the vibration in the deformed state, and the noise radiation. They found that splitting in the natural frequencies happens only when a rotating ring is perfect and without contact. For a rotating tire in contact with the ground, the positive going and negative going waves do not occur. Moreover, the modes are complex.

The finite element model of a stationary tire was first developed by Lopez et al. [74] using a standard FE package. In that study, the effects of rotation were added, and then the matrices were transformed into Eulerian coordinates in order to perform the Eulerian finite element analysis of a rotating tire. Lopez et al. investigated the wave propagation and the natural frequencies of a circular rotating ring and a circular rotating shell. The equations of motion were written so as to take into account the Coriolis effect and the stiffening effect of the rotation when the inertial terms are transformed into the non-rotating coordinates. It is assumed that the center of the tire is fixed and the body rotates around it. In this model, there is bifurcation of the natural frequencies, caused by immobilization of the center of the tire. In another study, Lopez et al. [75] presented the effects of contact deformation in a three-dimensional model developed in the study

previously referred to. The contact is frictionless and hence, the road surface and the tire are both smooth. In order to simulate the deformation caused by the static loads, the center of the tire is fixed, a vertical displacement is applied to the bottom of the tire, and the displacements and the forces are measured. The natural frequencies show that “the neat eigen-value distribution for an undeformed rotating tyre predicted by the Doppler shift is not directly applicable to a deformed rotating tyre.” [75]

Geng et al. [76, 77] performed an experimental modal analysis of a tire and compared the results with those from an analytical model to find the damping value of a tire. Displacements of 16 points of a tire were measured. These displacements were used by Geng et al. to determine the mode shapes and the Frequency Response Functions. Then, the natural frequency and the damping ratio of each mode were analyzed corresponding to the model of a center-fixed tire. Finally, the damping matrix was developed. The overall results revealed an efficient method that helped the researchers to overcome the restrictions of proportional damping assumptions. However, the effects of contact between the tire and ground and the effects of the inertia of the vehicle body were not discussed in that study.

The study by Kindt et al. [78, 79, 80, 81] is based on the measurement of the forces at the hub of the wheel and the displacements at the tread of the tire. This set up consists of two tires. One of the tires is driven by an electromotor and it is referred to as the driver tire. The other tire, which is fixed at the center by using a multi-axial wheel hub dynamometer, is called the driven tire and is the subject of the test. The dynamometer measures the forces at the tire center in three dimensions. The distance between the centers of these two tires is adjustable so that one can simulate the contact deformation

and the static loads on the driven tire. A Laser Doppler vibrometer was used to measure the displacements of fifty eight points on the tread of the driven tire. The natural frequencies of the tire were calculated by analyzing the forces in the frequency domain. In the first place, it was verified experimentally that the splitting of the natural frequencies does not occur for a tire in contact. Secondly, the mode shapes are complex. Thirdly, the road impact excites the tire in frequencies below 300 Hz.

To study the free vibration of tires, Sabiniarz and Kropp [82] used a waveguide finite element method. In this study, the center of the tire was fixed; the tire was stationary; and the tire was not in contact with the ground. The authors focused on frequencies in the range of 0-1500 Hz. The results showed both curve veering and bifurcation. The influence of different types of modes on sound radiation was discussed.

Zimmer and Otter developed a tire-ground model progressively [83]. The model at first started as an ideal rigid rolling wheel. At the second step, the slipping of the wheel on the ground was added to the model and the corresponding equations were developed. Zimmer and Otter [83] inserted a spring and a damper at the third step in order to model the contact deformation and contact force. Rolling resistance was also taken into account in this development. At the fourth step, smooth tire was replaced by a tire with treads. This replacement allowed the researchers to study the deflection and the elasticity of the treads in the contact area, as well as the nonlinear effect of the normal load. Lateral slip and self-aligning torque were taken into account at this level, too. At the next step, the effects of tire deformation in both lateral and longitudinal directions were studied by adding a spring and a damper in each direction. The last step was to model the actual shift of the contact point caused by rotation. Equations of the models at each level were

derived for a bicycle and were solved by using commercial software. The results of different models showed that the friction, the slippage, and the tire deformation have a damping effect that makes the vehicle much more stable. The study of Zimmer and Otter showed the importance of complex models for the simulations of maneuvers. However, this study did not take into account the effects of the tire structure and vehicle-body inertia.

Imperfect Ring

In addition to the structure of tire, the effect of unbalance also has received attention by the researchers. In 1986, Allaei et al. [84] used the Galerkin method to study the influence of ring imperfections on the natural frequencies and the modes of the tire. The tire was modeled by a non-rotating center-fixed ring. Their study covered three types of imperfections: a non-uniform mass at the circumference of the ring, a non-uniform linear spring in the radial direction, and a non-uniform torsional spring at the circumference of the ring. Later, the study was extended to treat the case of multiple springs [85]. In a subsequent study, Allaei et al. [86] performed the analysis with a three-dimensional model of a tire obtained by the finite element method. The analysis revealed that a non-uniformity caused by a point mass changes the higher frequencies of the tire more than it does the lower frequencies. In contrast with the non-uniform mass case, the shift caused by a non-uniform stiffness is more significant at lower frequencies.

In 1995, Stutts et al. [87] reported the use of a rigid ring as the model of the tread-band of a tire. The tread-band was supported on a visco-elastic foundation. In addition to the visco-elastic foundation, there was a linear spring representing the non-uniform stiffness.

They discovered that the non-uniformity created a harmonic force, the frequency of which was twice the frequency of the rotations.

Fox [88] proposed a method to modify the frequency of a ring according to three types of imperfections. He assumed that the imperfections were small, and he could therefore use the Rayleigh-Ritz method. As mentioned in his report, the effect of the imperfections is significant. Fox's study was extended by Rourke et al. [89, 90] in order to correct the imperfections of the rings. Also, Eley et al. [91] followed the method presented in Fox's study [88] to analyze the effect of the Coriolis accelerations on the frequencies of a ring with imperfections, rotating in three perpendicular axes. Moreover, in 2005, the methodology presented in Fox's report [88] was used by McWilliam et al., [92] to study the effects of the random distribution of imperfect mass. McWilliam et al. investigated three types of random distributions:

- 1) Random harmonic variations in the mass per unit length around the circumference of the ring
- 2) The attachment of random point masses at random locations on the ring
- 3) The attachment of random point masses at uniformly spaced positions on the ring

In 2007, Bisegna and Giovanni [93] presented a closed-form solution to the problem of an imperfect ring by using the perturbation method. The ring that they considered had two types of non-uniformity. The mass density and the in-plane bending stiffness could vary along the circumference of the ring. They proposed solutions by using two different theories: the linear theory, which was efficient for small non-uniformities; the enhanced

theory, which required an iterative solving procedure, but was accurate for large non-uniformities.

In 2008, Dillinger et al. [94] presented a discrete model of a tire with non-uniformities. Non-uniformities consisted of mass imbalance, stiffness non-uniformity, and radial run-out. They assumed that the center of the wheel was fixed. Their discrete model was used to predict the forces at the wheel hub. The predicted forces were compared with the experimental results in order to perform system identification. Their simulation demonstrated that the non-uniformities caused significant forces, at frequencies close to the natural frequencies of the system, thereby resulting in a large amplitude vibration of the different components.

Combined Models

Most of the research, dedicated to the vibration and frequencies of tire, consider the tire as an individual elastic object. The contribution of the vibration of tires in the multibody dynamics is not concentrated very often.

In the study by Kung et al. [95] the tire-wheel unit is modeled as a combination of a rigid center mass, which is free to move vertically, and of an elastic ring supported by distributed springs in radial and tangential directions. The distributed springs are attached to the rigid center mass. The effect of the contact with the road surface is not taken into account. The results obtained by the analytical solution are verified by comparing them with those obtained by the finite element approach of [29–32]. Kung et al. concluded that the free movement of the wheel center affects only the first mode and only the first natural frequency of the ring. In a further study by Kung et al. [96, 97], this model was

expanded into a tire-wheel-suspension assembly, which was used by the same authors to find the response of the assembly to harmonic excitation caused by the road.

In another study, Huang and Hsu [98] studied the effect of a suspension system on tires. They considered the damping and the stiffness of the wheel, as well as the inertia of its vertical motion. The results obtained in their study did not take into account the mass of the vehicle. The kinetic energy caused by the vertical motion of the wheel center was also not taken into account.

An instantaneously centered Lagrangian observer was defined in order to make it possible to follow the displacement of the tire [99, 100]. The finite element approach was used to study the steady and transient responses of structures consisting of rotating components. The idea of a Lagrangian observer is further employed by Padovan et al. in their 1992 study [101].

A tire wheel suspension assembly was introduced by Dohrmann [102] to study the effects of the tire-ground contact as well as the suspension system on the natural frequencies of the rotating tire. Linear spring elements and dashpot elements were used to model the suspension system. The suspension was assumed to be connected to a rigid body located at the center of a ring. This rigid body represents the mass of the wheel, and its rotational speed is constant. An inextensible circular ring on a foundation was used to model the tire body. The wheel-and-tire assembly was released to move vertically, and the kinetic energy added by this degree of freedom was taken into account. The equations of motion were solved in the fixed-frame coordinates instead of in the rotating frame. The contact

surface deformation and the contact force distribution over this surface were calculated and were linearized so that they could be used in the equations of motion.

An experimental set-up similar to that used in [71] was used to analyze the effect of a bump impact on passenger ride comfort [103]. The accelerometer was mounted on the axis of the vehicle in order to measure the acceleration of the center of the tire. The experimental results were compared to those of a seven-degree-of-freedom model. A parametric study of the tire was carried out to analyze the effects of the tread rubber on the vibration energy. Their study also took into account the effects of the tire tread belt on the vibration energy. The effects of the sidewall characteristics were also analyzed.

Mohd Nor et al. [104] introduced the Vehicle Acoustical Comfort Index (VACI) and the Vehicle Acoustical Comfort Factor (VACF) as two parameters used to measure the noise in a vehicle compartment. They presented results that were obtained by performing tests on different types of roads. The noise inside the vehicle was recorded. The data was then compared with those obtained under other road conditions. It is shown that as the degree of loudness increases, the Vehicle Acoustical Comfort Factor decreases. Moreover, the roughness of the road does not affect the Vehicle Acoustical Comfort Factor. Another report [105] revealed the results of a similar test, which considered the effect of road roughness and the driving speed on the vibration of the driver's seat. In a subsequent study [106], the influence of the vibrations of the engine and the tire on the seat vibration was studied while the vehicle was being driven on different roads. The sources of excitation were separated. In other words, the effects of the road roughness were ignored, and only the tire vibration and engine vibration were taken into account. The results showed that only the frequencies below 400 Hz had significant impact on the vibration

recorded for the seat. Also the excitation caused by the engine was comparable to that caused by the tires for a smooth road. However, tire vibration rises on bumpy roads so that it turns out to be the dominant source of excitation. The Frequency Response Functions of the engine mount and the tire damper show that these parts efficiently dampen the vibration below 1400 Hz and 200 Hz, respectively.

Nguyen and Inaba [107] have reported the use of accelerometers and strain gages in order to measure roll, bounce, and pitch accelerations, as well as the forces on the rear wheels. The vehicle used in the test procedure was an agricultural tractor driven on an asphalt road and a sandy loam field. The wavelet and the Fourier analyses were used in order to study the effects of the variation of tire characteristics such as non-uniformity and inflation pressure for different tractor forward speeds.

1.3. OBJECTIVES AND SCOPES

As mentioned earlier, most of the studies carried out on vehicle dynamics considered the vehicle, the suspension, and the non-rotating tires as a multi degree of freedom system, while the tire alone was considered as an isolated stationary or rotating ring or shell. The objectives of this thesis are as follows:

- 1) To develop a new model that takes into account the inertia of the vehicle body and the dynamics of the rotating tire. Although this model is two-dimensional, it can easily be extended to three-dimensional problems.
- 2) To investigate the effect of the vibration of the rotating tire on the contact force. The contact force is a dynamic force, which is function of the bounce vibration of the

vehicle as well as the tire rotational dynamics including the radial and tangential displacements and accelerations of the tire.

- 3) To explore various solutions for the model. Different methods are employed, as each one has pros and cons. The finite element method will be used to study problems with complicated cross sections, while the analytical method provides the exact natural frequencies and modes.
- 4) To study the response of the system to the random excitation applied by the profile of the road. The free vibration response is used in mode summation method to investigate the contact forces in both vertical and horizontal directions as a function of forward speed of the vehicle. Also the displacements of the passenger and of the rotating tire are studied.

In the present study, some of the previous studies on the dynamics of a rotating tire are reviewed. Then, the conventional ring model for the tire is briefly analyzed in Chapter 2 in order to better comprehend the nature of the parameters affecting the dynamics of a rotating tire. These parameters include the Coriolis acceleration and the centrifugal acceleration, the bifurcation of natural frequencies, and the stiffening of the tire because of rotation. Then the new model is described in Chapter 3. The equations of motion are derived by applying the Hamilton principle. The Galerkin method is used to solve the equations in Chapter 4. Also the results for both cases of the non-rotating ring and the rotating ring are obtained and compared. Comparison of the results of the new model with those available in the literature is carried out wherever possible. Finite element analysis is employed in the second part of this chapter. Eulerian finite element is used to

find the free vibration response of the hybrid quarter car model. In Chapter 5, the basics of the model are reviewed and the analytical solution is introduced. This analytical solution, provided for a two-dimensional model of the hybrid quarter car model, enables us to find the frequency response more conveniently. The frequency response is used in Chapter 6 to investigate the response of the model to road excitation. The spectral densities and the mean value of the displacement and the contact forces are presented and compared.

Chapter 7 summarizes the conclusions arising out of the results of the investigations. Moreover, it provides suggestions for further investigations that could provide more clarity and context to the present study.

CHAPTER 2 CENTER-FIXED RING

2.1. INTRODUCTION

In this chapter, the equations of motion for the traditional model of a tire are derived and solved. The tire is modeled as a ring with a uniform rectangular cross section. It is assumed that the center of the ring is fixed and that the ring rotates around it. In the following, the equations of motion of such a ring are presented in both the rotating and the non-rotating systems of coordinates. The analytical solutions of the equations are presented and compared. Moreover, the bifurcation of the natural frequencies of the rotating ring in both rotating and non-rotating coordinate systems is studied. Such a study would help in better understanding the concept of the bifurcation of the natural frequencies of tires as well as the effect of the Coriolis and centrifugal accelerations. The model and the results are also helpful in developing the equations solved by the Galerkin method and the finite element analysis, both of which are presented in Chapter 4.

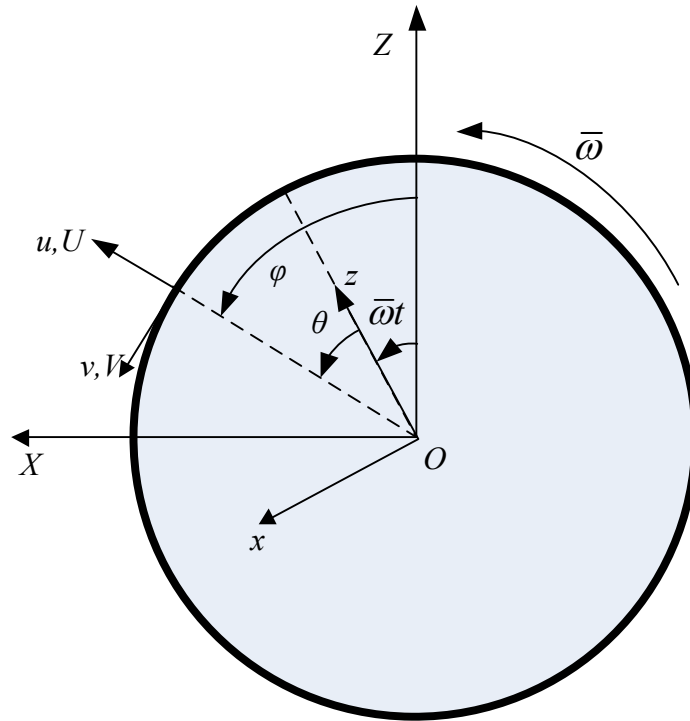


Figure 2.1: Schematic of the 2-D model of a tire: ring rotating about a fixed center

2.2. FREE VIBRATION OF A CENTER-FIXED RING IN ROTATING COORDINATE SYSTEM

Figure 2.1 shows the ring model of a tire. The ring presents the thread of the tire. It is assumed that point O , the center of the ring, is fixed and the ring is rotating around this point. Two different coordinate systems are defined. One is the local system of coordinates xz , rotating with an angular velocity $\bar{\omega}$. The angular position in this coordinate system is defined by θ . The other system of coordinates, used as a reference, is called the non-rotating coordinate system XZ . The angular position in this coordinate system is shown by φ . The radial displacement u , and the tangential displacement v , are defined in the rotating coordinate system. The effects of the inflation pressure of the tire

and of the rotational stiffening are taken into account by defining the resultant force N_0 . This circumferential resultant force, caused by the angular velocity and the internal pressure of the tire, is defined as follows [108]:

$$N_0 = abp + \rho A a^2 \bar{\omega}^2 \quad (2.1)$$

The static deformation of the tire as a result of this initial tension in the ring is a constant radial displacement, calculated as follows:

$$u_0 = \frac{pb + \rho A a \bar{\omega}^2}{\frac{EA}{a^2} - \rho A \bar{\omega}^2} \quad (2.2)$$

The general solution for the rotating ring is given by the superposition of the static deformation and of the dynamic response. The following equations, describing the dynamic behavior of the ring, do not include the constant static response. The following equations describe the equations of the motion of a ring in the rotating coordinate system xz , which is also called the local coordinate system [108]:

$$\frac{EI}{a^4} \left(\frac{\partial^4 u}{\partial \theta^4} - \frac{\partial^3 v}{\partial \theta^3} \right) + \frac{EA}{a^2} \left(\frac{\partial v}{\partial \theta} + u \right) - \frac{N_0}{a^2} \frac{\partial^2 u}{\partial \theta^2} + \rho A (\ddot{u} - 2\bar{\omega} \dot{v} - \bar{\omega}^2 u) = 0 \quad (2.3)$$

$$\frac{EI}{a^4} \left(\frac{\partial^3 u}{\partial \theta^3} - \frac{\partial^2 v}{\partial \theta^2} \right) - \frac{EA}{a^2} \left(\frac{\partial^2 v}{\partial \theta^2} + \frac{\partial u}{\partial \theta} \right) + \rho A (\dot{v} + 2\bar{\omega} \dot{u} - \bar{\omega}^2 v) = 0 \quad (2.4)$$

It should be mentioned that the nonlinear effects of the circumferential resultant force are neglected. The free vibration response of the model is expressed in the variable separation form as follows:

$$u(\theta, t) = \tilde{u}(\theta)e^{j\omega t} \quad (2.5)$$

$$v(\theta, t) = \tilde{v}(\theta)e^{j\omega t} \quad (2.6)$$

Substituting Equations (2.5) and (2.6) in Equations (2.3) and (2.4) results in the following equations, where \tilde{u} and \tilde{v} are functions of θ , only.

$$\frac{EI}{a^4} \left(\frac{d^4 \tilde{u}}{d\theta^4} - \frac{d^3 \tilde{v}}{d\theta^3} \right) + \frac{EA}{a^2} \left(\frac{d\tilde{v}}{d\theta} + \tilde{u} \right) - \frac{N_0}{a^2} \frac{d^2 \tilde{u}}{d\theta^2} - \rho A \left(\omega^2 \tilde{u} + 2j\bar{\omega}\omega\tilde{v} + \bar{\omega}^2 \tilde{u} \right) = 0 \quad (2.7)$$

$$\frac{EI}{a^4} \left(\frac{d^3 \tilde{u}}{d\theta^3} - \frac{d^2 \tilde{v}}{d\theta^2} \right) - \frac{EA}{a^2} \left(\frac{d^2 \tilde{v}}{d\theta^2} + \frac{d\tilde{u}}{d\theta} \right) - \rho A \left(\omega^2 \tilde{v} - 2j\bar{\omega}\omega\tilde{u} + \bar{\omega}^2 \tilde{v} \right) = 0 \quad (2.8)$$

In order to satisfy the continuity conditions of the ring, the eigen-functions of the equations above must be assumed in the following form:

$$\begin{aligned} \tilde{u}(\theta) &= \hat{A}e^{jn\theta} \\ \tilde{v}(\theta) &= \hat{B}e^{jn\theta} \end{aligned} \quad (2.9)$$

where n is an integer. By substituting Equation (2.9) in Equations (2.7) and (2.8), one can arrive at the following algebraic system of equations:

$$\begin{bmatrix} \frac{EI}{a^4} n^4 + \frac{N_0}{a^2} n^2 + \frac{EA}{a^2} - \rho A (\omega^2 + \bar{\omega}^2) & j \left(\frac{EI}{a^4} n^3 + \frac{EA}{a^2} n - 2\rho A \bar{\omega}\omega \right) \\ -j \left(\frac{EI}{a^4} n^3 + \frac{EA}{a^2} n - 2\rho A \bar{\omega}\omega \right) & \frac{EI}{a^4} n^2 + \frac{EA}{a^2} n^2 - \rho A (\omega^2 + \bar{\omega}^2) \end{bmatrix} \begin{bmatrix} \hat{A} \\ \hat{B} \end{bmatrix} = \begin{bmatrix} 0 \\ 0 \end{bmatrix} \quad (2.10)$$

The eigen-values of this system of equations are the natural frequencies of a rotating ring in the rotating coordinate system. Table 2.1 presents the natural frequencies of non-rotating ring (i.e. $\bar{\omega}=0$) with the following values:

$$p = 206910 \text{ Pa}; \quad \rho = 1200 \text{ kg / m}^3; \quad E = 4.9 \times 10^8 \text{ Pa}; \quad b = 0.16 \text{ m}; \quad h = 0.008 \text{ m}; \quad a = 0.32 \text{ m};$$

Table 2.1: The natural frequencies of a non-rotating center-fixed ring

<i>n</i>	ω (rad/s)	
0	1996.91	
1	2830.11	183.12
2	4471.61	465.21
3	6320.17	746.06
4	8238.13	1028.15
5	10186.48	1316.34
6	12150.66	1614.05
7	14124.07	1923.91
8	16103.32	2248.07
9	18086.49	2588.36
10	20072.43	2946.38

Table 2.2: The natural frequencies of a center-fixed ring rotating with angular velocity $\bar{\omega}=100$ rad/s in the rotating coordinate system

<i>n</i>	ω (rad/s)			
0		2004.38		
1	2731.00	2930.99	96.19	296.18
2	4393.02	4554.41	413.84	575.24
3	6261.59	6383.28	733.27	854.96
4	8192.29	8288.02	1047.16	1142.89
5	10149.05	10227.46	1362.09	1440.51
6	12119.08	12185.33	1683.09	1749.34
7	14096.78	14154.08	2013.71	2071.01
8	16079.30	16129.77	2356.63	2407.10
9	18065.04	18110.14	2714.02	2759.12
10	20053.05	20093.82	3087.69	3128.46

As can be seen, substituting each n in Equation (2.10) results in two different natural frequencies except for $n=0$. Table 2.2 shows the natural frequencies of the same ring when the angular velocity is $\bar{\omega}=100 \text{ rad/s}$. Each natural frequency for $n \geq 1$ in Table 2.1 has been split into two groups in Table 2.2. For example, $\omega=183.12 \text{ rad/s}$ and $\omega=2830.11 \text{ rad/s}$ obtained as the natural frequencies of the first wave (i.e. $n=1$) along the non-rotating ring have been split into two different frequencies, (96.19, 296.18) and (2731.00, 2930.99), respectively. For each pair, the higher value corresponds to the negative-going wave, whereas the lower value corresponds to the positive-going wave. The following calculations show the corresponding natural frequencies and eigen-vectors of $n = \pm 1$.

$$n = 1$$

$$\omega = \begin{cases} 2731.0016 \\ 296.1794 \\ -96.1889 \\ -2930.9921 \end{cases}$$

for $\omega = -96.1889$

$$\hat{A} = 1 \text{ and } \hat{B} = 1.01j$$

$$u(\theta, t) = e^{j(\theta - 96.1889t)}$$

positive going wave

for $\omega = 296.1794$

$$\hat{A} = 1 \text{ and } \hat{B} = 1.01j$$

$$u(\theta, t) = e^{j(\theta + 296.1794t)}$$

negative going wave

$$n = -1$$

$$\omega = \begin{cases} 2930.9921 \\ 96.1889 \\ -296.1794 \\ -2731.0016 \end{cases}$$

for $\omega = 96.1889$

$$\hat{A} = 1 \text{ and } \hat{B} = -1.01j$$

$$u(\theta, t) = e^{-j(\theta - 96.1889t)}$$

positive going wave

for $\omega = -296.1794$

$$\hat{A} = 1 \text{ and } \hat{B} = -1.01j$$

$$u(\theta, t) = e^{-j(\theta + 296.1794t)}$$

negative going wave

As the sample calculation above shows, the natural frequency of 96.1889 rad/s corresponds to a positive-going wave, which can be demonstrated to be a sinusoidal wave

moving in the direction of tire rotation. The frequency of 296.1794 rad/s corresponds to a negative-going wave. This wave can be illustrated as a sinusoidal wave rotating in a direction that is opposite to the direction of the rotation of the tire. It should be noted that these frequencies have been defined in the rotating coordinate system, which rotates with an angular velocity of $\bar{\omega}=100 \text{ rad/s}$. Among the two lower frequencies obtained for each n , the smaller frequency is a positive-going wave and the larger frequency is the negative-going wave. Also among the two higher frequencies, the larger corresponds to the positive-going wave.

Figure 2.2 and Figure 2.3 show the bifurcating natural frequencies of the center-fixed tire in the rotating system of coordinates. It can be seen from Figure 2.2 that there is no bifurcation for $n=0$. The natural frequencies corresponding to $n=0$ are quite high compared to those for $n = 1$, because $n=0$ corresponds to a “breathing” type mode involving circumferential stretching and compression. This mode has a higher stiffness compared to the “bending” type deformation for $n > 0$. Also it can be seen that the bifurcating behavior decreases as the natural frequency of the ring increases. In other words, the difference between the positive-going and the negative-going waves is greater at the lower frequencies, whereas at the higher frequencies this difference is smaller.

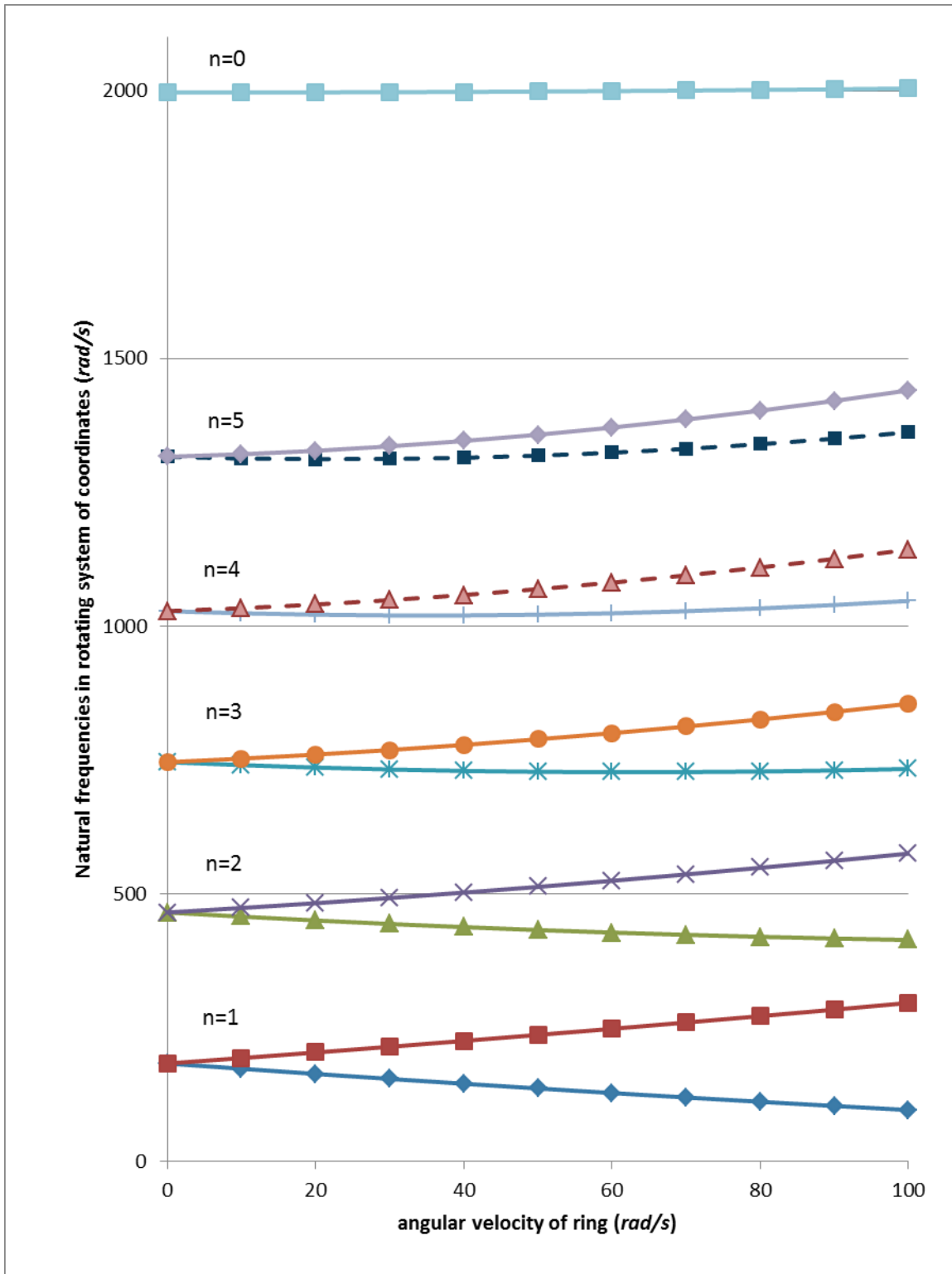


Figure 2.2: The bifurcating natural frequencies (less than 2000 *rad/s*) of the center-fixed ring in the rotating system of coordinates vs. different angular velocities.

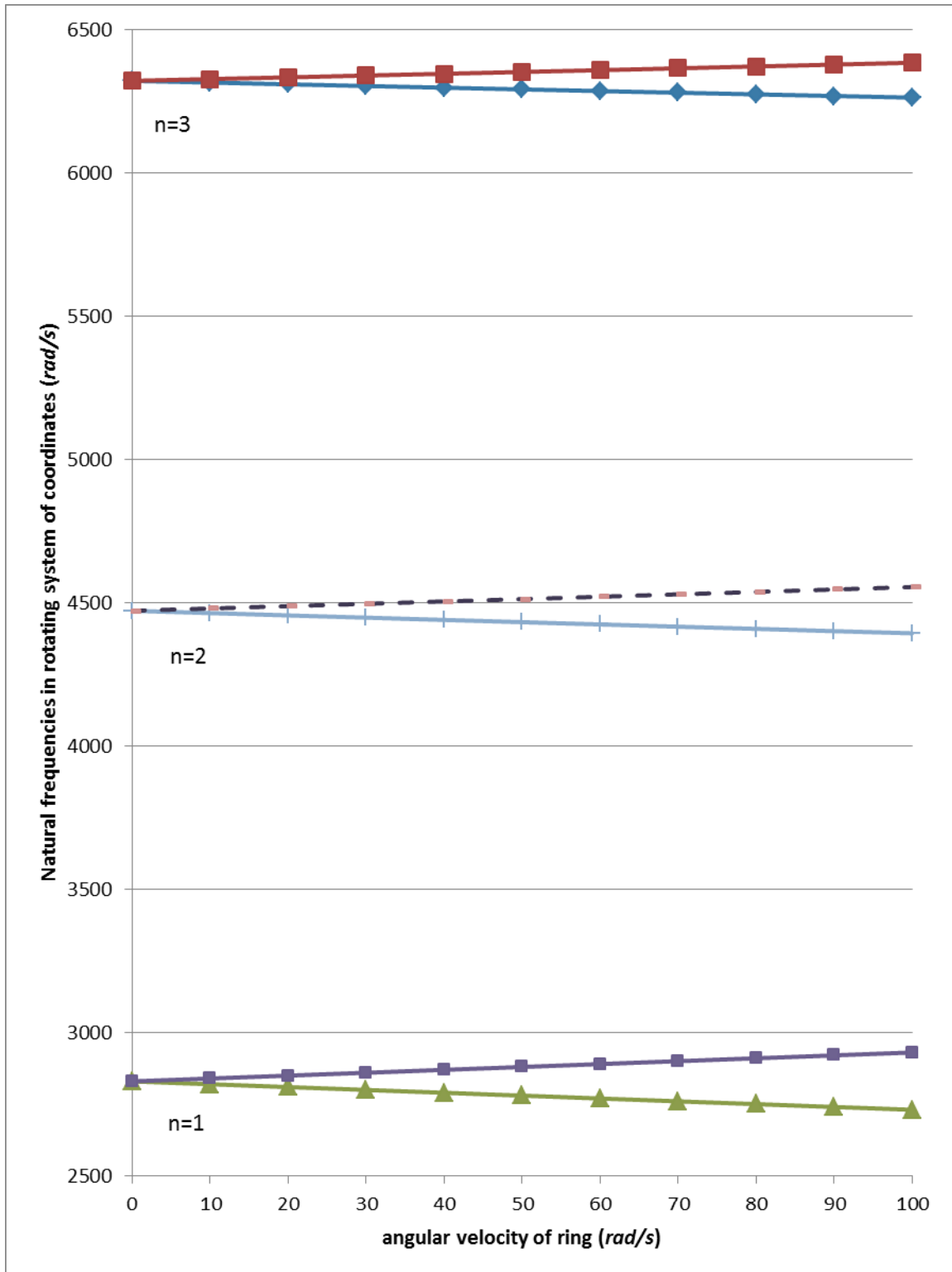


Figure 2.3: The bifurcating natural frequencies (higher than 2000 rad/s) of the center-fixed ring in the rotating system of coordinates vs. different angular velocities.

2.3. FREE VIBRATION OF A CENTER-FIXED RING IN NON-ROTATING COORDINATE SYSTEM

A tire modeled as a ring, as shown in Figure 2.1, is considered again, with the equations of motion presented in the non-rotating system of coordinates as follows:

$$\frac{EI}{a^4} \left(\frac{\partial^4 U}{\partial \varphi^4} - \frac{\partial^3 V}{\partial \varphi^3} \right) + \frac{EA}{a^2} \left(\frac{\partial V}{\partial \varphi} + U \right) - \frac{N_0}{a^2} \frac{\partial^2 U}{\partial \varphi^2} + \rho A \left(\frac{D^2 U}{Dt^2} - 2\bar{\omega} \frac{DV}{Dt} - \bar{\omega}^2 U \right) = 0 \quad (2.11)$$

$$\frac{EI}{a^4} \left(\frac{\partial^3 U}{\partial \varphi^3} - \frac{\partial^2 V}{\partial \varphi^2} \right) - \frac{EA}{a^2} \left(\frac{\partial^2 V}{\partial \varphi^2} + \frac{\partial U}{\partial \varphi} \right) + \rho A \left(\frac{D^2 V}{Dt^2} + 2\bar{\omega} \frac{DU}{Dt} - \bar{\omega}^2 V \right) = 0 \quad (2.12)$$

Here, $U(\varphi, t)$ and $V(\varphi, t)$ are defined in the non-rotating coordinate system and are functions of φ . Since φ can be written as:

$$\varphi = \theta + \bar{\omega}t \quad (2.13)$$

the first and second time derivatives of $U(\varphi, t)$ and $V(\varphi, t)$ in the non-rotating coordinate system are given by:

$$\frac{D}{Dt} = \frac{\partial}{\partial t} + \bar{\omega} \frac{\partial}{\partial \varphi} \quad (2.14)$$

$$\frac{D^2}{Dt^2} = \frac{\partial^2}{\partial t^2} + 2\bar{\omega} \frac{\partial^2}{\partial t \partial \varphi} + \bar{\omega}^2 \frac{\partial^2}{\partial \varphi^2} \quad (2.15)$$

The solution of the equations of motion is assumed to be in the form of a product of functions of position and time, in the following form:

$$U(\varphi, t) = \tilde{U}(\varphi)e^{j\omega t} \quad (2.16)$$

$$V(\varphi, t) = \tilde{V}(\varphi)e^{j\omega t} \quad (2.17)$$

Substituting Equations (2.14)– (2.17) in Equations (2.11) and (2.12) results in the following spatial differential equations:

$$\begin{aligned} \frac{EI}{a^4} \left(\frac{d^4 \tilde{U}}{d\varphi^4} - \frac{d^3 \tilde{V}}{d\varphi^3} \right) + \frac{EA}{a^2} \left(\frac{d\tilde{V}}{d\varphi} + \tilde{U} \right) - \frac{N_0}{a^2} \frac{d^2 \tilde{U}}{d\varphi^2} \\ + \rho A \left(-\omega^2 \tilde{U} + 2j\bar{\omega}\omega \frac{d\tilde{U}}{d\varphi} + \bar{\omega}^2 \frac{d^2 \tilde{U}}{d\varphi^2} - 2j\bar{\omega}\omega \tilde{V} - 2\bar{\omega}^2 \frac{d\tilde{V}}{d\varphi} - \bar{\omega}^2 \tilde{U} \right) = 0 \end{aligned} \quad (2.18)$$

$$\begin{aligned} \frac{EI}{a^4} \left(\frac{d^3 \tilde{U}}{d\varphi^3} - \frac{d^2 \tilde{V}}{d\varphi^2} \right) - \frac{EA}{a^2} \left(\frac{d^2 \tilde{V}}{d\varphi^2} + \frac{d\tilde{U}}{d\varphi} \right) \\ + \rho A \left(-\omega^2 \tilde{V} + 2j\bar{\omega}\omega \frac{d\tilde{V}}{d\varphi} + \bar{\omega}^2 \frac{d^2 \tilde{V}}{d\varphi^2} + 2j\bar{\omega}\omega \tilde{U} + 2\bar{\omega}^2 \frac{d\tilde{U}}{d\varphi} - \bar{\omega}^2 \tilde{V} \right) = 0 \end{aligned} \quad (2.19)$$

Since the response of the ring should be periodic in the circumferential direction φ , one can assume the solution in the following form:

$$\tilde{U}(\varphi) = \hat{A}e^{jn\varphi} \quad (2.20)$$

$$\tilde{V}(\varphi) = \hat{B}e^{jn\varphi} \quad (2.21)$$

where n is an integer. Therefore, the natural frequencies and the ratio of \hat{B}/\hat{A} can be obtained by solving the following eigen-value problem:

$$\begin{bmatrix} \frac{EI}{a^4}n^4 + \frac{N_0}{a^2}n^2 + \frac{EA}{a^2} - \rho A((\omega + n\bar{\omega})^2 + \bar{\omega}^2) & j\left(\frac{EI}{a^4}n^3 + \frac{EA}{a^2}n - 2\rho A\bar{\omega}(\omega + n\bar{\omega})\right) \\ -j\left(\frac{EI}{a^4}n^3 + \frac{EA}{a^2}n - 2\rho A\bar{\omega}(\omega + n\bar{\omega})\right) & \frac{EI}{a^4}n^2 + \frac{EA}{a^2}n^2 - \rho A((\omega + n\bar{\omega})^2 + \bar{\omega}^2) \end{bmatrix} \begin{bmatrix} \hat{A} \\ \hat{B} \end{bmatrix} = \begin{bmatrix} 0 \\ 0 \end{bmatrix} \quad (2.22)$$

The determinant of the equation above is calculated and solved for each n . Table 2.3 tabulates the natural frequencies of a ring with the same mechanical and geometrical properties of the ring in Section 2.2, when its angular velocity is $\bar{\omega}=100 \text{ rad/s}$. The results in this table are presented from $n=0$ to $n=10$. All the results are for the natural frequencies in the non-rotating coordinate system XZ . As can be seen, four distinct frequencies are obtained for each $n > 0$ in the case of the rotating ring in contrast to the non-rotating ring (Table 2.1) which has only two natural frequencies.

Table 2.3: The natural frequencies of a center-fixed ring rotating with an angular velocity $\bar{\omega}=100 \text{ rad/s}$ in the non-rotating coordinate system

n	$\omega \text{ (rad/s)}$			
0		2004.38		
1	2631.00	3030.99	196.18	196.19
2	4193.02	4754.41	375.24	613.84
3	5961.59	6683.28	554.96	1033.27
4	7792.29	8688.02	742.89	1447.16
5	9649.05	10727.46	940.51	1862.09
6	11519.08	12785.33	1149.34	2283.09
7	13396.78	14854.08	1371.01	2713.71
8	15279.30	16929.77	1607.10	3156.63
9	17165.04	19010.14	1859.12	3614.02
10	19053.05	21093.82	2128.46	4087.69

As explained in the previous section, the natural frequencies of a rotating ring can be specified as those corresponding to positive-going waves and to negative-going waves. This phenomenon is named the bifurcation of natural frequencies [59]. There is no

bifurcation for frequencies corresponding to $n=1$, because the positive-going waves and negative-going waves coalesce at $\omega=196.19 \text{ rad/s}$. The following calculations show the natural frequencies and the modes of a rotating ring with an angular velocity of $\bar{\omega}=100 \text{ rad/s}$ obtained for $n = +2$ and $n = -2$ separately, in the non-rotating system of coordinates XZ .

$$n = 2$$

$$\omega = \begin{cases} 4193.0157 \\ 375.2395 \\ -613.8414 \\ -4754.4138 \end{cases}$$

for $\omega = -613.8414$

$$\hat{A} = 1 \text{ and } \hat{B} = 0.5111j$$

$$U(\varphi, t) = e^{j(2\varphi - 613.8414t)}$$

$$V(\varphi, t) = 0.5111je^{j(2\varphi - 613.8414t)}$$

positive going wave

for $\omega = 375.2395$

$$\hat{A} = 1 \text{ and } \hat{B} = 0.5036j$$

$$U(\varphi, t) = e^{j(2\varphi + 375.2395t)}$$

$$V(\varphi, t) = 0.5036je^{j(2\varphi + 375.2395t)}$$

negative going wave

$$n = -2$$

$$\omega = \begin{cases} 4754.4138 \\ 613.8414 \\ -375.2395 \\ -4193.0157 \end{cases}$$

for $\omega = 613.8414$

$$\hat{A} = 1 \text{ and } \hat{B} = -0.5111j$$

$$U(\varphi, t) = e^{-j(2\varphi - 613.8414t)}$$

$$V(\varphi, t) = -0.5111je^{-j(2\varphi - 613.8414t)}$$

positive going wave

for $\omega = -375.2395$

$$\hat{A} = 1 \text{ and } \hat{B} = -0.5036j$$

$$U(\varphi, t) = e^{-j(2\varphi + 375.2395t)}$$

$$V(\varphi, t) = -0.5036je^{-j(2\varphi + 375.2395t)}$$

negative going wave

It should be noted that the multiples of the angular velocity are added to and subtracted from the positive-going and negative-going natural frequencies in the rotating coordinate system, respectively, in order to obtain the natural frequencies in the non-rotating system of coordinates. For example for $n=2$ and $\bar{\omega}=100 \text{ rad/s}$

$$n = 2 \quad \bar{\omega} = 100 \text{ rad} / \text{s}$$

positive going wave

$$\omega_{\text{rotating}} = 413.8414$$

$$\omega_{\text{non-rotating}} = 613.8414$$

$$\omega_{\text{non-rotating}} = \omega_{\text{rotating}} + 2\bar{\omega}$$

negative going wave

$$\omega_{\text{rotating}} = 575.2395$$

$$\omega_{\text{non-rotating}} = 375.2395$$

$$\omega_{\text{non-rotating}} = \omega_{\text{rotating}} - 2\bar{\omega}$$

Figure 2.4 shows the variation of natural frequencies of the center-fixed ring with the angular velocity of the ring. Figure 2.5 represents the natural frequencies above 2000 rad/s. All the frequencies are calculated in the non-rotating system of coordinates, and the bifurcation is shown. The difference between the frequencies of the positive- going and the negative-going waves increases as the rotating speed of the tire increases.

The results for each n can be split into two groups of natural frequencies: the lower frequencies and the higher frequencies. For instance as $n=2$ and $\bar{\omega}=100 \text{ rad/s}$ the couple of (375.24 , 613.84) is the group of lower frequencies. In contrast to the frequencies in the rotating coordinate system, presented in the previous section, the larger value in this group is the positive-going wave i.e. 613.84 rad/s. Also in the pair of higher frequencies, the larger value corresponds to the positive-going wave.

Figure 2.6 shows the radial displacement of the ring at different modes. It can be seen that $n=0$ corresponds to the breathing mode, whereas the bending of the ring is clear for $n=2$. The effect of the tangential displacement is more dominant at the higher frequencies obtained for each n . The lower frequencies correspond to the modes in which the effect of radial displacement is more dominant. For example for $n=2$:

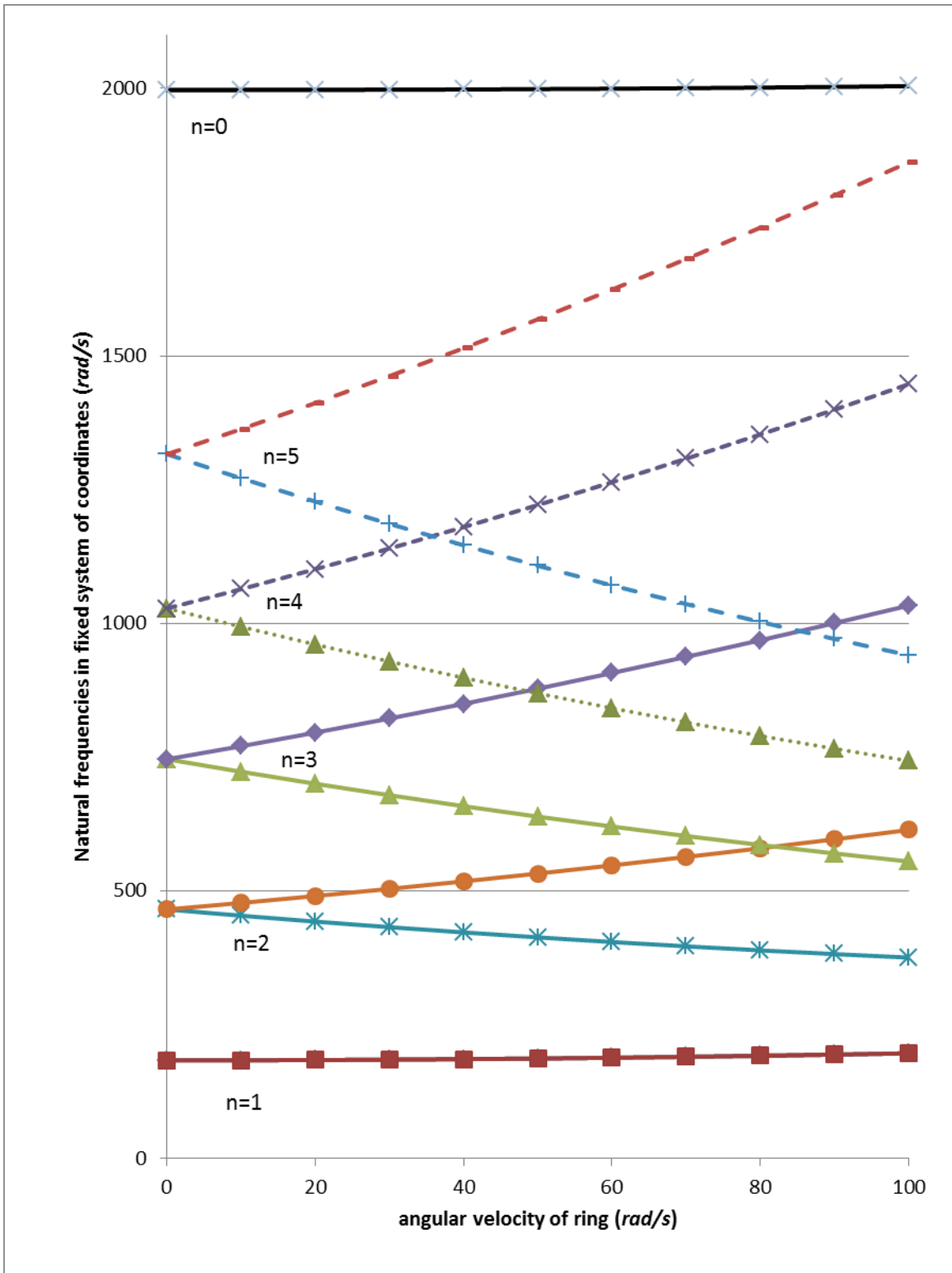


Figure 2.4: The bifurcating natural frequencies (less than 2000 rad/s) of the center-fixed ring in the non-rotating system of coordinates vs. different angular velocities.

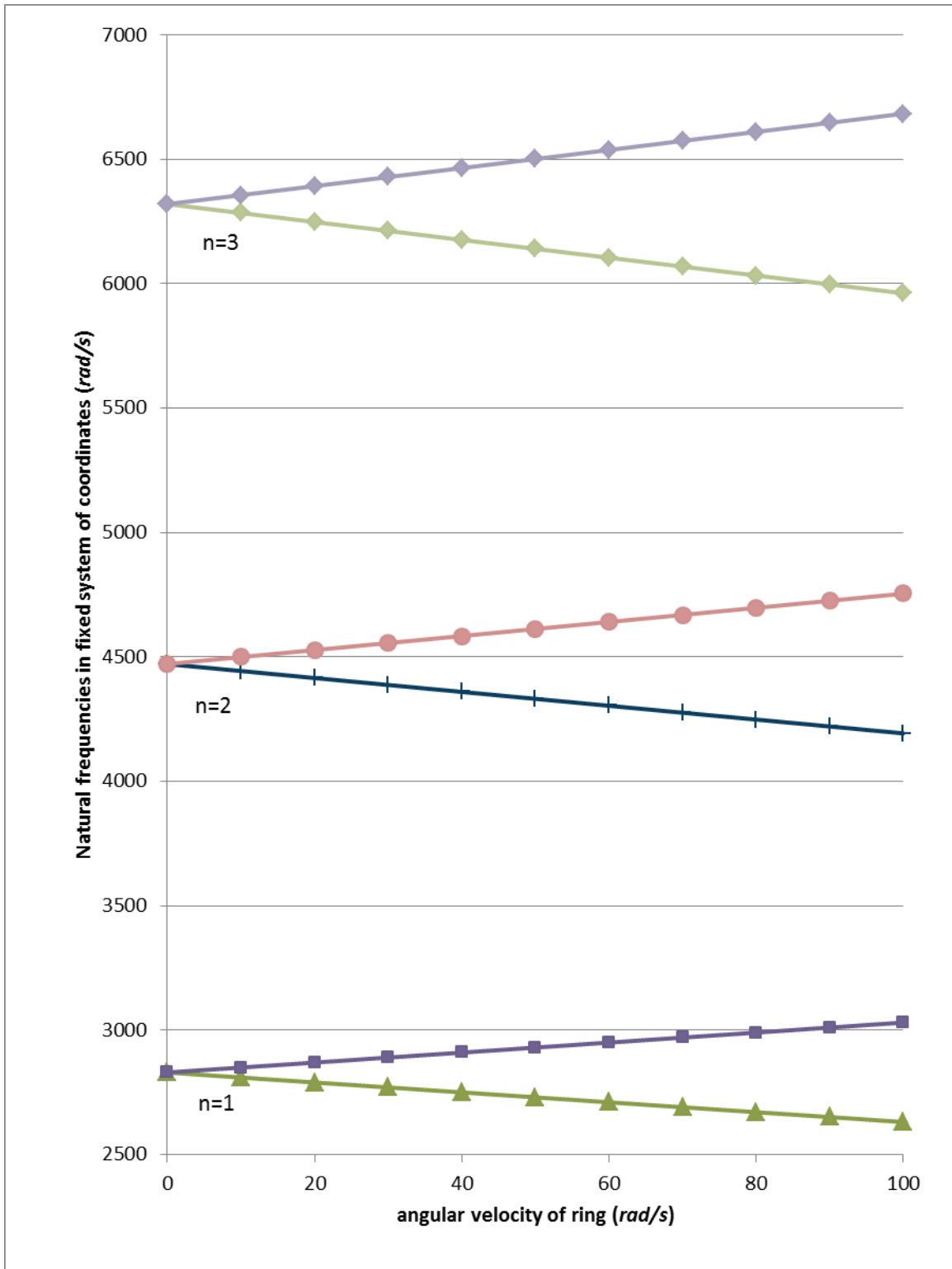


Figure 2.5: The bifurcating natural frequencies (higher than 2000 *rad/s*) of the center-fixed ring in the non-rotating system of coordinates vs. different angular velocities.

$$n = 2 \quad \omega = \begin{cases} 4193.0157 \\ 375.2395 \\ -613.8414 \\ -4754.4138 \end{cases}$$

for $\omega = 375.2395$ rad/s

$$\hat{A} = 1 \text{ and } \hat{B} = 0.5036j$$

$$U(\varphi, t) = e^{j(2\varphi + 375.2395t)}$$

$$V(\varphi, t) = 0.5036je^{j(2\varphi + 375.2395t)}$$

for $\omega = 4193.0157$ rad/s

$$\hat{A} = 1 \text{ and } \hat{B} = -2.1143j$$

$$U(\varphi, t) = e^{j(2\varphi + 4193.0157t)}$$

$$V(\varphi, t) = -2.1143je^{j(2\varphi + 375.2395t)}$$

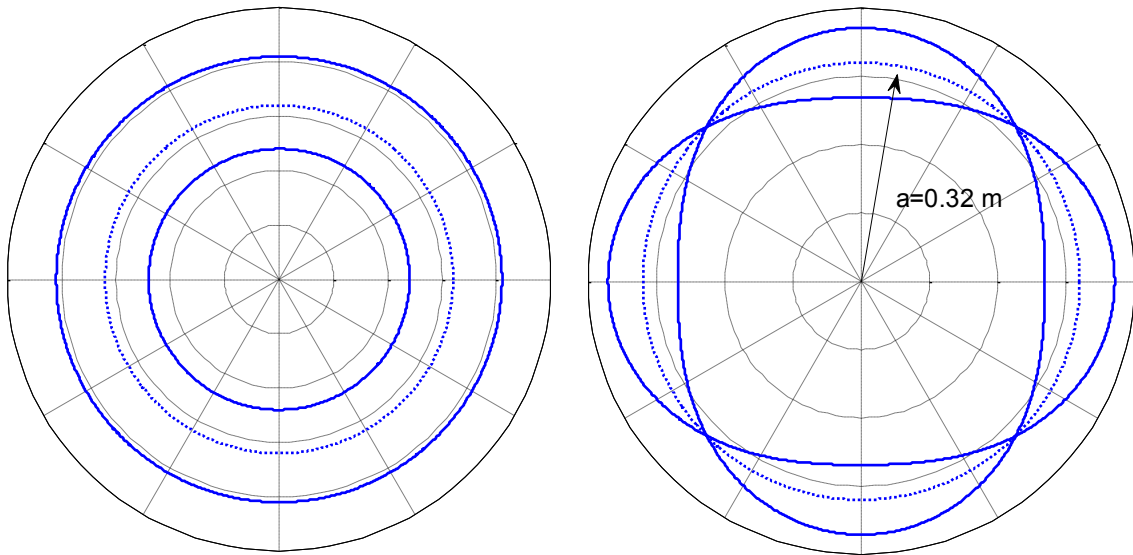


Figure 2.6: The radial displacement of a center-fixed ring for $n=0$ (left) and for $n=2$ (right)

2.4. CONCLUDING REMARKS

The equations of motion for a center-fixed ring in both the rotating and non-rotating systems of coordinates are discussed. The effects of tire-road contact and the deformation at the contact area were not taken into account. The effects of the inflation pressure of the

tire were taken into account. Also the transformation of the equations of motion from one coordinate system to another was analyzed. It was shown that the frequencies of one system of coordinates can be transformed into the frequencies of the other system of coordinates by using multiples of the angular velocity of the ring. Also the bifurcation phenomenon was shown. Bifurcation splits the natural frequencies of a non-rotating ring into two groups as the tire starts rotating. These groups are called positive-going and negative-going waves. The analysis of the modes reveals the dominance of the radial displacement at lower frequencies, whereas at the higher frequencies the tangential displacement is more dominant.

In the next chapter, the equations of the motion of the ring are used to develop the equations of the motion of the hybrid quarter-car model. This hybrid quarter-car model consists of sprung mass, a suspension system and a rotating ring as a tire that is in contact with the road.

CHAPTER 3 HYBRID QUARTER-CAR

MODEL

3.1. INTRODUCTION

In the previous chapter, the vibrations of both non-rotating and rotating center-fixed rings were discussed. The center-fixed ring is the traditional model of a tire and consists of a ring that is allowed to rotate about a fixed center. The simpler versions of this model ignore the Coriolis and centrifugal accelerations. These versions may also use the assumption of an inextensible ring, which simplifies the radial and tangential displacements. The model shown in Chapter 2 takes into account the Coriolis and the centrifugal accelerations, as well as the initial tension on the ring circumference caused by the inflation pressure and the rotations. The most important weakness of this model is that the effects of the contact of the tire with the road and of the dynamics of the vehicle body are not considered. In the present chapter, a hybrid model is presented taking into

account the significance of road contact and vehicle body inertia. This model combines a rotating ring with a discrete system that represents the vehicle body and the suspension system. Since a vehicle tire carries the dynamic loads of the vehicle system vibrations, the rotating ring is considered to be in contact with the road. Through the contact point, all the dynamic forces are applied to the hybrid system.

3.2. MODELING

A model of a vehicle with suspension system and a tire is presented in Figure 3.1. This model consists of a mass that represents the vehicle body, a rotating ring that represents the tire, and a set of spring and damper that represents the suspension system. In this model, the center of the ring can translate horizontally and vertically. The position of the center of the ring in the global system of coordinates is measured by $X_u(t)$ and $Z_u(t)$, in the horizontal and vertical directions, respectively. The vertical position of the vehicle body is denoted as $Z_s(t)$, which is also measured in the global system of coordinates. Figure 3.2 shows more details of the deflections and displacements of the ring. Two different systems of coordinates are defined: one is xz , rotating with the tire and the other is XZ , which does not rotate. The origins of both of these coordinate systems are located at the center of the ring, which is moving in both horizontal and vertical directions. The radial and tangential displacements of an arbitrary point on the ring, $U(\varphi, t)$ and $V(\varphi, t)$, respectively, are defined in the non-rotating system of coordinates, whereas the radial and tangential displacements, $u(\theta, t)$ and $v(\theta, t)$, respectively, are defined in the rotating coordinate system xz . These displacements are all measured from the center of the ring.

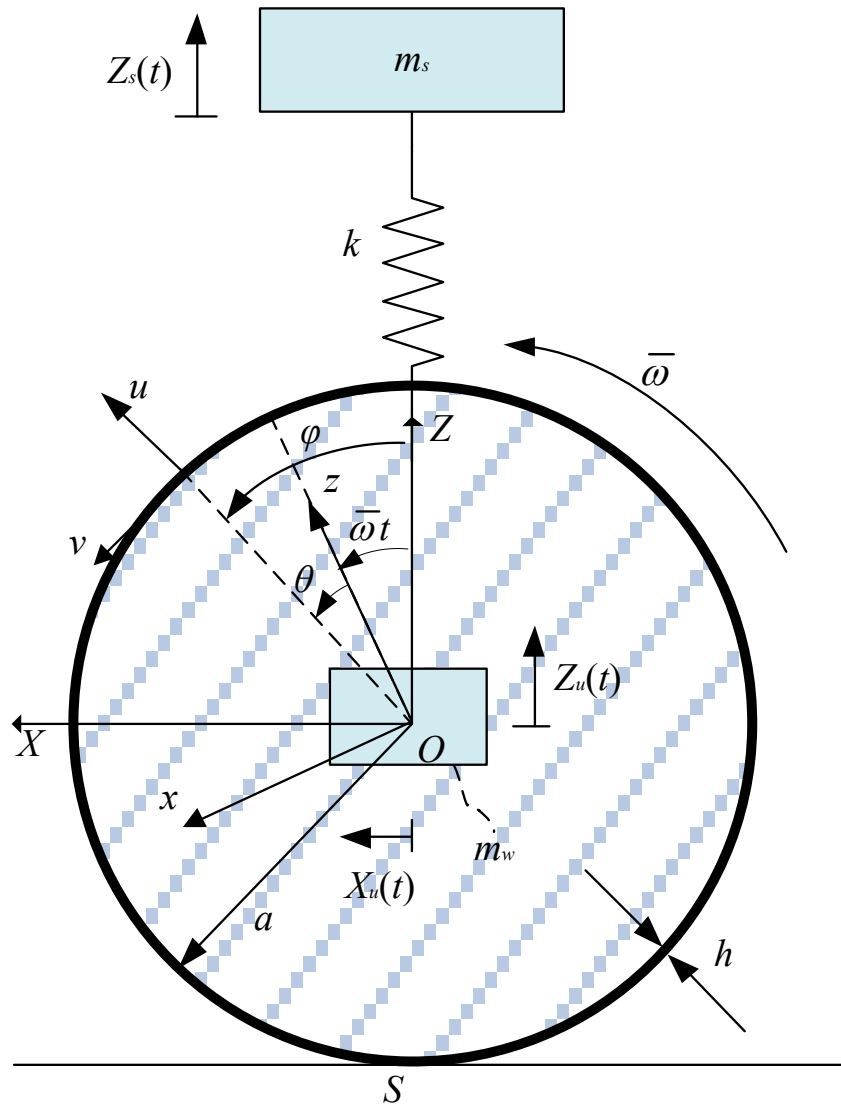


Figure 3.1: Schematic of a 2-D model of a vehicle: a rotating ring with the center that moves horizontally and vertically

It is assumed that the bottom point of the tire, S , always remains in contact with the ground and the contact force is introduced as $T(t)$. In other words, the following conditions in the dynamic solution of the model are written:

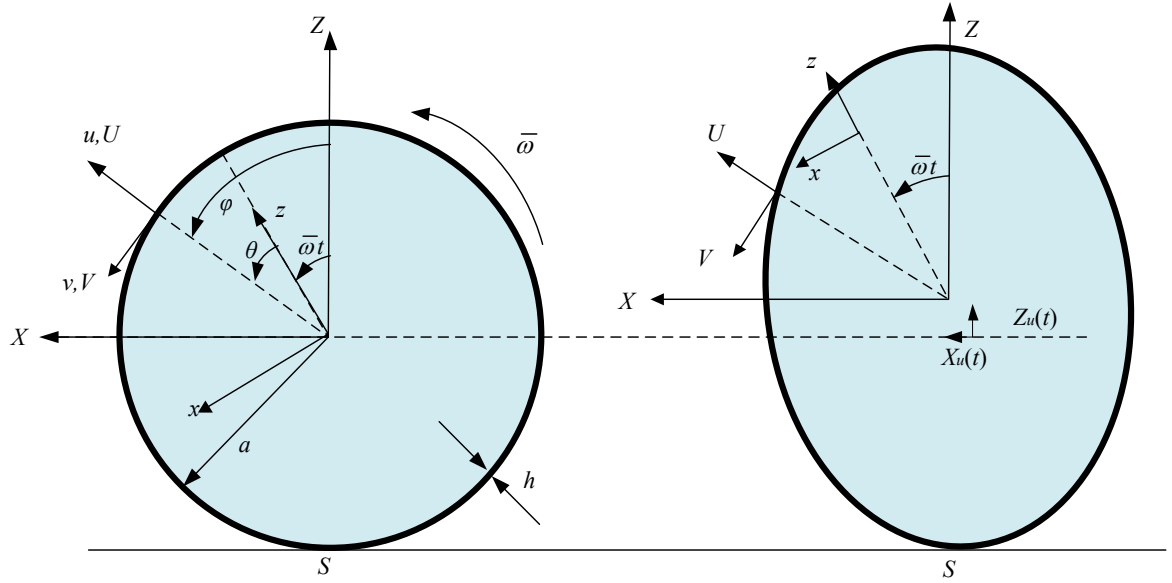


Figure 3.2: The undeformed ring (left) and the deformed ring with a free center (right)

$$X_u(t) = V(\pi, t) \quad (3.1)$$

$$Z_u(t) = U(\pi, t) \quad (3.2)$$

meaning that the radial displacement of the tire at the contact point, measured with respect to the non-rotating coordinate system XZ , causes the vertical displacement of the ring. Also the tangential displacement of the tire at the contact point causes the horizontal displacement of the ring.

In order to obtain the equations of motion, the variation of the kinetic energy of the system must be obtained. Accordingly, the velocity of an arbitrary point on the circumference of the ring in the rotating system of coordinates xz is written as:

$$\begin{aligned} \vec{V} = & \left[\dot{Z}_u \cos(\theta + \bar{\omega}t) \tilde{e}_r - \dot{Z}_u \sin(\theta + \bar{\omega}t) \tilde{e}_\theta \right] + \left[\dot{X}_u \sin(\theta + \bar{\omega}t) \tilde{e}_r + \dot{X}_u \cos(\theta + \bar{\omega}t) \tilde{e}_\theta \right] \\ & + \bar{\omega} \tilde{j} \times [(a+u) \tilde{e}_r + v \tilde{e}_\theta] + [\dot{u} \tilde{e}_r + \dot{v} \tilde{e}_\theta] \end{aligned} \quad (3.3)$$

where \tilde{e}_r is the radial unit vector and \tilde{e}_θ is the tangential unit vector. Since the total kinetic energy of the system is:

$$K = \frac{1}{2} \rho A a \int_0^{2\pi} (\vec{V} \cdot \vec{V}) d\theta + \frac{1}{2} m_w (\dot{X}_u^2 + \dot{Z}_u^2) + \frac{1}{2} m_s \dot{Z}_s^2 \quad (3.4)$$

the following equation, obtained by substituting Equation (3.3) in Equation (3.4), describes the kinetic energy in terms of the displacements in the rotating coordinate system:

$$\begin{aligned} K = & \frac{1}{2} \rho A a \int_0^{2\pi} \left(\left[\dot{u} - \bar{\omega}v + \dot{X}_u \sin(\theta + \bar{\omega}t) + \dot{Z}_u \cos(\theta + \bar{\omega}t) \right]^2 \right. \\ & \left. + \left[\dot{v} + \bar{\omega}(a+u) + \dot{X}_u \cos(\theta + \bar{\omega}t) - \dot{Z}_u \sin(\theta + \bar{\omega}t) \right]^2 \right) d\theta \\ & + \frac{1}{2} m_w (\dot{X}_u^2 + \dot{Z}_u^2) + \frac{1}{2} m_s \dot{Z}_s^2 \end{aligned} \quad (3.5)$$

Hence, in order to use the Hamilton's principle, the variation of the kinetic energy is obtained as follows:

$$\begin{aligned}
-\delta \int_{t_1}^{t_2} K dt &= \rho A a \int_{t_1}^{t_2} \int_0^{2\pi} \left[\dot{v} + 2\bar{\omega}\dot{u} - \bar{\omega}^2 v - \ddot{Z}_u \sin(\theta + \bar{\omega}t) + \ddot{X}_u \cos(\theta + \bar{\omega}t) \right] \delta v d\theta dt \\
&+ \rho A a \int_{t_1}^{t_2} \int_0^{2\pi} \left[\ddot{u} - 2\bar{\omega}\dot{v} - \bar{\omega}^2 (a+u) + \ddot{Z}_u \cos(\theta + \bar{\omega}t) + \ddot{X}_u \sin(\theta + \bar{\omega}t) \right] \delta u d\theta dt \\
&+ \rho A a \int_{t_1}^{t_2} \int_0^{2\pi} \left[\ddot{X}_u + \ddot{u} \sin(\theta + \bar{\omega}t) + \dot{v} \cos(\theta + \bar{\omega}t) \right. \\
&\quad \left. - 2\bar{\omega}\dot{v} \sin(\theta + \bar{\omega}t) + 2\bar{\omega}\dot{u} \cos(\theta + \bar{\omega}t) \right. \\
&\quad \left. - \bar{\omega}^2 v \cos(\theta + \bar{\omega}t) - \bar{\omega}^2 (a+u) \sin(\theta + \bar{\omega}t) \right] \delta X_u d\theta dt \\
&+ \rho A a \int_{t_1}^{t_2} \int_0^{2\pi} \left[\ddot{Z}_u + \ddot{u} \cos(\theta + \bar{\omega}t) - \dot{v} \sin(\theta + \bar{\omega}t) \right. \\
&\quad \left. - 2\bar{\omega}\dot{v} \cos(\theta + \bar{\omega}t) - 2\bar{\omega}\dot{u} \sin(\theta + \bar{\omega}t) \right. \\
&\quad \left. + \bar{\omega}^2 v \sin(\theta + \bar{\omega}t) - \bar{\omega}^2 (a+u) \cos(\theta + \bar{\omega}t) \right] \delta Z_u d\theta dt \\
&+ \int_{t_1}^{t_2} \left(m_w \ddot{Z}_u \delta Z_u + m_w \ddot{X}_u \delta X_u + m_s \ddot{Z}_s \delta Z_s \right) dt
\end{aligned} \tag{3.6}$$

Also the potential energy of the system is obtained as [108]:

$$\begin{aligned}
P &= \frac{1}{2} \int_0^{2\pi} \left(\frac{EI}{a^4} (u'' - v')^2 + \frac{EA}{a^2} (u + v')^2 + \frac{N_0}{a^2} u'^2 \right) a d\theta + \frac{1}{2} k (Z_u - Z_s)^2 + m_w g Z_u \\
&+ m_s g Z_s + \rho A g a \int_0^{2\pi} (Z_u + u \cos(\theta + \bar{\omega}t) - v \sin(\theta + \bar{\omega}t)) d\theta
\end{aligned} \tag{3.7}$$

in which the energy stored in the system due to bending, circumferential deformation, spring deformation, and gravity are taken into account. Therefore, using Equation (3.6) and the variation of Equation (3.7), the equations of motion can be introduced as:

$$\begin{aligned}
\frac{EI}{a^4} \left(\frac{\partial^4 u}{\partial \theta^4} - \frac{\partial^3 v}{\partial \theta^3} \right) + \frac{EA}{a^2} \left(\frac{\partial v}{\partial \theta} + u \right) - \frac{N_0}{a^2} \frac{\partial^2 u}{\partial \theta^2} + \rho A g \cos(\theta + \bar{\omega}t) \\
+ \rho A \left(\ddot{u} - 2\bar{\omega}\dot{v} - \bar{\omega}^2 (a+u) + \ddot{Z}_u \cos(\theta + \bar{\omega}t) + \ddot{X}_u \sin(\theta + \bar{\omega}t) \right) = -\frac{T_z}{a} \delta(\theta + \bar{\omega}t - \pi)
\end{aligned} \tag{3.8}$$

$$\begin{aligned}
\frac{EI}{a^4} \left(\frac{\partial^3 u}{\partial \theta^3} - \frac{\partial^2 v}{\partial \theta^2} \right) - \frac{EA}{a^2} \left(\frac{\partial^2 v}{\partial \theta^2} + \frac{\partial u}{\partial \theta} \right) - \rho A g \sin(\theta + \bar{\omega}t) \\
+ \rho A \left(\dot{v} + 2\bar{\omega}\dot{u} - \bar{\omega}^2 v - \ddot{Z}_u \sin(\theta + \bar{\omega}t) + \ddot{X}_u \cos(\theta + \bar{\omega}t) \right) = -\frac{T_x}{a} \delta(\theta + \bar{\omega}t - \pi)
\end{aligned} \tag{3.9}$$

$$\begin{aligned}
T_z &= m_w \ddot{Z}_u + m_w g + m_t \ddot{Z}_u + m_t g + k(Z_u - Z_s) \\
&+ a \rho A \int_0^{2\pi} \left(\ddot{u} \cos(\theta + \bar{\omega}t) - \ddot{v} \sin(\theta + \bar{\omega}t) - 2\bar{\omega} \dot{v} \cos(\theta + \bar{\omega}t) - 2\bar{\omega} \dot{u} \sin(\theta + \bar{\omega}t) \right. \\
&\quad \left. + \bar{\omega}^2 v \sin(\theta + \bar{\omega}t) - \bar{\omega}^2 (a + u) \cos(\theta + \bar{\omega}t) \right) d\theta
\end{aligned} \tag{3.10}$$

$$\begin{aligned}
T_x &= m_w \ddot{X}_u + m_t \ddot{X}_u \\
&+ a \rho A \int_0^{2\pi} \left(\ddot{u} \sin(\theta + \bar{\omega}t) + \ddot{v} \cos(\theta + \bar{\omega}t) - 2\bar{\omega} \dot{v} \sin(\theta + \bar{\omega}t) + 2\bar{\omega} \dot{u} \cos(\theta + \bar{\omega}t) \right. \\
&\quad \left. - \bar{\omega}^2 v \cos(\theta + \bar{\omega}t) - \bar{\omega}^2 (a + u) \sin(\theta + \bar{\omega}t) \right) d\theta
\end{aligned} \tag{3.11}$$

$$m_s \ddot{Z}_s + k(Z_s - Z_u) + m_s g = 0 \tag{3.12}$$

where T_x is the horizontal component of the force at the contact point and T_z is the vertical force. By using Equations (2.14) and (2.15), the equations of motion are transformed into the non-rotating system of coordinates as:

$$\begin{aligned}
&\frac{EI}{a^4} \left(\frac{\partial^4 U}{\partial \varphi^4} - \frac{\partial^3 V}{\partial \varphi^3} \right) + \frac{EA}{a^2} \left(\frac{\partial V}{\partial \varphi} + U \right) - \frac{N_0}{a^2} \frac{\partial^2 U}{\partial \varphi^2} + \rho A g \cos \varphi \\
&+ \rho A \left(\frac{D^2 U}{Dt^2} - 2\bar{\omega} \frac{DV}{Dt} - \bar{\omega}^2 (a + U) + \ddot{Z}_u \cos \varphi + \ddot{X}_u \sin \varphi \right) = -\frac{T_z}{a} \delta(\varphi - \pi)
\end{aligned} \tag{3.13}$$

$$\begin{aligned}
&\frac{EI}{a^4} \left(\frac{\partial^3 U}{\partial \varphi^3} - \frac{\partial^2 V}{\partial \varphi^2} \right) - \frac{EA}{a^2} \left(\frac{\partial^2 V}{\partial \varphi^2} + \frac{\partial U}{\partial \varphi} \right) - \rho A g \sin \varphi \\
&+ \rho A \left(\frac{D^2 V}{Dt^2} + 2\bar{\omega} \frac{DU}{Dt} - \bar{\omega}^2 V - \ddot{Z}_u \sin \varphi + \ddot{X}_u \cos \varphi \right) = -\frac{T_x}{a} \delta(\varphi - \pi)
\end{aligned} \tag{3.14}$$

$$m_s \ddot{Z}_s + k(Z_s - Z_u) + m_s g = 0 \tag{3.15}$$

The contact forces T_z and T_x are given by:

$$\begin{aligned}
T_z &= m_w \ddot{Z}_u + m_w g + m_t \ddot{Z}_u + m_t g + k(Z_u - Z_s) \\
&+ a \rho A \int_0^{2\pi} \left(\frac{D^2 U}{Dt^2} \cos \varphi - \frac{D^2 V}{Dt^2} \sin \varphi - 2\bar{\omega} \frac{DV}{Dt} \cos \varphi - 2\bar{\omega} \frac{DU}{Dt} \sin \varphi \right) d\varphi \\
&\quad \left(+ \bar{\omega}^2 V \sin \varphi - \bar{\omega}^2 (a + U) \cos \varphi \right)
\end{aligned} \tag{3.16}$$

$$\begin{aligned}
T_x &= m_w \ddot{X}_u + m_t \ddot{X}_u \\
&+ a \rho A \int_0^{2\pi} \left(\frac{D^2 U}{Dt^2} \sin \varphi + \frac{D^2 V}{Dt^2} \cos \varphi - 2\bar{\omega} \frac{DV}{Dt} \sin \varphi + 2\bar{\omega} \frac{DU}{Dt} \cos \varphi \right) d\varphi \\
&\quad \left(- \bar{\omega}^2 V \cos \varphi - \bar{\omega}^2 (a + U) \sin \varphi \right)
\end{aligned} \tag{3.17}$$

Substituting Equations (2.14) and (2.15) in Equations (3.16) and (3.17), and after some mathematical simplification, one can rewrite the contact forces T_z and T_x as:

$$\begin{aligned}
T_z &= m_w \ddot{Z}_u + m_w g + m_t \ddot{Z}_u + m_t g + k(Z_u - Z_s) \\
&+ a \rho A \int_0^{2\pi} (\ddot{U} \cos \varphi - \ddot{V} \sin \varphi) d\varphi \\
&+ 2\bar{\omega} a \rho A \int_0^{2\pi} (\dot{U} \cos \varphi - \dot{V} \sin \varphi)' d\varphi \\
&+ a \rho A \bar{\omega}^2 \int_0^{2\pi} (U' \cos \varphi - V' \sin \varphi - U \sin \varphi - V \cos \varphi)' d\varphi \\
&- \bar{\omega}^2 a \rho A \int_0^{2\pi} a \cos \varphi d\varphi
\end{aligned} \tag{3.18}$$

$$\begin{aligned}
T_x &= m_w \ddot{X}_u + m_t \ddot{X}_u \\
&+ a \rho A \int_0^{2\pi} (\ddot{U} \sin \varphi + \ddot{V} \cos \varphi) d\varphi \\
&+ 2\bar{\omega} a \rho A \int_0^{2\pi} (\dot{U} \sin \varphi + \dot{V} \cos \varphi)' d\varphi \\
&+ a \rho A \bar{\omega}^2 \int_0^{2\pi} (U' \sin \varphi + V' \cos \varphi + U \cos \varphi - V \sin \varphi)' d\varphi \\
&- a \rho A \bar{\omega}^2 \int_0^{2\pi} a \sin \varphi d\varphi
\end{aligned} \tag{3.19}$$

In order to satisfy the continuity conditions, the last three integrals on the right-hand side of both Equations (3.18) and (3.19) are equated to zero. The contact force components

are only functions of the accelerations of the tire. The following gives the vertical and horizontal contact forces, respectively:

$$T_z = m_w \ddot{Z}_u + m_w g + m_t \ddot{Z}_u + m_t g + k(Z_u - Z_s) + a\rho A \int_0^{2\pi} \left(\frac{\partial^2 U}{\partial t^2} \cos \varphi - \frac{\partial^2 V}{\partial t^2} \sin \varphi \right) d\varphi \quad (3.20)$$

$$T_x = m_w \ddot{X}_u + m_t \ddot{X}_u + a\rho A \int_0^{2\pi} \left(\frac{\partial^2 U}{\partial t^2} \sin \varphi + \frac{\partial^2 V}{\partial t^2} \cos \varphi \right) d\varphi \quad (3.21)$$

Equations (3.13)–(3.15) and (3.20)–(3.21) provide the equations of motion of the hybrid quarter-car model with a rotating tire. In these equations, the radial and tangential displacement of the tire, the vertical displacement of the sprung mass, and the horizontal and vertical components of the contact force are unknown.

3.3. SUMMARY

In the present chapter, a new vehicle-tire-ground model is introduced. Since this model combines the effect of the vibration of a rotating ring with the bounce vibration of the traditional quarter-car model, it is called a hybrid quarter-car model. This model takes into account the effects of the rotation including the Coriolis and centrifugal acceleration as well as the axial force at the circumference of the ring. After adding the contact point as a constraint to the hybrid quarter-car model, the equations of motion are developed and simplified according to the continuity conditions. The center of the tire was assumed to be free to move in both the vertical and horizontal directions. The contact is considered as a point through which the horizontal force T_x and the vertical force T_z are applied. These

forces are functions of the radial and tangential displacements of the tire as well as the displacements of both the center of the tire and the vehicle.

In the next chapter, the approximate solutions of the equations of motion, first by using the Galerkin method and then by using a finite element analysis are presented. Also in Chapter 5 an analytical solution of the model is presented. This model enables us to analyze the effect of tire rotation on the contact forces and on the natural frequencies and mode shapes of the system. Also the influence of the vehicle body inertia on the contact forces and the tire vibration is investigated.

CHAPTER 4 APPROXIMATE SOLUTIONS

BY GALERKIN METHOD AND FEM

4.1. INTRODUCTION

In the previous chapter, a hybrid quarter-car model consisting of a rotating ring with constraint at the bottom and a spring-mass system as the suspension and mass of the vehicle was introduced. In this chapter, the free vibration response of this model is studied by using two approximate methods. The Galerkin method with trigonometric admissible functions is used to obtain the equations of motion in the matrix form, which are solved to obtain the natural frequencies. Afterwards, a finite element model is developed by using the energy equations of the system, in order to find the natural frequencies of the quarter-car model. The natural frequencies of the hybrid quarter-car model with both non-rotating and rotating tires are obtained.

4.2. GALERKIN SOLUTION

The Galerkin method is used to solve the equations of motion of the hybrid system consisting of the rotating ring type tire and the vehicle. The effect of gravity and the static deformation of the tire are neglected in Equations (3.13), (3.14), (3.15), (3.20), and (3.21). The equations of motion are rewritten as:

$$\begin{aligned} \frac{EI}{a^4} \left(\frac{\partial^4 U}{\partial \varphi^4} - \frac{\partial^3 V}{\partial \varphi^3} \right) + \frac{EA}{a^2} \left(\frac{\partial V}{\partial \varphi} + U \right) - \frac{N_0}{a^2} \frac{\partial^2 U}{\partial \varphi^2} \\ + \rho A \left(\frac{D^2 U}{Dt^2} - 2\bar{\omega} \frac{DV}{Dt} - \bar{\omega}^2 U + \ddot{Z}_u \cos \varphi + \ddot{X}_u \sin \varphi \right) = -\frac{T_z}{a} \delta(\varphi - \pi) \end{aligned} \quad (4.1)$$

$$\begin{aligned} \frac{EI}{a^4} \left(\frac{\partial^3 U}{\partial \varphi^3} - \frac{\partial^2 V}{\partial \varphi^2} \right) - \frac{EA}{a^2} \left(\frac{\partial^2 V}{\partial \varphi^2} + \frac{\partial U}{\partial \varphi} \right) \\ + \rho A \left(\frac{D^2 V}{Dt^2} + 2\bar{\omega} \frac{DU}{Dt} - \bar{\omega}^2 V - \ddot{Z}_u \sin \varphi + \ddot{X}_u \cos \varphi \right) = -\frac{T_x}{a} \delta(\varphi - \pi) \end{aligned} \quad (4.2)$$

$$T_z = m_w \ddot{Z}_u + m_t \ddot{Z}_u + k(Z_u - Z_s) + a \rho A \int_0^{2\pi} \left(\frac{\partial^2 U}{\partial t^2} \cos \varphi - \frac{\partial^2 V}{\partial t^2} \sin \varphi \right) d\varphi \quad (4.3)$$

$$T_x = m_w \ddot{X}_u + m_t \ddot{X}_u + a \rho A \int_0^{2\pi} \left(\frac{\partial^2 U}{\partial t^2} \sin \varphi + \frac{\partial^2 V}{\partial t^2} \cos \varphi \right) d\varphi \quad (4.4)$$

$$m_s \ddot{Z}_s + k(Z_s - Z_u) = 0 \quad (4.5)$$

In order to find the solution by using the Galerkin method, a finite number of linear independent functions that satisfy all the boundary conditions are required. The solutions of the radial and tangential displacements are assumed as [109]:

$$U(\varphi, t) = \mathbf{\Phi}(\varphi) \mathbf{\alpha}(t) \quad (4.6)$$

$$V(\varphi, t) = \mathbf{\Phi}(\varphi) \mathbf{\beta}(t) \quad (4.7)$$

where, $\mathbf{\alpha}(t)$ and $\mathbf{\beta}(t)$ are unknown coefficients that should be identified by solving the eigen-value problem, and $\mathbf{\Phi}(\varphi)$ is a collection of periodic exponential functions as:

$$\mathbf{\Phi}(\varphi) = \begin{bmatrix} e^{-jn\phi} & \dots & e^{-j\phi} & 1 & e^{j\phi} & \dots & e^{jn\phi} \end{bmatrix} \quad (4.8)$$

$\mathbf{\Phi}(\varphi)$ is a $1 \times \hat{N}$ vector and $\hat{N} = 2n + 1$. The functions used in Equation (4.8) are orthogonal functions. By substituting Equations (4.6) and (4.7) in Equations (4.1)–(4.5) and integrating in the interval of $[0, 2\pi]$, one can obtain a set of \hat{N}^{th} order ordinary differential equations as follows:

$$\mathbf{M} \begin{bmatrix} \{\ddot{\mathbf{\alpha}}(t)\} \\ \{\ddot{\mathbf{\beta}}(t)\} \\ \ddot{Z}_s \end{bmatrix} + \mathbf{C} \begin{bmatrix} \{\dot{\mathbf{\alpha}}(t)\} \\ \{\dot{\mathbf{\beta}}(t)\} \\ \dot{Z}_s \end{bmatrix} + \mathbf{K} \begin{bmatrix} \{\mathbf{\alpha}(t)\} \\ \{\mathbf{\beta}(t)\} \\ Z_s \end{bmatrix} = \begin{bmatrix} \mathbf{0} \\ \mathbf{0} \\ 0 \end{bmatrix} \quad (4.9)$$

In the equation above, the mass, the damping, and the stiffness matrices are composed of sub-matrices as:

$$\mathbf{K} = \begin{bmatrix} \mathbf{K}^{11} & \mathbf{K}^{12} & -\mathbf{\Phi}^T(\pi) \frac{k}{m_t} \\ \mathbf{K}^{21} & \mathbf{K}^{22} & \mathbf{0} \\ -\frac{k}{m_s} \mathbf{\Phi}(\pi) & \mathbf{0} & \frac{k}{m_s} \end{bmatrix} \quad (4.10)$$

$$\mathbf{C} = \begin{bmatrix} \mathbf{C}^{11} & \mathbf{C}^{12} & \mathbf{0} \\ \mathbf{C}^{21} & \mathbf{C}^{22} & \mathbf{0} \\ \mathbf{0} & \mathbf{0} & \mathbf{0} \end{bmatrix} \quad (4.11)$$

$$\mathbf{M} = \begin{bmatrix} \mathbf{M}^{11} & \mathbf{M}^{12} & \mathbf{0} \\ \mathbf{M}^{21} & \mathbf{M}^{22} & \mathbf{0} \\ \mathbf{0} & \mathbf{0} & 1 \end{bmatrix} \quad (4.12)$$

By using the following operator:

$$\mathbf{D} = \text{diag}[-nj \quad \dots \quad -j \quad 0 \quad j \quad \dots \quad nj] \quad (4.13)$$

each sub-matrix is defined as:

$$\begin{aligned} \mathbf{K}^{11} &= \frac{1}{\rho A} \left(\frac{EI}{a^4} \mathbf{D}^4 + \frac{EA}{a^2} \mathbf{I} - \frac{N_0}{a^2} \mathbf{D}^2 \right) + \bar{\omega}^2 (\mathbf{D}^2 - \mathbf{I}) + \Phi^T(\pi) \frac{k}{m_t} \Phi(\pi) \\ \mathbf{K}^{12} &= \frac{1}{\rho A} \left(-\frac{EI}{a^4} \mathbf{D}^3 + \frac{EA}{a^2} \mathbf{D} \right) - 2\bar{\omega}^2 \mathbf{D} \\ \mathbf{K}^{21} &= \frac{1}{\rho A} \left(\frac{EI}{a^4} \mathbf{D}^3 - \frac{EA}{a^2} \mathbf{D} \right) + 2\bar{\omega}^2 \mathbf{D} \\ \mathbf{K}^{22} &= \frac{1}{\rho A} \left(-\frac{EI}{a^4} \mathbf{D}^2 - \frac{EA}{a^2} \mathbf{D}^2 \right) + \bar{\omega}^2 (\mathbf{D}^2 - \mathbf{I}) \end{aligned} \quad (4.14)$$

$$\begin{aligned} \mathbf{C}^{11} &= 2\bar{\omega} \mathbf{D} \\ \mathbf{C}^{12} &= -2\bar{\omega} \mathbf{I} \\ \mathbf{C}^{21} &= 2\bar{\omega} \mathbf{I} \\ \mathbf{C}^{22} &= 2\bar{\omega} \mathbf{D} \end{aligned} \quad (4.15)$$

$$\begin{aligned}
\mathbf{M}^{11} &= \mathbf{I} + \frac{1}{2\pi} \int_0^{2\pi} \mathbf{\Phi}^T(\varphi) \cos \varphi d\varphi \mathbf{\Phi}(\pi) + \left(\frac{m_w}{m_t} + 1 \right) \mathbf{\Phi}^T(\pi) \mathbf{\Phi}(\pi) \\
&\quad + \mathbf{\Phi}^T(\pi) \frac{1}{2\pi} \int_0^{2\pi} \mathbf{\Phi}(\varphi) \cos \varphi d\varphi \\
\mathbf{M}^{12} &= \frac{1}{2\pi} \int_0^{2\pi} \mathbf{\Phi}^T(\varphi) \sin \varphi d\varphi \mathbf{\Phi}(\pi) - \mathbf{\Phi}^T(\pi) \frac{1}{2\pi} \int_0^{2\pi} \mathbf{\Phi}(\varphi) \sin \varphi d\varphi \\
\mathbf{M}^{21} &= -\frac{1}{2\pi} \int_0^{2\pi} \mathbf{\Phi}^T(\varphi) \sin \varphi d\varphi \mathbf{\Phi}(\pi) + \mathbf{\Phi}^T(\pi) \frac{1}{2\pi} \int_0^{2\pi} \mathbf{\Phi}(\varphi) \sin \varphi d\varphi \\
\mathbf{M}^{22} &= \mathbf{I} + \frac{1}{2\pi} \int_0^{2\pi} \mathbf{\Phi}^T(\varphi) \cos \varphi d\varphi \mathbf{\Phi}(\pi) + \left(\frac{m_w}{m_t} + 1 \right) \mathbf{\Phi}^T(\pi) \mathbf{\Phi}(\pi) \\
&\quad + \mathbf{\Phi}^T(\pi) \frac{1}{2\pi} \int_0^{2\pi} \mathbf{\Phi}(\varphi) \cos \varphi d\varphi
\end{aligned} \tag{4.16}$$

in which \mathbf{I} is the identity matrix. The Galerkin method is used to solve the equations above. The mechanical and geometrical properties of the tire are the same as the one used in Chapter 2. The data for the sprung mass and wheel assembly mass is as follows:

$$m_s = 200 \text{ kg}, m_w = 30 \text{ kg}$$

The equivalent stiffness of the hybrid quarter-car model is obtained by analyzing the McPherson suspension spring. Figure 4.1 shows the McPherson suspension system of a vehicle. This figure shows the displacements of the sprung mass (vehicle body) and the unsprung mass (tire center) as well as the configuration of the control arm and the spring and damper.

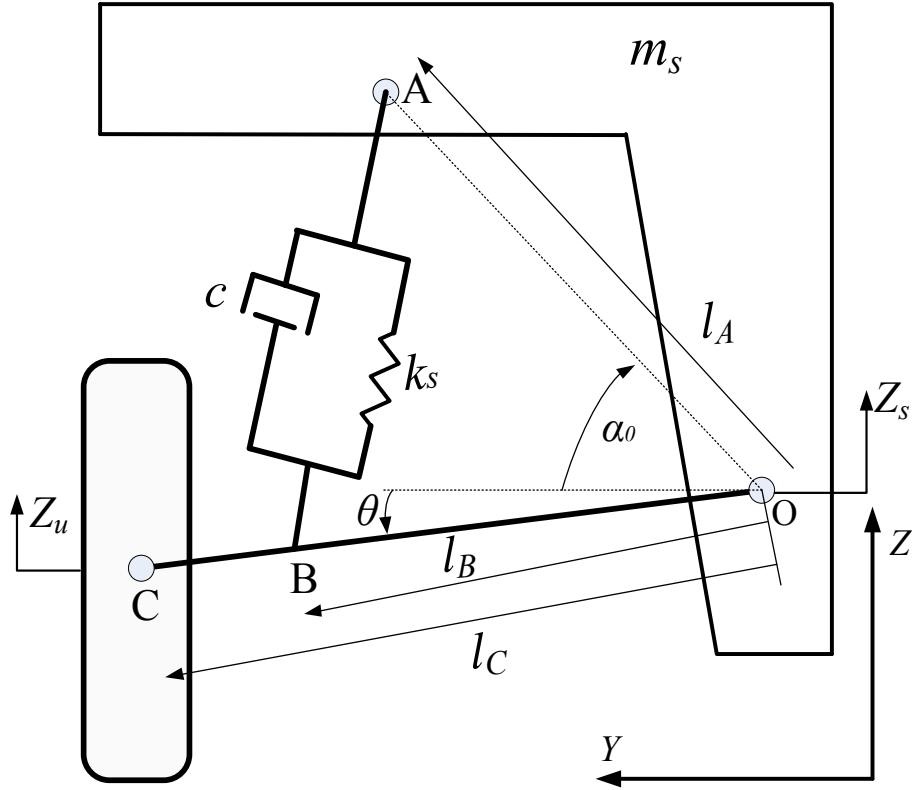


Figure 4.1: Schematic of a McPherson suspension system

The angle between the Y axis and line OA is α_0 . This angle is constant. The angular position of the control arm with respect to the Y axis is θ . The initial value of θ when the vehicle is not vibrating is called θ_0 . Accordingly, the initial length of the spring L_0 and the length of the deformed spring L can be written as:

$$L_0 = \sqrt{l_B^2 + l_A^2 + 2l_A l_B \sin \alpha \sin \theta_0 - 2l_A l_B \cos \alpha \cos \theta_0} \quad (4.17)$$

$$L = \sqrt{l_B^2 + l_A^2 + 2l_A l_B \sin \alpha \sin \theta - 2l_A l_B \cos \alpha \cos \theta} \quad (4.18)$$

The potential energy stored only at the spring can be written as the following:

$$P = \frac{1}{2} k_s (L - L_0)^2 \quad (4.19)$$

In order to linearize the equation, the variation of the potential energy is calculated as:

$$\begin{aligned} \delta P &= k_s (L - L_0) \delta L \\ &= k_s \left(1 - \frac{L_0}{L} \right) L \delta L \end{aligned} \quad (4.20)$$

where the variation of the spring length is obtained from Equation (4.18) as follows:

$$\delta L = \frac{2l_A l_B \sin \alpha \cos \theta \delta \theta + 2l_A l_B \cos \alpha \sin \theta \delta \theta}{2\sqrt{l_B^2 + l_A^2 + 2l_A l_B \sin \alpha \sin \theta} - 2l_A l_B \cos \alpha \cos \theta} \quad (4.21)$$

Substituting Equation (4.18) in Equation (4.21) results in:

$$\delta L = l_A l_B \frac{\sin \alpha \cos \theta \delta \theta + \cos \alpha \sin \theta \delta \theta}{L} \quad (4.22)$$

On the other hand, the vertical distance between point O and the center of the tire is written as:

$$l_C \sin \theta = l_C \sin \theta_0 + Z_s - Z_u \quad (4.23)$$

and its variation is written as:

$$\cos \theta \delta \theta = \frac{1}{l_C} (\delta Z_s - \delta Z_u) \quad (4.24)$$

Substituting $\delta \theta$ from Equation (4.24) in Equation (4.22) results in:

$$\delta L = \frac{l_A l_B}{l_C L} \sin \alpha (\delta Z_s - \delta Z_u) + \cos \alpha \tan \theta (\delta Z_s - \delta Z_u) \quad (4.25)$$

By using the equation above, the variation of potential energy is simplified as:

$$\delta P = k_s \left(1 - \frac{L_0}{L} \right) \frac{l_A l_B}{l_C} (\sin \alpha + \cos \alpha \tan \theta) (\delta Z_s - \delta Z_u) \quad (4.26)$$

Neglecting the ratio of initial length to actual length of the spring L_0/L , the variation of the potential energy stored at the spring is linearized as:

$$\delta P = k_s \frac{l_A l_B}{l_C} (\sin \alpha + \cos \alpha \tan \theta_0) (\delta Z_s - \delta Z_u) \quad (4.27)$$

Consequently, the equivalent spring is defined as:

$$k = k_s \frac{l_A l_B}{l_C} (\sin \alpha + \cos \alpha \tan \theta_0) \quad (4.28)$$

The information provided in [7], [110] is used to calculate the equivalent stiffness of the McPherson suspension system as:

$$k=17800 \text{ N/m}$$

Table 4.1 shows the natural frequencies of the quarter car model with a non-rotating ring i.e. a stationary vehicle. It should be noted that n refers to the highest harmonic of trigonometric functions used in Equation (4.8), and \hat{N} refers to the total number of admissible functions. For example, $n=5$ means that $\hat{N}=11$ functions are used as admissible functions. Figure 4.2 and Figure 4.3 present the rate of convergence for the

data shown in Table 4.1. The comparison has been done for the results of $n=1$ to $n=5$, where more than three frequencies are available. They are all normalized with respect to the frequencies obtained for $n=5$. The frequencies below 1000 rad/s are compared in Figure 4.2. The maximum error is about 17% where only three functions as $\begin{bmatrix} e^{-j\varphi} & 1 & e^{j\varphi} \end{bmatrix}$ are used. The convergence speeds up as the number of admissible functions is increased. Figure 4.3 demonstrates the convergence rate of the frequencies above 1000 rad/s when $\bar{\omega}=0$. All frequencies converge very quickly so that the use of few functions seems satisfactory, except for the breathing mode with $\omega=1905.483 \text{ rad/s}$.

Table 4.2 presents the natural frequencies of the hybrid quarter-car model when the tire rotates with angular velocity $\bar{\omega}=100 \text{ rad/s}$. The natural frequencies are not much different from those of the non-rotating ring, but there is a considerable difference between these results and those of the conventional model. It must be noted that the frequencies of the system at different rotating velocities are compared in the next chapter, and only the convergence of the results is considered in this chapter. All the frequencies of the hybrid quarter-car model are calculated in the non-rotating coordinate system.

Table 4.1: The natural frequencies of the hybrid quarter-car model with a non-rotating ring $\bar{\omega} = 0$ for the different number of functions employed in the Galerkin Method

$n=0$ $\hat{N} = 1$	$n=1$ $\hat{N} = 3$	$n=2$ $\hat{N} = 5$	$n=3$ $\hat{N} = 7$	$n=4$ $\hat{N} = 9$	$n=5$ $\hat{N} = 11$
9.480	8.739	8.577	8.508	8.400	8.378
	63.650	57.893	55.900	54.899	54.303
	141.822	140.525	140.266	140.173	140.135
		321.305	304.441	297.024	292.876
		427.245	425.583	425.097	424.890
			629.217	611.551	602.829
			718.655	717.349	716.895
				924.117	907.141
				1005.895	1004.832
					1217.920
					1296.345
583.877	1302.540	1649.652	1790.868	1861.938	1905.483
	2316.856	2289.179	2282.010	2281.390	2284.443
	2510.260	2578.853	2637.716	2679.794	2710.364
		3852.260	3771.079	3732.847	3710.664
		4317.903	4351.090	4375.411	4392.647
			5715.085	5620.508	5570.825
			6236.691	6252.064	6263.629
				7657.796	7560.753
				8186.488	8194.657
					9628.651
					10151.570

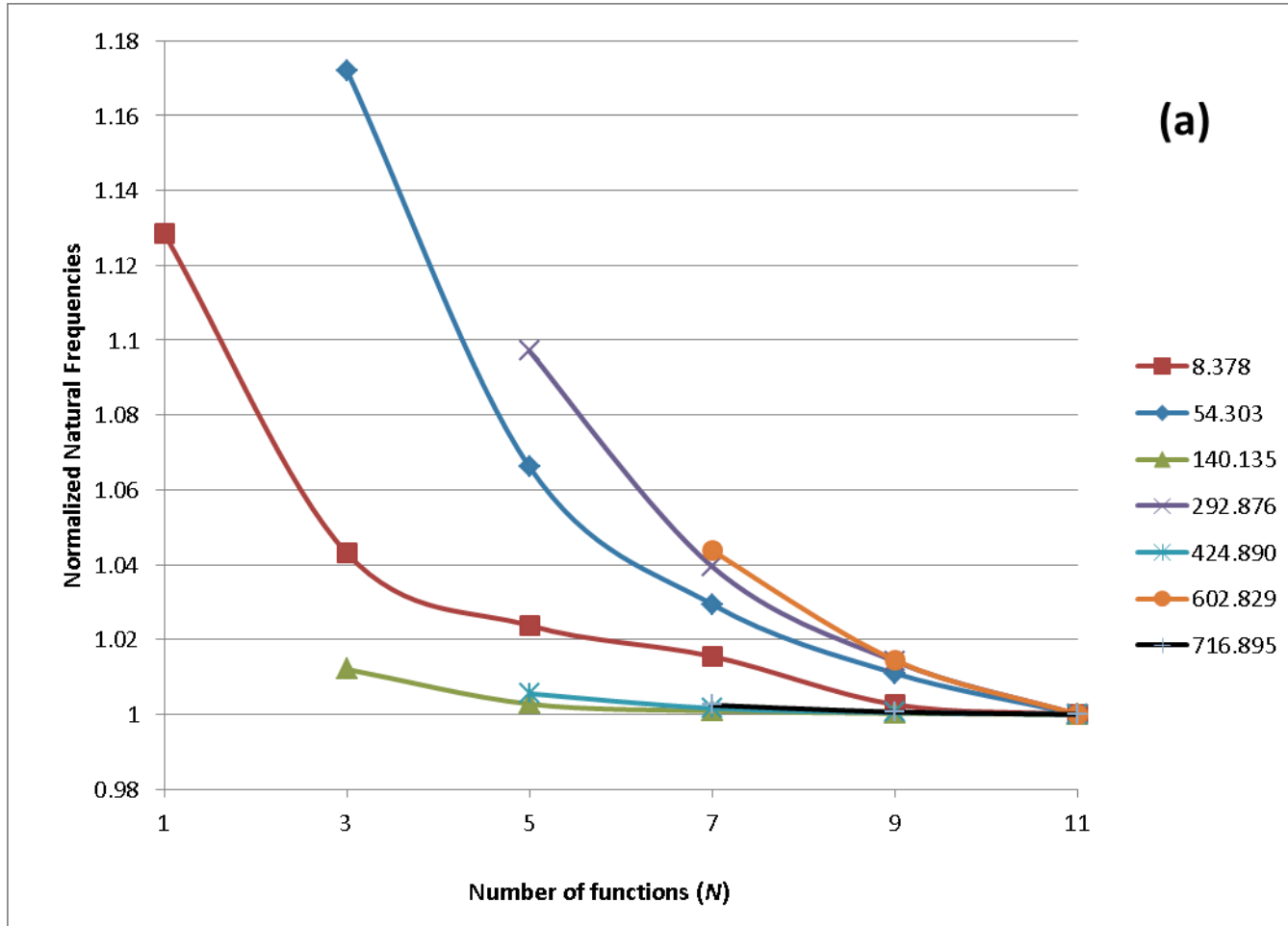


Figure 4.2: The convergence rate of the natural frequencies of a hybrid quarter-car model with a non-rotating ring vs. the number of functions applied in the Galerkin method (frequencies lower than 1000 rad/s)

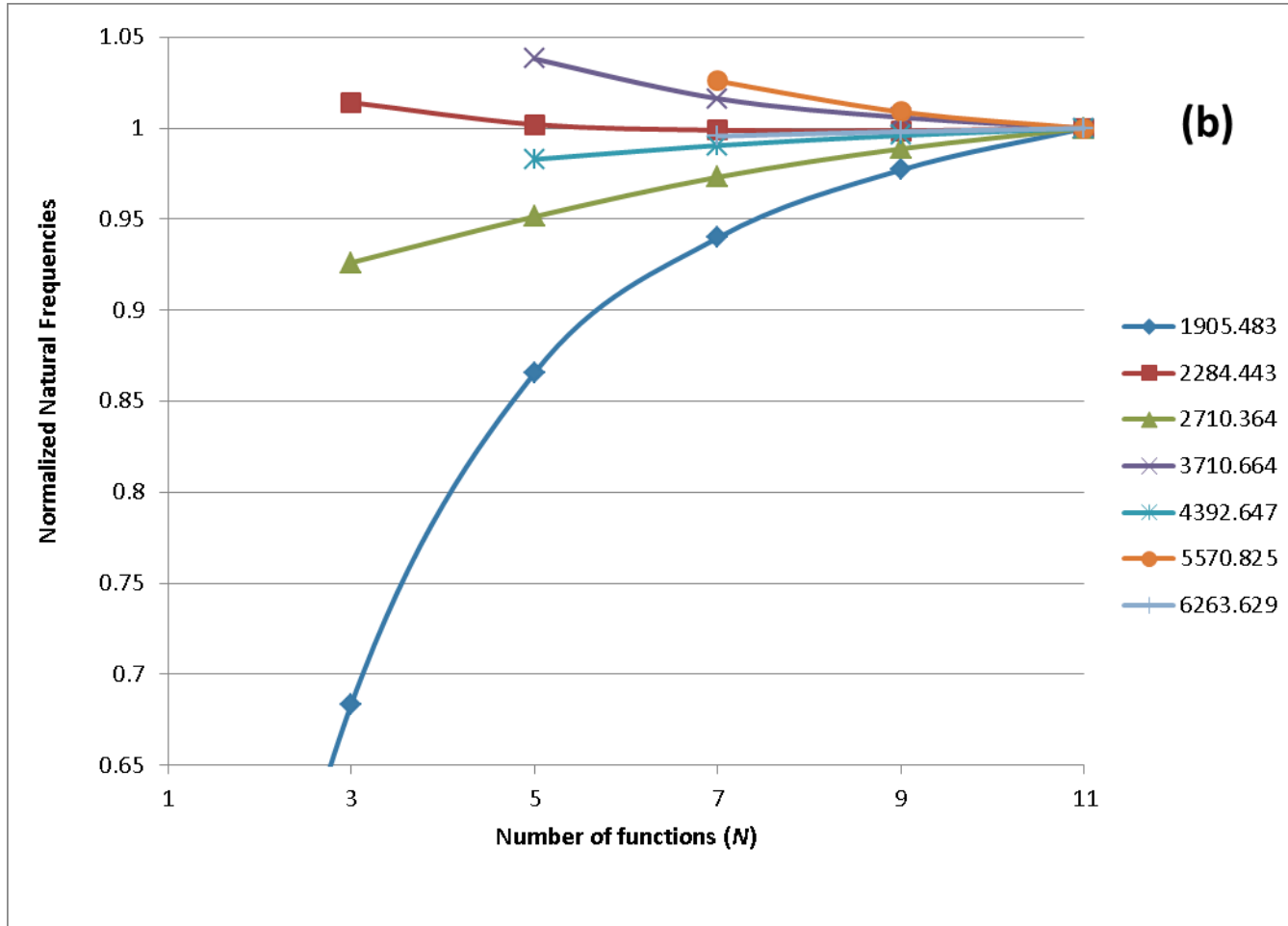


Figure 4.3: The convergence rate of the natural frequencies of a hybrid quarter-car model with a non-rotating ring vs. the number of functions applied in the Galerkin method (frequencies higher than 1000 rad/s)

Table 4.2: The natural frequencies of the hybrid quarter-car model with a rotating ring with $\bar{\omega}=100$ rad/s, for a different number of functions employed in the Galerkin Method

$n=0$ $\hat{N} = 1$	$n=1$ $\hat{N} = 3$	$n=2$ $\hat{N} = 5$	$n=3$ $\hat{N} = 7$	$n=4$ $\hat{N} = 9$	$n=5$ $\hat{N} = 11$
9.480	8.826	8.670	8.585	8.547	8.524
	67.492	60.819	58.467	57.300	56.608
	137.801	135.401	134.903	134.728	134.650
		308.233	298.400	293.791	291.127
		477.174	443.259	433.489	428.527
			543.779	543.088	542.784
			900.333	699.971	694.101
				903.585	856.794
				1320.416	951.636
					1313.869
					1723.260
583.394	1303.650	1651.749	1793.582	1866.833	1926.020
	2233.986	2233.021	2243.285	2255.756	2271.841
	2594.544	2632.548	2673.658	2705.403	2730.002
		3759.752	3708.821	3686.143	3673.799
		4418.358	4415.781	4422.282	4428.669
			5580.805	5523.585	5493.548
			6384.655	6351.660	6338.860
				7464.196	7413.760
				8400.368	8344.133
					9366.577
					10443.079

Since the natural frequencies tabulated in Table 4.2 belong to the hybrid system, whole the system undergoes a vibration at each frequency. However, at each frequency the magnitude of one of the displacements may be higher than the others. For instance, the first frequency correspond to the vehicle bounce mode and the displacement of the sprung mass is larger. The mode shapes are plotted in the next chapter.

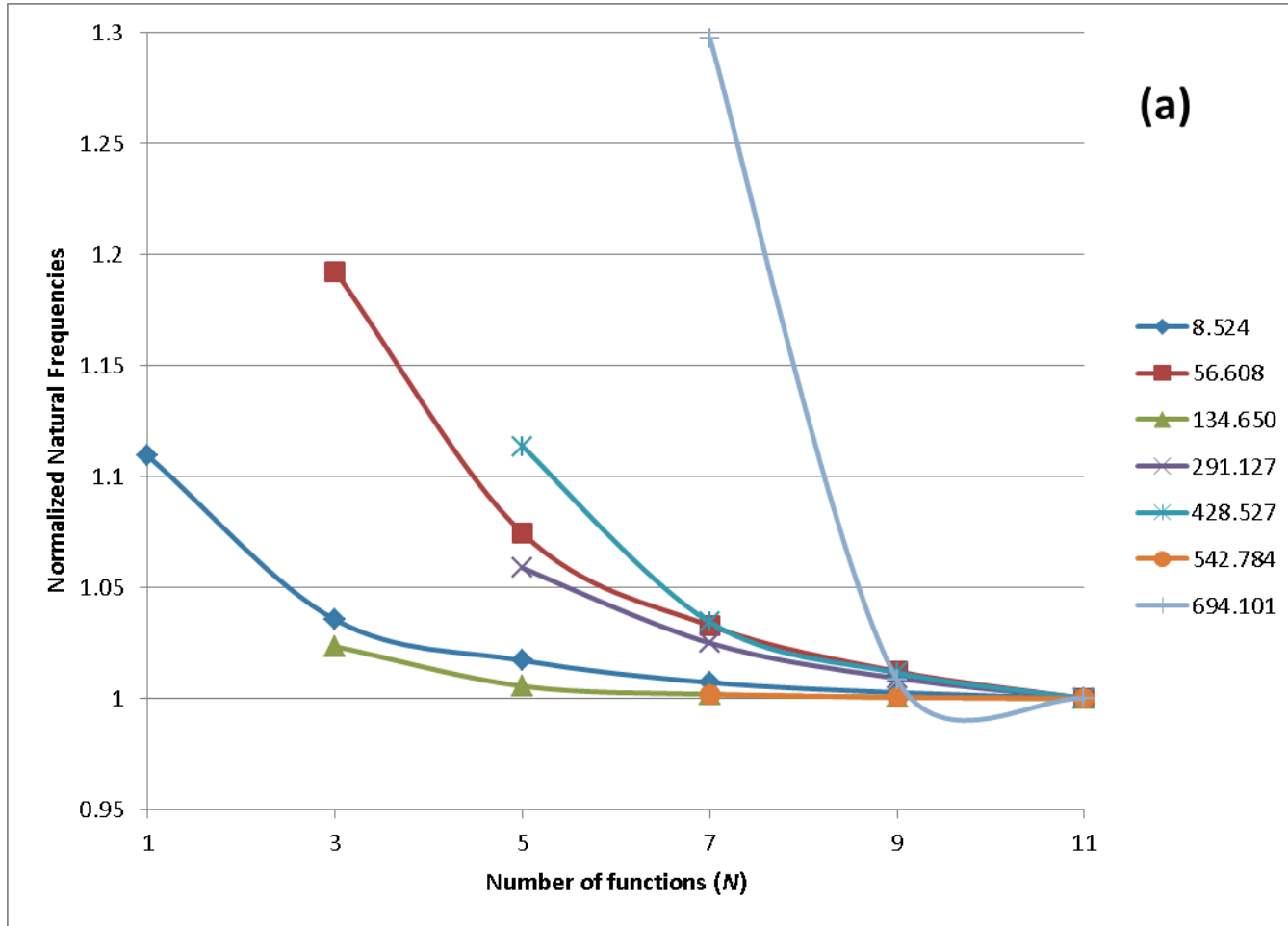


Figure 4.4: The convergence rate of the natural frequencies of a quarter-car model with a rotating ring $\bar{\omega}=100 \text{ rad/s}$ vs. the number of functions applied in the Galerkin method (frequencies lower than 1000 rad/s)

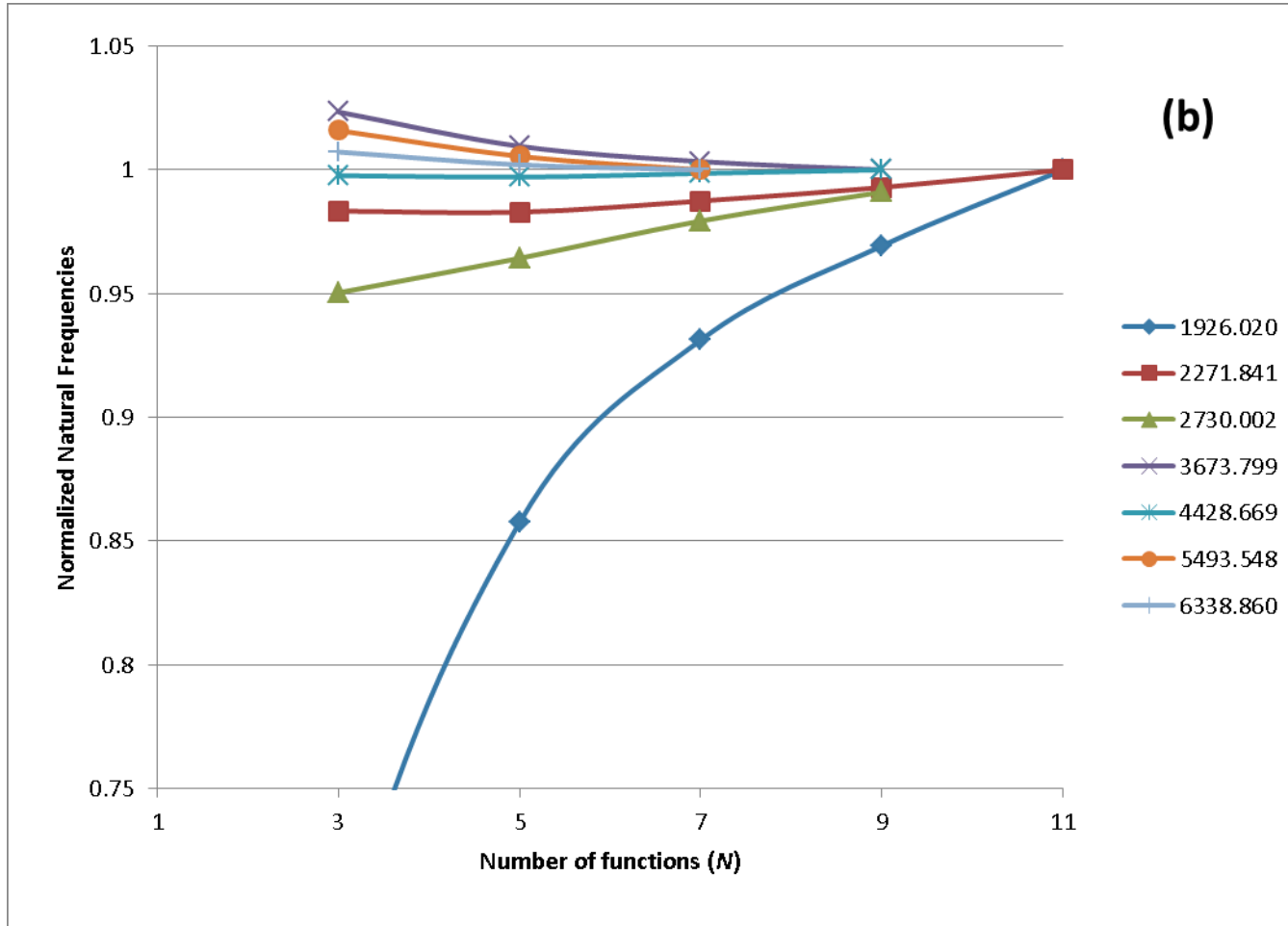


Figure 4.5: The convergence rate of the natural frequencies of a quarter-car model with a rotating ring $\bar{\omega}=100 \text{ rad/s}$ vs. the number of functions applied in the Galerkin method (frequencies higher than 1000 rad/s)

Figure 4.4 and Figure 4.5 show the normalized natural frequencies of the hybrid quarter-car model with a rotating ring. The convergence of the frequencies obtained by using a different number of functions (maximum $n=5$) is compared. Adding the number of functions reveals a greater number of natural frequencies. It can be seen that the convergence rate significantly increases when more than three functions are used. However, the use of less than three functions is not recommended.

4.3. FINITE ELEMENT METHOD

The rotating ring type model for a tire is modeled with curved beam finite elements. Figure 4.6 presents a curved element that is used in the finite element model. It is assumed that the radial and tangential displacements at any arbitrary position of the element can be described by the following equations, respectively.

$$v(\beta) = [\mathbf{d}][\boldsymbol{\psi}] \quad (4.29)$$

$$u(\beta) = [\mathbf{c}][\boldsymbol{\psi}] \quad (4.30)$$

where $[\mathbf{d}]$ and $[\mathbf{c}]$ vectors consist of six unknown elements, each as follows:

$$[\mathbf{d}] = [d_1 \ d_2 \ d_3 \ d_4 \ d_5 \ d_6] \quad (4.31)$$

$$[\mathbf{c}] = [c_1 \ c_2 \ c_3 \ c_4 \ c_5 \ c_6] \quad (4.32)$$

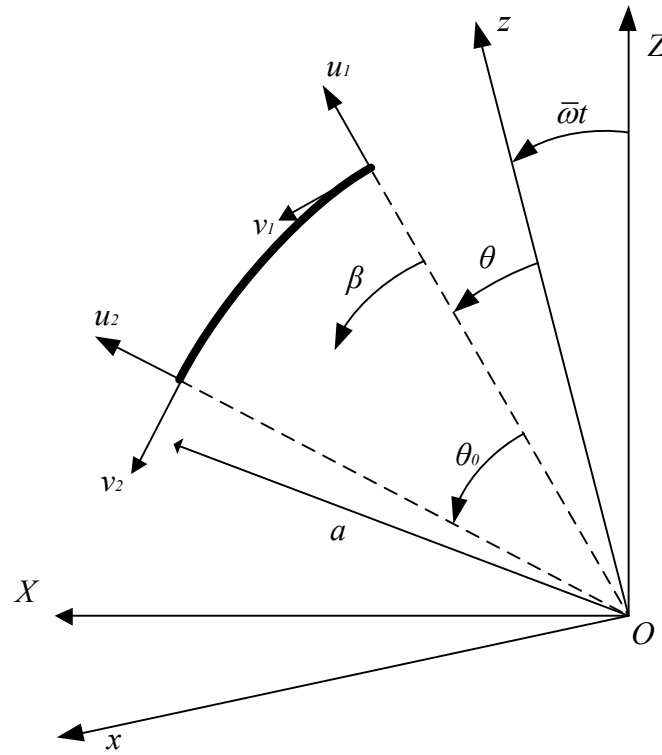


Figure 4.6: A curved beam element for the circular ring

and $[\psi(\beta)]$ is a spatial vector. This is used as a vector of shape functions obtained by using differential equations of static deformation of the element as [111]:

$$[\psi(\beta)] = [1 \quad \beta \quad \sin \beta \quad \cos \beta \quad \beta \sin \beta \quad \beta \cos \beta]^T \quad (4.33)$$

The spatial derivative of the vector of interpolating functions is written as:

$$[\psi'(\beta)] = \mathbf{D}[\psi(\beta)] \quad (4.34)$$

where \mathbf{D} is defined as:

$$\mathbf{D} = \begin{bmatrix} 0 & 0 & 0 & 0 & 0 & 0 \\ 1 & 0 & 0 & 0 & 0 & 0 \\ 0 & 0 & 0 & 1 & 0 & 0 \\ 0 & 0 & -1 & 0 & 0 & 0 \\ 0 & 0 & 1 & 0 & 0 & 1 \\ 0 & 0 & 0 & 1 & -1 & 0 \end{bmatrix} \quad (4.35)$$

Then by considering static curved-beam equations, the coefficient of $[\mathbf{c}]$ can be written in terms of $[\mathbf{d}]$ as:

$$[\mathbf{c}] = [\mathbf{d}] \mathbf{T}_1 \quad (4.36)$$

where \mathbf{T}_1 is:

$$\mathbf{T}_1 = \left(\frac{EI}{a^4} \mathbf{D}^3 - \frac{EA}{a^2} \mathbf{D} \right) \left(\frac{EI}{a^4} \mathbf{D}^4 + \frac{EA}{a^2} \mathbf{I} - \frac{N_0}{a^2} \mathbf{D}^2 \right)^{-1} \quad (4.37)$$

Vector \mathbf{U} is defined as follows to obtain the coefficients in vector $[\mathbf{d}]$ in terms of the radial and tangential displacements of the endpoints and in terms of the slope at the end points as follows:

$$\mathbf{U} = \begin{bmatrix} v_j & u_j & u_j^p & v_{j+1} & u_{j+1} & u_{j+1}^p \end{bmatrix} \quad (4.38)$$

By using Equations (4.29), (4.30), (3.35), and (4.36), \mathbf{U} can be written as:

$$\mathbf{U} = \mathbf{d} [\boldsymbol{\psi}(0) \quad \mathbf{T}_1 \boldsymbol{\psi}(0) \quad \mathbf{T}_1 \mathbf{D} \boldsymbol{\psi}(0) \quad \boldsymbol{\psi}(\theta_0) \quad \mathbf{T}_1 \boldsymbol{\psi}(\theta_0) \quad \mathbf{T}_1 \mathbf{D} \boldsymbol{\psi}(\theta_0)] \quad (4.39)$$

Therefore, the vector $[\mathbf{d}]$ can be rewritten as:

$$[\mathbf{d}] = \mathbf{U} \mathbf{T}_2 \quad (4.40)$$

where,

$$\mathbf{T}_2 = [\boldsymbol{\Psi}(0) \quad \mathbf{T}_1\boldsymbol{\Psi}(0) \quad \mathbf{T}_1\mathbf{D}\boldsymbol{\Psi}(0) \quad \boldsymbol{\Psi}(\theta_0) \quad \mathbf{T}_1\boldsymbol{\Psi}(\theta_0) \quad \mathbf{T}_1\mathbf{D}\boldsymbol{\Psi}(\theta_0)]^{-1} \quad (4.41)$$

The potential energy of a curved beam can be written as:

$$P = \frac{1}{2} \int_0^{\theta_0} \left(\frac{EI}{a^4} (u'' - v')^2 + \frac{EA}{a^2} (u + v')^2 + \frac{N_0}{a^2} u'^2 \right) a d\beta \quad (4.42)$$

However, to use the finite element method, the potential energy is sought in the form of:

$$P = \frac{1}{2} \mathbf{U} \mathbf{K} \mathbf{U}^T \quad (4.43)$$

Transforming all the unknown coefficients to \mathbf{U} , the following equation for the stiffness matrix of such an element is obtained:

$$\begin{aligned} \mathbf{K} = & \frac{EI}{a^4} (\mathbf{T}_2 \mathbf{T}_1 \mathbf{D}^2 - \mathbf{T}_2 \mathbf{D}) \int_0^{\theta_0} ([\boldsymbol{\Psi}][\boldsymbol{\Psi}]^T) a d\beta (\mathbf{T}_2 \mathbf{T}_1 \mathbf{D}^2 - \mathbf{T}_2 \mathbf{D})^T \\ & + \frac{EA}{a^2} (\mathbf{T}_2 \mathbf{T}_1 + \mathbf{T}_2 \mathbf{D}) \int_0^{\theta_0} ([\boldsymbol{\Psi}][\boldsymbol{\Psi}]^T) a d\beta (\mathbf{T}_2 \mathbf{T}_1 + \mathbf{T}_2 \mathbf{D})^T \\ & + \frac{N_0}{a^2} (\mathbf{T}_2 \mathbf{T}_1 \mathbf{D}) \int_0^{\theta_0} ([\boldsymbol{\Psi}][\boldsymbol{\Psi}]^T) a d\beta \mathbf{D}^T \mathbf{T}_1^T \mathbf{T}_2^T \end{aligned} \quad (4.44)$$

The kinetic energy of the curved beam as a function of u , v , X_u and Z_u is written as follows:

$$\begin{aligned} K = & \frac{1}{2} \rho A a \int_0^{\theta_0} \left(\left[\dot{u} - \bar{\omega} v + \dot{X}_u \sin(\beta + \theta + \bar{\omega} t) + \dot{Z}_u \cos(\beta + \theta + \bar{\omega} t) \right]^2 \right. \\ & \left. + \left[\dot{v} + \bar{\omega}(a + u) + \dot{X}_u \cos(\beta + \theta + \bar{\omega} t) - \dot{Z}_u \sin(\beta + \theta + \bar{\omega} t) \right]^2 \right) d\beta \end{aligned} \quad (4.45)$$

The radial and tangential displacements are replaced by \mathbf{U} , and the kinetic energy is rewritten. The variation of the kinetic energy of the element in a non-rotating coordinate system is written as follows:

$$\begin{aligned}
& -\delta K / (\rho A a) = \\
& \delta \mathbf{U} \mathbf{T}_2 \int_0^{\theta_0} [\boldsymbol{\Psi}] [\boldsymbol{\Psi}]^T d\beta \mathbf{T}_2^T \dot{\mathbf{U}}^T + 2\bar{\omega} \delta \mathbf{U} \mathbf{T}_2 \int_0^{\theta_0} [\boldsymbol{\Psi}] [\boldsymbol{\Psi}]^T d\beta \mathbf{D}^T \mathbf{T}_2^T \dot{\mathbf{U}}^T \\
& \quad + \bar{\omega}^2 \delta \mathbf{U} \mathbf{T}_2 \int_0^{\theta_0} [\boldsymbol{\Psi}] [\boldsymbol{\Psi}]^T d\beta (\mathbf{D}^T)^2 \mathbf{T}_2^T \mathbf{U}^T \\
& + 2\bar{\omega} \delta \mathbf{U} \mathbf{T}_2 \int_0^{\theta_0} [\boldsymbol{\Psi}] [\boldsymbol{\Psi}]^T d\beta \mathbf{T}_1^T \mathbf{T}_2^T \dot{\mathbf{U}}^T + 2\bar{\omega}^2 \delta \mathbf{U} \mathbf{T}_2 \int_0^{\theta_0} [\boldsymbol{\Psi}] [\boldsymbol{\Psi}]^T d\beta \mathbf{D}^T \mathbf{T}_1^T \mathbf{T}_2^T \mathbf{U}^T \\
& - \bar{\omega}^2 \delta \mathbf{U} \mathbf{T}_2 \int_0^{\theta_0} [\boldsymbol{\Psi}] [\boldsymbol{\Psi}]^T d\beta \mathbf{T}_2^T \mathbf{U}^T \\
& - \delta \mathbf{U} \mathbf{T}_2 \int_0^{\theta_0} [\boldsymbol{\Psi}] \sin(\theta + \beta + \bar{\omega}t) d\beta \ddot{Z}_u \\
& + \delta \mathbf{U} \mathbf{T}_2 \int_0^{\theta_0} [\boldsymbol{\Psi}] \cos(\theta + \beta + \bar{\omega}t) d\beta \ddot{X}_u \\
& + \delta \mathbf{U} \mathbf{T}_2 \mathbf{T}_1 \int_0^{\theta_0} [\boldsymbol{\Psi}] [\boldsymbol{\Psi}]^T d\beta \mathbf{T}_1^T \mathbf{T}_2^T \dot{\mathbf{U}}^T + 2\bar{\omega} \delta \mathbf{U} \mathbf{T}_2 \mathbf{T}_1 \int_0^{\theta_0} [\boldsymbol{\Psi}] [\boldsymbol{\Psi}]^T d\beta \mathbf{D}^T \mathbf{T}_1^T \mathbf{T}_2^T \dot{\mathbf{U}}^T \\
& \quad + \bar{\omega}^2 \delta \mathbf{U} \mathbf{T}_2 \mathbf{T}_1 \int_0^{\theta_0} [\boldsymbol{\Psi}] [\boldsymbol{\Psi}]^T d\beta (\mathbf{D}^T)^2 \mathbf{T}_1^T \mathbf{T}_2^T \mathbf{U}^T \\
& - 2\bar{\omega} \delta \mathbf{U} \mathbf{T}_2 \mathbf{T}_1 \int_0^{\theta_0} [\boldsymbol{\Psi}] [\boldsymbol{\Psi}]^T d\beta \mathbf{T}_2^T \dot{\mathbf{U}}^T - 2\bar{\omega}^2 \delta \mathbf{U} \mathbf{T}_2 \mathbf{T}_1 \int_0^{\theta_0} [\boldsymbol{\Psi}] [\boldsymbol{\Psi}]^T d\beta \mathbf{D}^T \mathbf{T}_2^T \mathbf{U}^T \\
& - \bar{\omega}^2 \delta \mathbf{U} \mathbf{T}_2 \mathbf{T}_1 \int_0^{\theta_0} [\boldsymbol{\Psi}] [\boldsymbol{\Psi}]^T d\beta \mathbf{T}_1^T \mathbf{T}_2^T \mathbf{U}^T \\
& + \delta \mathbf{U} \mathbf{T}_2 \mathbf{T}_1 \int_0^{\theta_0} [\boldsymbol{\Psi}] \cos(\theta + \beta + \bar{\omega}t) d\beta \ddot{Z}_u \\
& + \delta \mathbf{U} \mathbf{T}_2 \mathbf{T}_1 \int_0^{\theta_0} [\boldsymbol{\Psi}] \sin(\theta + \beta + \bar{\omega}t) d\beta \ddot{X}_u \\
& + \delta Z_u \int_0^{\theta_0} \cos(\theta + \beta + \bar{\omega}t) [\boldsymbol{\Psi}]^T d\beta \mathbf{T}_1^T \mathbf{T}_2^T \dot{\mathbf{U}}^T \\
& \quad + 2\bar{\omega} \delta Z_u \int_0^{\theta_0} \cos(\theta + \beta + \bar{\omega}t) [\boldsymbol{\Psi}]^T d\beta \mathbf{D}^T \mathbf{T}_1^T \mathbf{T}_2^T \dot{\mathbf{U}}^T \\
& \quad + \bar{\omega}^2 \delta Z_u \int_0^{\theta_0} \cos(\theta + \beta + \bar{\omega}t) [\boldsymbol{\Psi}]^T d\beta (\mathbf{D}^T)^2 \mathbf{T}_1^T \mathbf{T}_2^T \mathbf{U}^T \\
& - \delta Z_u \int_0^{\theta_0} \sin(\theta + \beta + \bar{\omega}t) [\boldsymbol{\Psi}]^T d\beta \mathbf{T}_2^T \dot{\mathbf{U}}^T \\
& \quad - 2\bar{\omega} \delta Z_u \int_0^{\theta_0} \sin(\theta + \beta + \bar{\omega}t) [\boldsymbol{\Psi}]^T d\beta \mathbf{D}^T \mathbf{T}_2^T \dot{\mathbf{U}}^T \\
& \quad - \bar{\omega}^2 \delta Z_u \int_0^{\theta_0} \sin(\theta + \beta + \bar{\omega}t) [\boldsymbol{\Psi}]^T d\beta (\mathbf{D}^T)^2 \mathbf{T}_2^T \mathbf{U}^T \\
& - 2\bar{\omega} \delta Z_u \int_0^{\theta_0} \cos(\theta + \beta + \bar{\omega}t) [\boldsymbol{\Psi}]^T d\beta \mathbf{T}_2^T \dot{\mathbf{U}}^T \\
& \quad - 2\bar{\omega}^2 \delta Z_u \int_0^{\theta_0} \cos(\theta + \beta + \bar{\omega}t) [\boldsymbol{\Psi}]^T d\beta \mathbf{D}^T \mathbf{T}_2^T \mathbf{U}^T
\end{aligned} \tag{4.46}$$

$$\begin{aligned}
& -2\bar{\omega}\delta Z_u \int_0^{\theta_0} \sin(\theta + \beta + \bar{\omega}t) [\boldsymbol{\Psi}]^T d\beta \mathbf{T}_1^T \mathbf{T}_2^T \dot{\mathbf{U}}^T \\
& \quad - 2\bar{\omega}^2 \delta Z_u \int_0^{\theta_0} \sin(\theta + \beta + \bar{\omega}t) [\boldsymbol{\Psi}]^T d\beta \mathbf{D}^T \mathbf{T}_1^T \mathbf{T}_2^T \mathbf{U}^T \\
& + \bar{\omega}^2 \delta Z_u \int_0^{\theta_0} \sin(\theta + \beta + \bar{\omega}t) [\boldsymbol{\Psi}]^T d\beta \mathbf{T}_2^T \mathbf{U}^T \\
& - \bar{\omega}^2 \delta Z_u \int_0^{\theta_0} \cos(\theta + \beta + \bar{\omega}t) [\boldsymbol{\Psi}]^T d\beta \mathbf{T}_1^T \mathbf{T}_2^T \mathbf{U}^T \\
& + \delta X_u \int_0^{\theta_0} \sin(\theta + \beta + \bar{\omega}t) [\boldsymbol{\Psi}]^T d\beta \mathbf{T}_1^T \mathbf{T}_2^T \dot{\mathbf{U}}^T \\
& \quad + 2\bar{\omega} \delta X_u \int_0^{\theta_0} \sin(\theta + \beta + \bar{\omega}t) [\boldsymbol{\Psi}]^T d\beta \mathbf{D}^T \mathbf{T}_1^T \mathbf{T}_2^T \dot{\mathbf{U}}^T \\
& \quad + \bar{\omega}^2 \delta X_u \int_0^{\theta_0} \sin(\theta + \beta + \bar{\omega}t) [\boldsymbol{\Psi}]^T d\beta (\mathbf{D}^T)^2 \mathbf{T}_1^T \mathbf{T}_2^T \mathbf{U}^T \\
& + \delta X_u \int_0^{\theta_0} \cos(\theta + \beta + \bar{\omega}t) [\boldsymbol{\Psi}]^T d\beta \mathbf{T}_2^T \dot{\mathbf{U}}^T \\
& \quad + 2\bar{\omega} \delta X_u \int_0^{\theta_0} \cos(\theta + \beta + \bar{\omega}t) [\boldsymbol{\Psi}]^T d\beta \mathbf{D}^T \mathbf{T}_2^T \dot{\mathbf{U}}^T \\
& \quad + \bar{\omega}^2 \delta X_u \int_0^{\theta_0} \cos(\theta + \beta + \bar{\omega}t) [\boldsymbol{\Psi}]^T d\beta (\mathbf{D}^T)^2 \mathbf{T}_2^T \mathbf{U}^T \\
& - 2\bar{\omega} \delta X_u \int_0^{\theta_0} \sin(\theta + \beta + \bar{\omega}t) [\boldsymbol{\Psi}]^T d\beta \mathbf{T}_2^T \dot{\mathbf{U}}^T \\
& \quad - 2\bar{\omega}^2 \delta X_u \int_0^{\theta_0} \sin(\theta + \beta + \bar{\omega}t) [\boldsymbol{\Psi}]^T d\beta \mathbf{D}^T \mathbf{T}_2^T \mathbf{U}^T \\
& + 2\bar{\omega} \delta X_u \int_0^{\theta_0} \cos(\theta + \beta + \bar{\omega}t) [\boldsymbol{\Psi}]^T d\beta \mathbf{T}_1^T \mathbf{T}_2^T \dot{\mathbf{U}}^T \\
& \quad + 2\bar{\omega}^2 \delta X_u \int_0^{\theta_0} \cos(\theta + \beta + \bar{\omega}t) [\boldsymbol{\Psi}]^T d\beta \mathbf{D}^T \mathbf{T}_1^T \mathbf{T}_2^T \mathbf{U}^T \\
& - \bar{\omega}^2 \delta X_u \int_0^{\theta_0} \cos(\theta + \beta + \bar{\omega}t) [\boldsymbol{\Psi}]^T d\beta \mathbf{T}_2^T \mathbf{U}^T \\
& - \bar{\omega}^2 \delta X_u \int_0^{\theta_0} \sin(\theta + \beta + \bar{\omega}t) [\boldsymbol{\Psi}]^T d\beta \mathbf{T}_1^T \mathbf{T}_2^T \mathbf{U}^T \\
& + \delta Z_u \theta_0 \ddot{Z}_u + \delta X_u \theta_0 \ddot{X}_u
\end{aligned}$$

The mass matrix and the stiffness matrix are assembled for N elements. There are $(N+1)$ nodes in the finite element model. In order to satisfy the continuity of the ring, the $(N+1)^{\text{th}}$ node lies on the first node. The contact forces T_x and T_z , which are functions of the displacements and accelerations, are applied as the external forces to the element that is in contact with the ground. These forces are functions of ω . The mass, stiffness, damping, and external forces create an eigenvalue problem where the radial and

tangential displacements and the slopes are eigenvectors. The natural frequencies are the eigenvalues.

Table 4.3 presents the first twenty natural frequencies of the hybrid model when the vehicle is stationary, i.e. $\bar{\omega}=0$. Increasing the number of elements reveals a greater number of frequencies. Also this table tabulates the relative error between the natural frequencies obtained by using $N=60$, $N=72$, and $N=144$ elements along the ring. The maximum error between the results from $N=60$ and from $N=144$ is about 2.8% showing a satisfactory convergence in the finite element model. The accuracy gained by doubling the number of the elements from 72 to 144 does not compensate for the time spent.

Table 4.4 presents the natural frequencies of the hybrid quarter-car model with a rotating tire when $\bar{\omega}=100$. This angular velocity corresponds to the forward speed of 115 km/h. However, the convergence is evident. Since the influence of rotation will be discussed in the next chapter, only the variation of the natural frequencies with different numbers of elements is shown as well as the relative error. The results for $N=144$ are taken as reference to calculate the relative error. The relative error, calculated between the results gained by using $N=60$ and $N=144$ shows a maximum improvement of 5.5%. However this error reduces to 2.8% if $N=72$ elements are used.

Table 4.3: The natural frequencies of the hybrid quarter-car model with a non-rotating ring ($\bar{\omega}=0$) obtained by FEA

N=18	N=36	N=60		N=72		N=144
<i>ω(rad/s)</i>	<i>ω(rad/s)</i>	<i>ω (rad/s)</i>	relative error %	<i>ω(rad/s)</i>	relative error %	<i>ω(rad/s)</i>
9.496	9.489	9.489	0.0053	9.4886	0.0011	9.4885
287.670	283.046	280.711	0.7730	280.2655	0.6131	278.5577
397.544	390.063	388.385	0.1768	388.1638	0.1197	387.6997
609.466	592.687	587.556	-0.4424	587.2234	-0.4987	590.1668
709.856	681.175	674.717	0.2645	673.9935	0.1570	672.9370
943.220	892.582	878.743	0.5672	877.1284	0.3824	873.7872
1070.434	1000.557	984.657	0.4297	982.9822	0.2588	980.4445
1320.987	1206.893	1178.710	0.2407	1176.0714	0.0163	1175.8800
1445.722	1291.998	1255.710	0.7834	1251.7973	0.4694	1245.9489
1731.861	1522.362	1473.494	0.5489	1469.2357	0.2584	1465.4496
1900.481	1635.521	1564.396	1.8782	1555.4809	1.2976	1535.5551
2228.650	1761.295	1669.505	1.5478	1660.3096	0.9885	1644.0581
2385.411	1899.409	1800.103	1.0674	1790.0587	0.5035	1781.0916
2590.987	2051.672	1953.007	0.9917	1943.9218	0.5219	1933.8293
2978.033	2230.574	2092.292	1.4196	2079.3519	0.7924	2063.0046
3014.081	2361.155	2207.593	1.5129	2192.6317	0.8250	2174.6911
3477.653	2488.322	2321.271	1.3643	2305.9802	0.6966	2290.0282
3690.971	2735.396	2513.676	1.5859	2492.7444	0.7400	2474.4347
4068.384	2849.169	2622.601	1.7575	2600.9741	0.9183	2577.3061
4388.903	3199.793	2880.545	2.8295	2847.1965	1.6390	2801.2840

Table 4.4: The natural frequencies of the hybrid quarter-car model with a rotating ring ($\bar{\omega}=100 \text{ rad/s}$) obtained by FEA

N=18	N=36	N=60		N=72		N=144
$\omega \text{ (rad/s)}$	$\omega \text{ (rad/s)}$	$\omega \text{ (rad/s)}$	<i>relative error %</i>	$\omega \text{ (rad/s)}$	<i>relative error %</i>	$\omega \text{ (rad/s)}$
9.4871	9.4869	9.4869	0.0000	9.4869	0.0000	9.4869
288.6579	282.9018	280.1268	0.6300	279.6865	0.4718	278.3731
407.9175	392.2881	386.8513	0.3083	386.1597	0.1290	385.6622
569.353	549.5164	544.124	-0.2202	543.8248	-0.2751	545.3250
747.6596	679.6672	659.2539	0.7708	656.9629	0.4206	654.2115
906.1717	850.2398	827.4082	0.2935	824.9562	-0.0037	824.9869
1106.6979	956.3364	917.3778	0.9227	913.5292	0.4994	908.9901
1338.1405	1175.1526	1108.6844	1.2915	1102.0692	0.6872	1094.5480
1525.9204	1305.1307	1238.4693	1.5554	1230.0898	0.8683	1219.5011
1833.8494	1497.4557	1391.4747	1.0590	1382.7982	0.4289	1376.8929
1999.5993	1633.2825	1516.4997	2.6106	1501.7285	1.6112	1477.9168
2340.1814	1812.8222	1639.2701	2.4430	1622.6213	1.4026	1600.1772
2582.5449	1909.0480	1762.4836	2.1736	1744.325	1.1210	1724.9887
2867.2631	2133.5335	1915.6631	2.1564	1895.5956	1.0863	1875.2256
3123.1556	2272.0614	2063.5632	2.7177	2039.4547	1.5176	2008.9665
3252.9017	2435.1601	2187.7658	2.8131	2158.6905	1.4467	2127.9051
3810.3735	2650.9184	2312.3594	2.1755	2288.3644	1.1152	2263.1249
4009.491	2779.1708	2496.6086	4.1152	2447.3679	2.0617	2397.9294
4430.9489	3130.7555	2634.2192	2.3504	2605.7666	1.2449	2573.7258
4723.0362	3261.8872	2859.793	5.4715	2787.1358	2.7919	2711.4355

4.4. CONCLUDING REMARKS

In this chapter, the equations of the motion of the model, which was introduced earlier, was solved by using two approximate methods. The first method was the Galerkin method. The trigonometric functions, which are the modes of the center-fixed ring as shown in Chapter 2, were used as admissible functions. The natural frequencies were obtained, and the convergence was studied. Although the model is a complicated model, it was shown that even using the first five harmonics of the ring produces excellent results.

In the second part of this chapter, the finite element solution of the model was analyzed. It can be seen that the results of FEA are similar to those obtained using the Galerkin method. The convergence is also investigated. These two approximate methods can be used when dealing with a three-dimensional model. For instance the Galerkin method can be used to solve the equations of motion when the tire is modeled as a rotating shell. Also the finite element method is applicable to problems with more complicated geometries. The finite element method can take into account the sidewall of the tire as well as the thread pattern.

In the next chapter, the equations of motion of the hybrid model are solved analytically. A closed-form solution is presented for the rotating ring in contact with the road. The natural frequencies are obtained and the mode shapes are presented. The comparison of both the rotating and non-rotating rings is performed.

CHAPTER 5 ANALYTICAL SOLUTION OF THE HYBRID MODEL

5.1. INTRODUCTION

An analytical solution of the hybrid quarter-car model is presented in this chapter. The rotating ring model is considered, and the boundary conditions and the external forces are applied. The contact point between the rotating tire and the road is treated as the boundary condition of the rotating ring, where the radial displacement and the tangential displacement of the tire create the vertical and horizontal displacement of the center of the tire, respectively. The forces and the moments at the contact point, which are functions of the dynamic response of the system, are employed in the eigen-value problem. A new method is introduced to investigate the effects of the displacements and the accelerations of the center of the ring, as well as the effects of the rotating tire dynamics, on the dynamic response of a vehicle system. The analytical solution enables

us to find the exact natural frequencies and the mode shapes of the hybrid model. It also provides the exact expressions for the horizontal and vertical components of the contact force that is used in the calculation of the response to the road excitation.

5.2. METHODOLOGY OF ANALYTICAL SOLUTION

Figure 5.1 shows the hybrid model of a vehicle. The forces and the moments at the contact point are shown in detail. The contact point is located at $\varphi=\pi$. In order to solve the equations of motion analytically, the vertical and horizontal components of the contact force are removed from the equations of motion and considered as boundary conditions. After neglecting the effects of gravity and of static deflection, the equations of motion are rewritten as:

$$\begin{aligned} \frac{EI}{a^4} \left(\frac{\partial^4 U}{\partial \varphi^4} - \frac{\partial^3 V}{\partial \varphi^3} \right) + \frac{EA}{a^2} \left(\frac{\partial V}{\partial \varphi} + U \right) - \frac{N_0}{a^2} \frac{\partial^2 U}{\partial \varphi^2} \\ + \rho A \left(\frac{D^2 U}{Dt^2} - 2\bar{\omega} \frac{DV}{Dt} - \bar{\omega}^2 U + \ddot{Z}_u \cos \varphi + \ddot{X}_u \sin \varphi \right) = 0 \end{aligned} \quad (5.1)$$

$$\begin{aligned} \frac{EI}{a^4} \left(\frac{\partial^3 U}{\partial \varphi^3} - \frac{\partial^2 V}{\partial \varphi^2} \right) - \frac{EA}{a^2} \left(\frac{\partial^2 V}{\partial \varphi^2} + \frac{\partial U}{\partial \varphi} \right) \\ + \rho A \left(\frac{D^2 V}{Dt^2} + 2\bar{\omega} \frac{DU}{Dt} - \bar{\omega}^2 V - \ddot{Z}_u \sin \varphi + \ddot{X}_u \cos \varphi \right) = 0 \end{aligned} \quad (5.2)$$

$$T_z = m_w \ddot{Z}_u + m_t \ddot{Z}_u + k(Z_u - Z_s) + a\rho A \int_{-\pi}^{\pi} \left(\frac{\partial^2 U}{\partial t^2} \cos \varphi - \frac{\partial^2 V}{\partial t^2} \sin \varphi \right) d\varphi \quad (5.3)$$

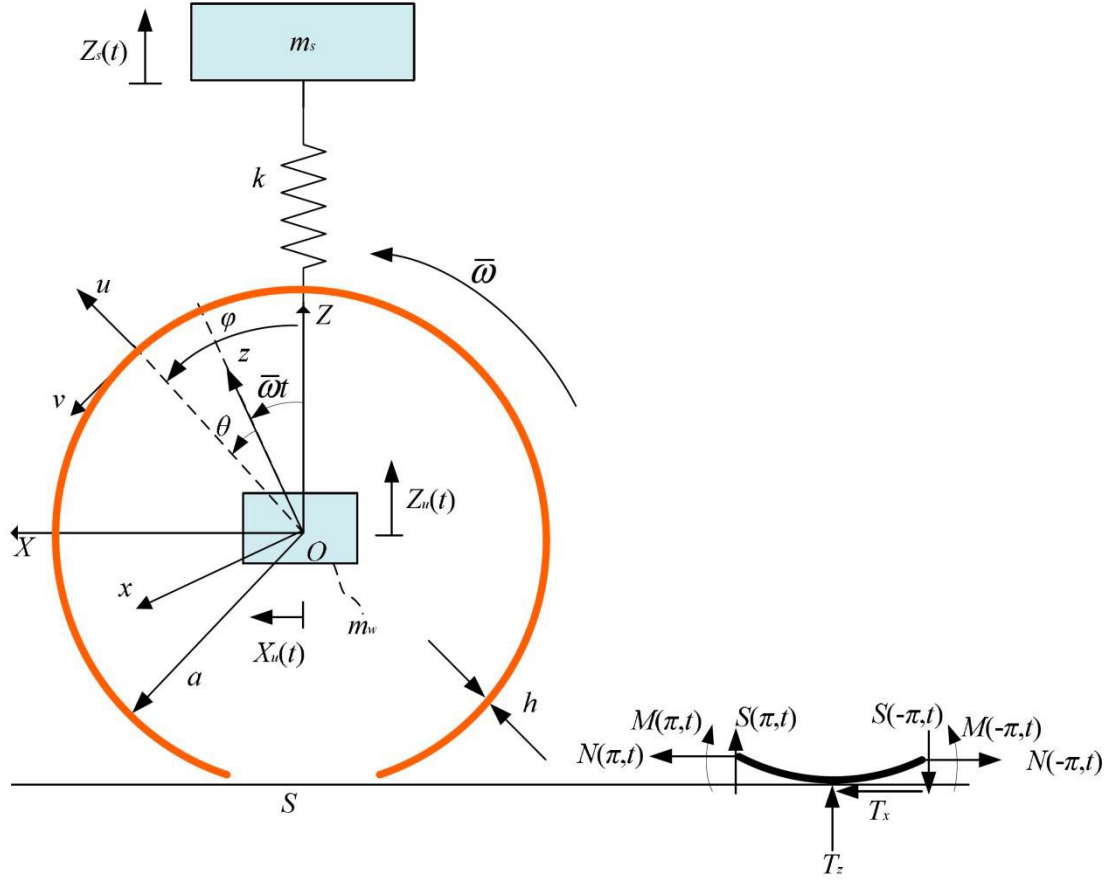


Figure 5.1: The schematic of a 2-D model of a vehicle: Forces and moments at the contact area

$$T_x = m_w \ddot{X}_u + m_t \ddot{X}_u + a \rho A \int_{-\pi}^{\pi} \left(\frac{\partial^2 U}{\partial t^2} \sin \varphi + \frac{\partial^2 V}{\partial t^2} \cos \varphi \right) d\varphi \quad (5.4)$$

$$m_s \ddot{Z}_s + k(Z_s - Z_u) = 0 \quad (5.5)$$

The angular coordinate of the ring is considered in the interval of $(-\pi, \pi)$, enabling us to use symmetry in the solutions. Accordingly, in Equations (5.3) and (5.4) the limits of

integration are changed to $(-\pi, \pi)$. The ring is considered an open ring with a cut at the contact point. The boundary conditions are defined as:

$$N(-\pi, t) - N(\pi, t) = T_x \quad (5.6)$$

$$S(-\pi, t) - S(\pi, t) = T_z \quad (5.7)$$

$$M(-\pi, t) = M(\pi, t) \quad (5.8)$$

$$U(-\pi, t) = U(\pi, t) \quad (5.9)$$

$$V(-\pi, t) = V(\pi, t) \quad (5.10)$$

$$U'(-\pi, t) = U'(\pi, t) \quad (5.11)$$

As can be seen, the equations above satisfy the continuity of the radial and tangential displacements, the slope, and the bending moment at the contact point as well as the discontinuity in both axial and shear forces. The axial force, bending moment, and shear force at the cross section of the ring are defined as:

$$N = \frac{EA}{a} \left(\frac{\partial V}{\partial \varphi} + U \right) \quad (5.12)$$

$$M = \frac{EI}{a^2} \left(\frac{\partial V}{\partial \varphi} - \frac{\partial^2 U}{\partial \varphi^2} \right) \quad (5.13)$$

$$S = \frac{EI}{a^3} \left(\frac{\partial^2 V}{\partial \varphi^2} - \frac{\partial^3 U}{\partial \varphi^3} \right) \quad (5.14)$$

The separation of variables is used to solve Equations (5.1)–(5.5). By assuming a harmonic solution with a frequency of ω for the time part of the solutions, one can write the following equations:

$$\frac{EI}{a^4} \left(\frac{\partial^4 U}{\partial \phi^4} - \frac{\partial^3 V}{\partial \phi^3} \right) + \frac{EA}{a^2} \left(\frac{\partial V}{\partial \phi} + U \right) - \frac{N_0}{a^2} \frac{\partial^2 U}{\partial \phi^2} + \rho A \left(-\omega^2 U + 2\bar{\omega} \omega j U' + \bar{\omega}^2 U'' - 2\bar{\omega} \omega j V - 2\bar{\omega}^2 V' - \bar{\omega}^2 U \right) = \rho A \omega^2 (Z_u \cos \phi + X_u \sin \phi) \quad (5.15)$$

$$\frac{EI}{a^4} \left(\frac{\partial^3 U}{\partial \phi^3} - \frac{\partial^2 V}{\partial \phi^2} \right) - \frac{EA}{a^2} \left(\frac{\partial^2 V}{\partial \phi^2} + \frac{\partial U}{\partial \phi} \right) + \rho A \left(-\omega^2 V + 2\bar{\omega} \omega j V' + \bar{\omega}^2 V'' + 2\bar{\omega} \omega j U + 2\bar{\omega}^2 U' - \bar{\omega}^2 V \right) = \rho A \omega^2 (-Z_u \sin \phi + X_u \cos \phi) \quad (5.16)$$

$$T_z = -m_w \omega^2 Z_u - m_t \omega^2 Z_u + k(Z_u - Z_s) - \omega^2 a \rho A \int_{-\pi}^{\pi} (U \cos \phi - V \sin \phi) d\phi \quad (5.17)$$

$$T_x = -m_w \omega^2 X_u - m_t \omega^2 X_u - \omega^2 a \rho A \int_{-\pi}^{\pi} (U \sin \phi + V \cos \phi) d\phi \quad (5.18)$$

$$-m_s \omega^2 Z_s + k(Z_s - Z_u) = 0 \quad (5.19)$$

The equations above are non-homogenous ordinary differential equations. The solutions of U and V are assumed as:

$$U(\phi) = U_h(\phi) + U_p(\phi) \quad (5.20)$$

$$V(\phi) = V_h(\phi) + V_p(\phi) \quad (5.21)$$

where the index h and p refer to the homogenous solutions and the particular solutions, respectively. The homogenous solution of a system of ordinary differential equations with constant coefficients is assumed as:

$$U_h(\varphi) = \alpha e^{\lambda\varphi} \quad (5.22)$$

$$V_h(\varphi) = \beta e^{\lambda\varphi} \quad (5.23)$$

In order to find the homogenous solutions, the right hand sides of Equations (5.15) and (5.16) are considered zero, and, then, Equations (5.22) and (5.23) are substituted for U and V , respectively. The results are expressed in the following format:

$$\begin{bmatrix} \frac{EI}{a^4} \lambda^4 - \frac{N_0}{a^2} \lambda^2 + \frac{EA}{a^2} - \rho A \left((\omega - j\bar{\omega}\lambda)^2 + \bar{\omega}^2 \right) & - \left(\frac{EI}{a^4} \lambda^3 - \frac{EA}{a^2} \lambda + 2\rho A \bar{\omega} (j\omega + \bar{\omega}\lambda) \right) \\ \left(\frac{EI}{a^4} \lambda^3 - \frac{EA}{a^2} \lambda + 2\rho A \bar{\omega} (j\omega + \bar{\omega}\lambda) \right) & - \frac{EI}{a^4} \lambda^2 - \frac{EA}{a^2} \lambda^2 - \rho A \left((\omega - j\bar{\omega}\lambda)^2 + \bar{\omega}^2 \right) \end{bmatrix} \begin{bmatrix} \alpha \\ \beta \end{bmatrix} = \begin{bmatrix} 0 \\ 0 \end{bmatrix} \quad (5.24)$$

The equation above is solved for λ which is a function of ω . The determinant is a 6th order equation. Therefore, the homogenous solutions of U and V are written as:

$$U_h(\varphi) = \sum_{j=1}^6 \alpha_j e^{\lambda_j \varphi} \quad (5.25)$$

$$V_h(\varphi) = \sum_{j=1}^6 \beta_j e^{\lambda_j \varphi} \quad (5.26)$$

In the equations above, α_j s are six constants, which are to be determined by using the boundary conditions at the contact point. β_j s are obtained as functions of α_j s and ω according to Equation (5.24).

In order to find the particular solution of Equations (5.15)–(5.16), the following identities are used:

$$\cos \varphi = \frac{e^{j\varphi} + e^{-j\varphi}}{2} \quad \sin \varphi = \frac{e^{j\varphi} - e^{-j\varphi}}{2j} \quad (5.27)$$

and Equations (5.15)–(5.16) are rewritten as:

$$\begin{aligned} \frac{EI}{a^4} \left(\frac{\partial^4 U}{\partial \varphi^4} - \frac{\partial^3 V}{\partial \varphi^3} \right) + \frac{EA}{a^2} \left(\frac{\partial V}{\partial \varphi} + U \right) - \frac{N_0}{a^2} \frac{\partial^2 U}{\partial \varphi^2} + \\ \rho A \left(-\omega^2 U + 2\bar{\omega} \omega j U' + \bar{\omega}^2 U'' - 2\bar{\omega} \omega j V - 2\bar{\omega}^2 V' - \bar{\omega}^2 U \right) = \frac{\rho A \omega^2}{2} (Z_u - jX_u) e^{j\varphi} \\ + \frac{\rho A \omega^2}{2} (Z_u + jX_u) e^{-j\varphi} \end{aligned} \quad (5.28)$$

$$\begin{aligned} \frac{EI}{a^4} \left(\frac{\partial^3 U}{\partial \varphi^3} - \frac{\partial^2 V}{\partial \varphi^2} \right) - \frac{EA}{a^2} \left(\frac{\partial^2 V}{\partial \varphi^2} + \frac{\partial U}{\partial \varphi} \right) + \\ \rho A \left(-\omega^2 V + 2\bar{\omega} \omega j V' + \bar{\omega}^2 V'' + 2\bar{\omega} \omega j U + 2\bar{\omega}^2 U' - \bar{\omega}^2 V \right) = \frac{\rho A \omega^2}{2} (Z_u - jX_u) j e^{j\varphi} \\ - \frac{\rho A \omega^2}{2} (Z_u + jX_u) j e^{-j\varphi} \end{aligned} \quad (5.29)$$

At this step, X_u and Z_u are treated as temporarily unknown constants that are multiplied by the exponential function. First, the responses of the equations above to $e^{j\varphi}$ are obtained:

$$\begin{aligned} \frac{EI}{a^4} \left(\frac{\partial^4 U}{\partial \varphi^4} - \frac{\partial^3 V}{\partial \varphi^3} \right) + \frac{EA}{a^2} \left(\frac{\partial V}{\partial \varphi} + U \right) - \frac{N_0}{a^2} \frac{\partial^2 U}{\partial \varphi^2} + \\ \rho A \left(-\omega^2 U + 2\bar{\omega} \omega j U' + \bar{\omega}^2 U'' - 2\bar{\omega} \omega j V - 2\bar{\omega}^2 V' - \bar{\omega}^2 U \right) = \frac{\rho A \omega^2}{2} e^{j\varphi} \end{aligned} \quad (5.30)$$

$$\begin{aligned} \frac{EI}{a^4} \left(\frac{\partial^3 U}{\partial \varphi^3} - \frac{\partial^2 V}{\partial \varphi^2} \right) - \frac{EA}{a^2} \left(\frac{\partial^2 V}{\partial \varphi^2} + \frac{\partial U}{\partial \varphi} \right) + \\ \rho A \left(-\omega^2 V + 2\bar{\omega} \omega j V' + \bar{\omega}^2 V'' + 2\bar{\omega} \omega j U + 2\bar{\omega}^2 U' - \bar{\omega}^2 V \right) = \frac{\rho A \omega^2}{2} j e^{j\varphi} \end{aligned} \quad (5.31)$$

The solution is assumed in the form of

$$U(\varphi) = \alpha_p e^{j\varphi} \quad V(\varphi) = \beta_p e^{j\varphi} \quad (5.32)$$

in which α_p and β_p are obtained from the following equation:

$$\begin{bmatrix} \frac{EI}{a^4} + \frac{N_0}{a^2} + \frac{EA}{a^2} - \rho A((\omega + \bar{\omega})^2 + \bar{\omega}^2) & j\left(\frac{EI}{a^4} + \frac{EA}{a^2} - 2\rho A\bar{\omega}(\omega + \bar{\omega})\right) \\ -j\left(\frac{EI}{a^4} + \frac{EA}{a^2} - 2\rho A\bar{\omega}(\omega + \bar{\omega})\right) & \frac{EI}{a^4} + \frac{EA}{a^2} - \rho A((\omega + \bar{\omega})^2 + \bar{\omega}^2) \end{bmatrix} \begin{bmatrix} \alpha_p \\ \beta_p \end{bmatrix} = \frac{\rho A \omega^2}{2} \begin{bmatrix} 1 \\ j \end{bmatrix} \quad (5.33)$$

Finally, the particular solutions of Equations (5.28)–(5.29) are written as:

$$U_p(\varphi) = (Z_u - jX_u)\alpha_p e^{j\varphi} + (Z_u + jX_u)\bar{\alpha}_p e^{-j\varphi} \quad (5.34)$$

$$V_p(\varphi) = (Z_u - jX_u)\beta_p e^{j\varphi} + (Z_u + jX_u)\bar{\beta}_p e^{-j\varphi} \quad (5.35)$$

in which $\bar{\alpha}_p$ and $\bar{\beta}_p$ are the conjugates of α_p and β_p , respectively. By substituting the coordinate of the contact point in equations (5.20) and (5.21) as:

$$U(\pi) = U_h(\pi) + U_p(\pi) \quad (5.36)$$

$$V(\pi) = V_h(\pi) + V_p(\pi) \quad (5.37)$$

and using the fact that the displacements of the center of the tire are related to the radial and tangential displacements of the contact point, i.e.

$$X_u = V(\pi) \quad (5.38)$$

$$Z_u = U(\pi) \quad (5.39)$$

the following equations are written:

$$Z_u = U_h(\pi) + (Z_u - jX_u)\alpha_p e^{j\pi} + (Z_u + jX_u)\bar{\alpha}_p e^{-j\pi} \quad (5.40)$$

$$X_u = V_h(\pi) + (Z_u - jX_u)\beta_p e^{j\pi} + (Z_u + jX_u)\bar{\beta}_p e^{-j\pi} \quad (5.41)$$

The equations above are rewritten in the matrix form as shown below. Solving these equations, one can obtain X_u and Z_u in terms of α_j s and ω .

$$\begin{bmatrix} 1 + \alpha_p + \bar{\alpha}_p & -j\alpha_p + j\bar{\alpha}_p \\ \beta_p + \bar{\beta}_p & 1 - j\beta_p + j\bar{\beta}_p \end{bmatrix} \begin{Bmatrix} Z_u \\ X_u \end{Bmatrix} = \begin{Bmatrix} U_h(\pi) \\ V_h(\pi) \end{Bmatrix} \quad (5.42)$$

Finally, U , V , X_u , and Z_u are substituted in Equations (5.6)–(5.11) resulting in an eigen-value problem. The eigen-values are the natural frequencies. Also the eigen-vectors demonstrate the six α_j s that determine the mode shapes.

5.3. FREE VIBRATION RESPONSE

Table 5.1 tabulates the natural frequencies of the hybrid quarter-car model for different angular velocities of the tire and Figure 5.2 demonstrates the variation of the frequencies at different angular velocities. The comparison is done for the angular velocity in the range of $\bar{\omega}=0$ to $\bar{\omega}=120 \text{ rad/s}$. The conversion of each angular velocity to the corresponding forward speed of the vehicle is shown in Table 5.2.

Table 5.1: The natural frequencies of the hybrid quarter-car model at different angular velocities

	$\bar{\omega}=0$	$\bar{\omega}=20$	$\bar{\omega}=40$	$\bar{\omega}=60$	$\bar{\omega}=80$	$\bar{\omega}=100$	$\bar{\omega}=120$
ω_1	8.380	8.383	8.396	8.414	8.439	8.471	8.505
ω_2	52.704	52.788	53.041	53.455	54.021	54.726	55.556
ω_3	140.054	139.817	139.110	137.958	136.406	134.527	132.426
ω_4	282.201	282.247	282.398	282.683	283.178	283.939	285.022
ω_5	424.466	424.236	423.503	422.128	419.932	416.789	412.689
ω_6	582.362	579.636	572.432	562.739	552.296	542.085	532.375
ω_7	716.056	716.978	717.473	712.690	700.179	682.278	662.632
ω_8	875.084	867.741	852.951	840.772	832.957	822.770	804.420
ω_9	1003.374	1008.419	1010.539	993.939	968.110	946.861	932.526
ω_{10}	1167.301	1153.913	1137.199	1135.350	1126.000	1096.160	1062.735
ω_{11}	1293.591	1304.467	1301.896	1272.402	1254.024	1247.173	1220.209

Table 5.2 The conversion of the angular velocity of the tire to the forward speed of the vehicle

$\bar{\omega}$ angular velocity of tire (rad/s)	0	20	40	60	80	100	120
forward speed of vehicle (m/s)	0	6.4	12.8	19.2	25.6	32	38.4
forward speed of vehicle (km/h)	0	23.04	46.08	69.12	92.16	115.2	138.24

As discussed in Chapter 2, the analytical solutions for the free vibration of a circular ring show that each natural frequency of a non-rotating ring splits into two natural frequencies for the rotating ring because of the effects of the rotation. Also it was shown that the breathing mode is an exception ($n=0$). The tire, in contact with the road, is no longer a center-fixed circular ring, free at the circumference. Consequently, the bifurcating natural frequencies, which increase and decrease with the multiple of the angular velocity of the ring, do not occur [72, 75]. “Occasionally a gyroscopic split can be detected, when the

contact state does not disturb the eigenmode” [72]. The effect of the rotation on the lower natural frequencies is not significant, such that the difference between the frequency at $\bar{\omega}=0$ and the one at $\bar{\omega}=100 \text{ rad/s}$ is about 1%. The first and the second frequencies of the hybrid system are very close to those of a two degree-of-freedom quarter-car model. However, the higher frequencies mostly decrease by increasing the angular velocity of the ring.

The natural frequencies obtained by using the three different methods of the Galerkin, the FEA, and the exact solution, are compared in Figure 5.3. The results of the analytical solution are taken as the reference. The frequencies obtained by using the Galerkin method and the finite element Method are normalized with respect to those from the analytical method. The comparison has been done for two different cases:

- (a) a hybrid quarter-car model with a non-rotating ring ($\bar{\omega}=0$)
- (b) a hybrid quarter-car model with a rotating ring $\bar{\omega}=100 \text{ rad/s}$

Since the finite element method did not provide reliable answers for the second and the third natural frequencies of the model, these results are not included in the comparison. It can be seen that the results by using the different methods are more or less similar. Both cases show a maximum deviation of about 13 %, which occurs at the first frequency.

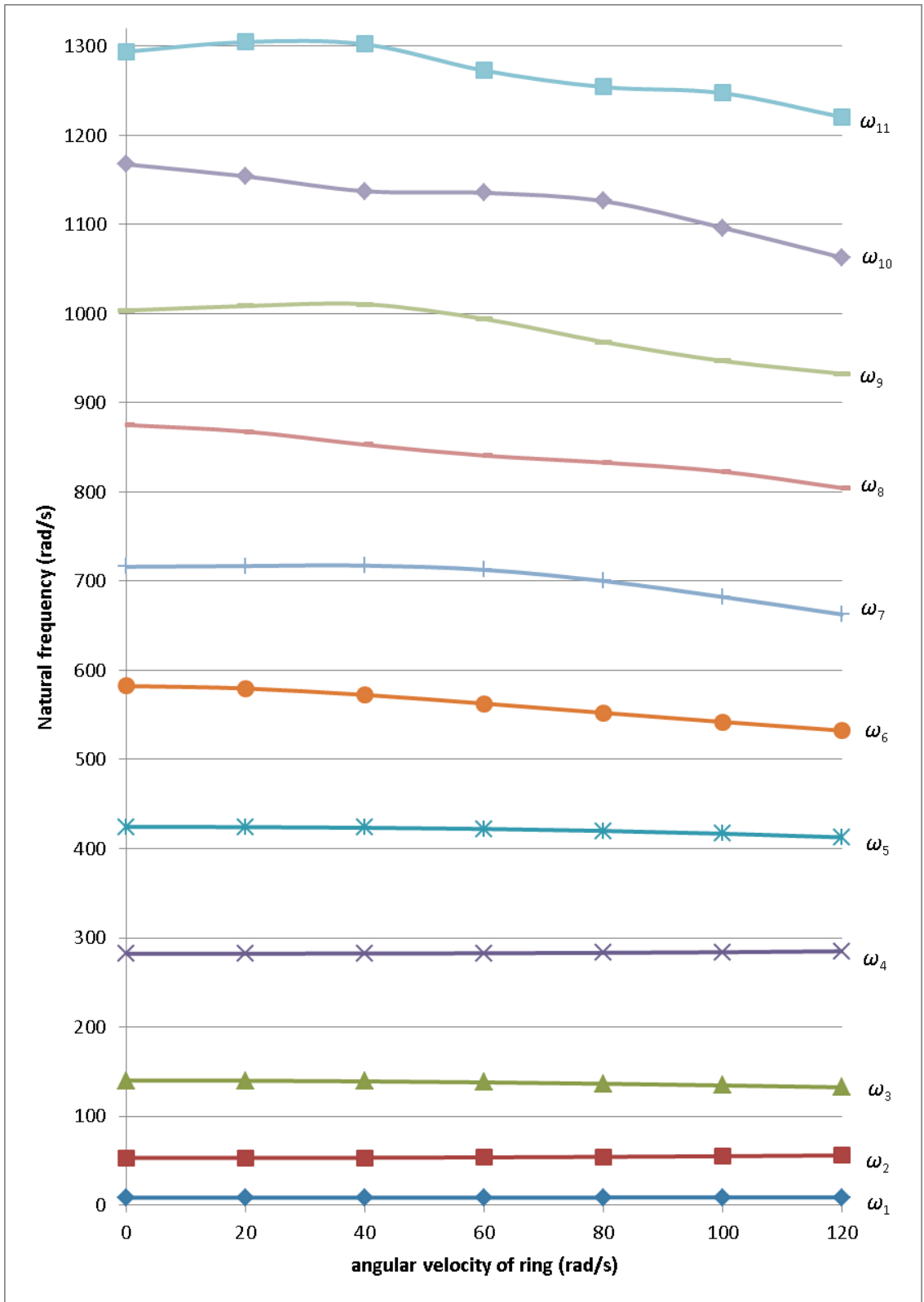


Figure 5.2: The natural frequencies of the hybrid quarter-car model for different angular velocities of the ring

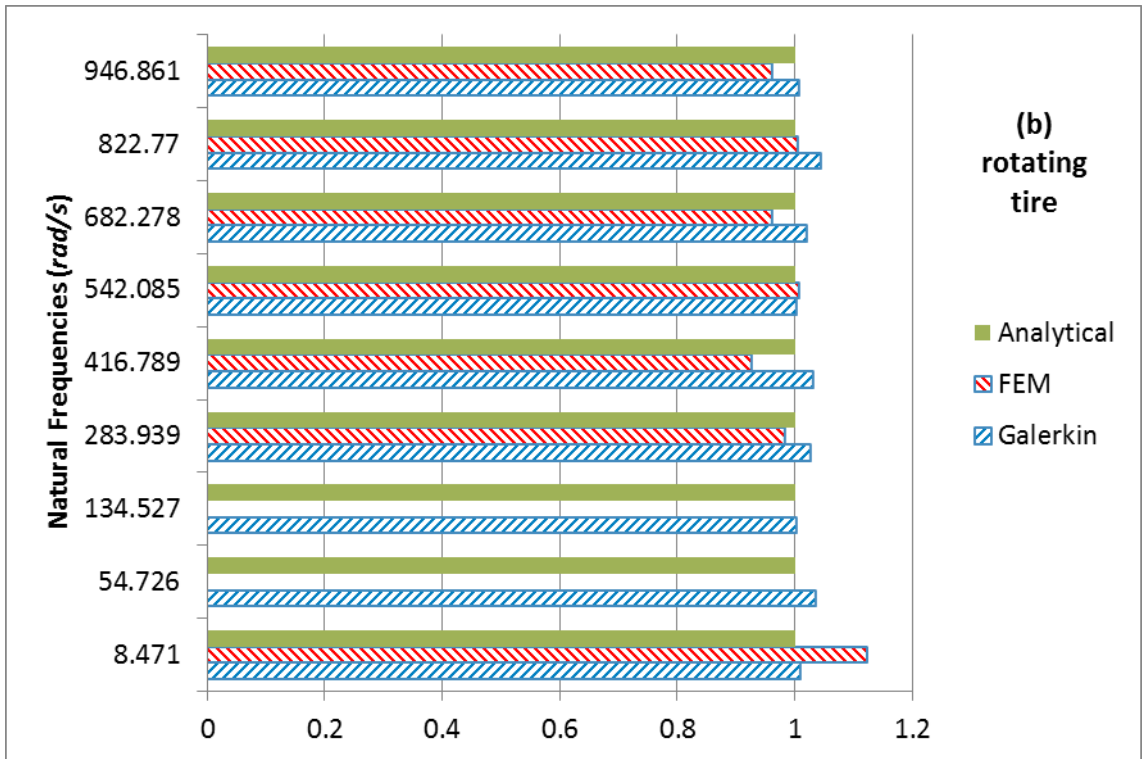
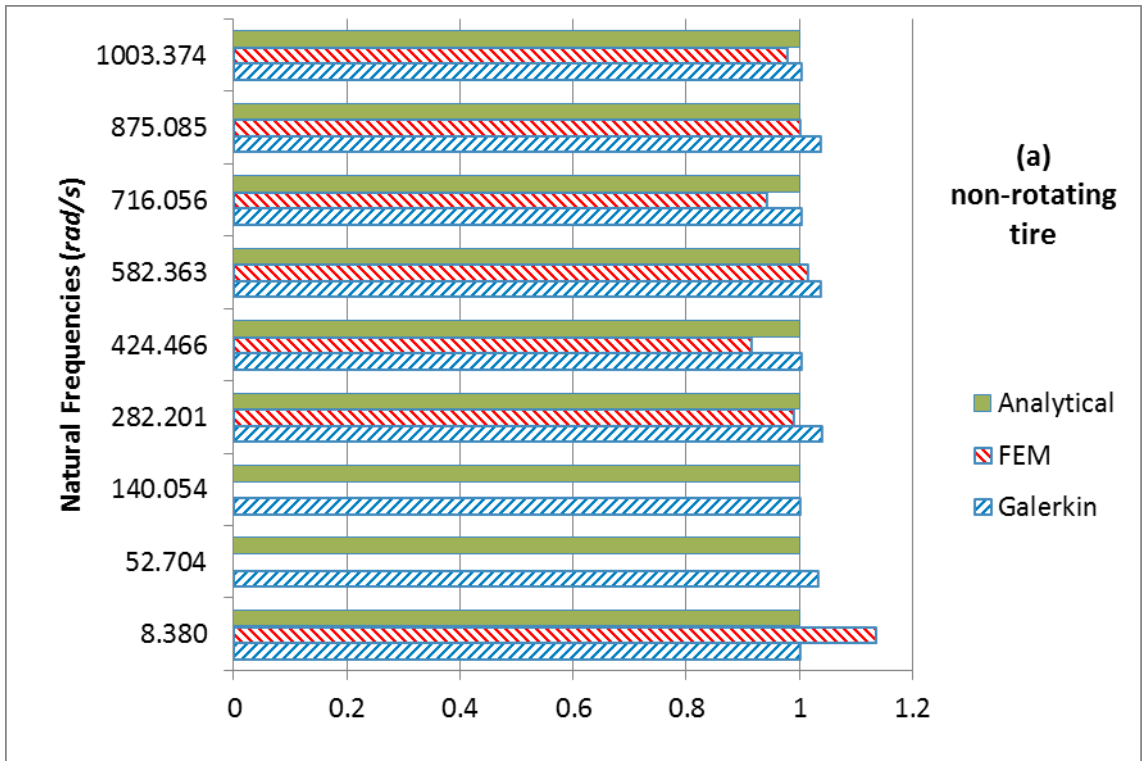


Figure 5.3: Comparison of the natural frequencies obtained by using different methods (a) non rotating ring (b) rotating ring $\bar{\omega}=100 \text{ rad/s}$

Figures 5.4 to 5.7 demonstrate the first four modes of the model with a non-rotating ring. The radial and the tangential displacements are shown for each mode as well as the vertical and the horizontal displacements of the center of the tire and the vertical displacement of the vehicle body. The radial displacement of the ring is shown in a polar coordinate system. The un-deformed tire is also shown as a dashed circle. The displacements in each mode are relative, so that they can be multiplied by an arbitrary number. In order to make the comparison easier, the maximum radial displacement of the ring is considered as one, and the rest of the displacements are normalized accordingly.

For the first mode, the sprung mass displacement is more dominant, whereas the radial and the tangential displacements are moderate. At this mode, the displacement of the sprung mass is 4.55 times larger than the displacement of the center of the wheel (unsprung mass). These displacements are in phase. The tangential displacement at the tire-road contact is zero. Therefore, the horizontal displacement of the center of the tire is zero, too.

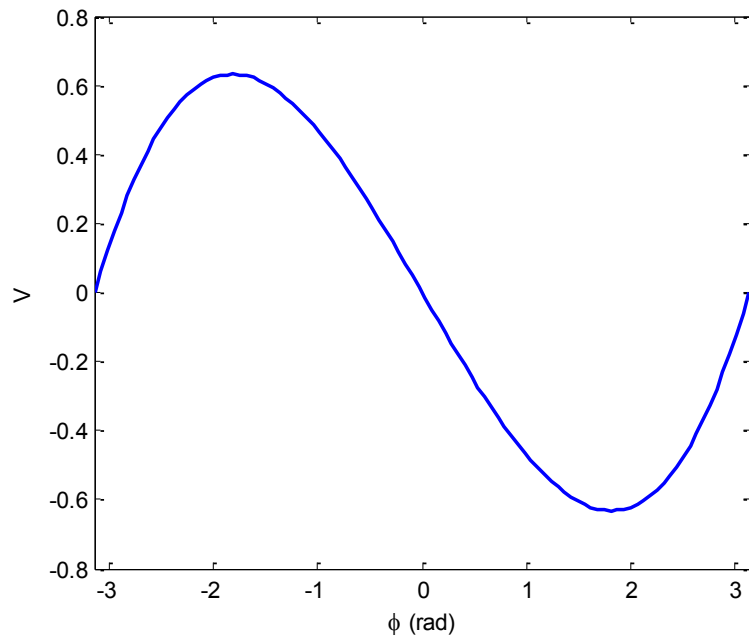
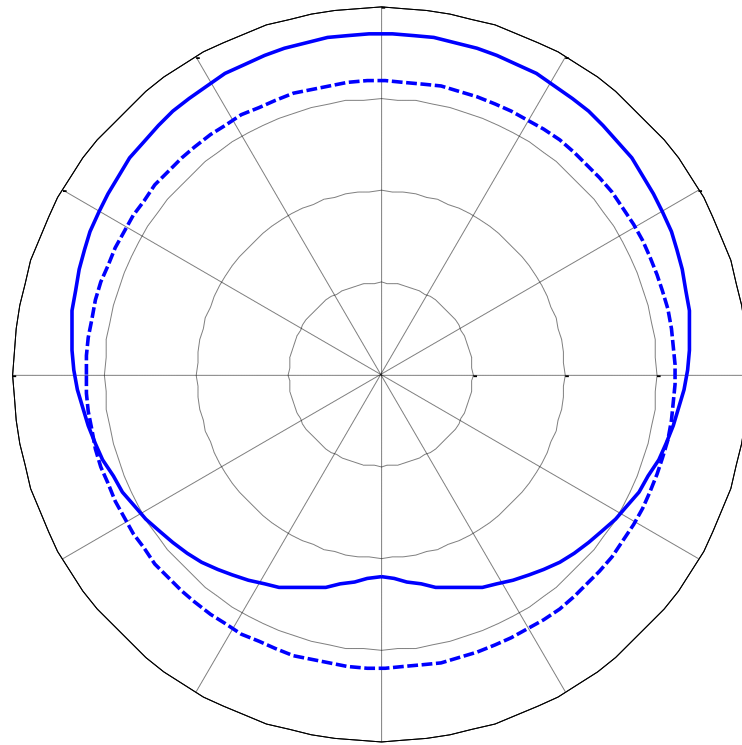


Figure 5.4: The first mode of the hybrid quarter-car model with a non-rotating tire. The radial displacement of tire U (top) and the tangential displacement of tire V (below). $\omega= 8.3803 \text{ rad/s}$, $Z_s= -4.552$, $Z_u=-1$, $X_u=0$

As shown in Figure 5.5, the radial displacement and consequently the vertical displacement of the unsprung mass are the most dominant displacements for $\omega=52.7044$ rad/s. The sprung mass moves with a small amplitude in the opposite direction of the unsprung mass. The maximum tangential displacement is about half of the maximum radial displacement, occurring at $\varphi = \pm \pi/2$. The tangential displacement at the contact area and X_u are both zero.

The third mode shows a large amplitude of vibration for V and X_u . The maximum tangential displacement is twice as large as the maximum radial displacement of the ring. However, the maximum U occurs at $\varphi = -\pi/2$, and the maximum V occurs at $\varphi = 0$. The fourth vibration mode of the system is shown in Figure 5.7. At this mode, the vertical displacement of the unsprung mass is almost 1000 times larger than the sprung mass displacement. The maximum radial displacement occurs at the top of the ring, and the radial displacement at the contact point is 0.0313 times of that displacement.

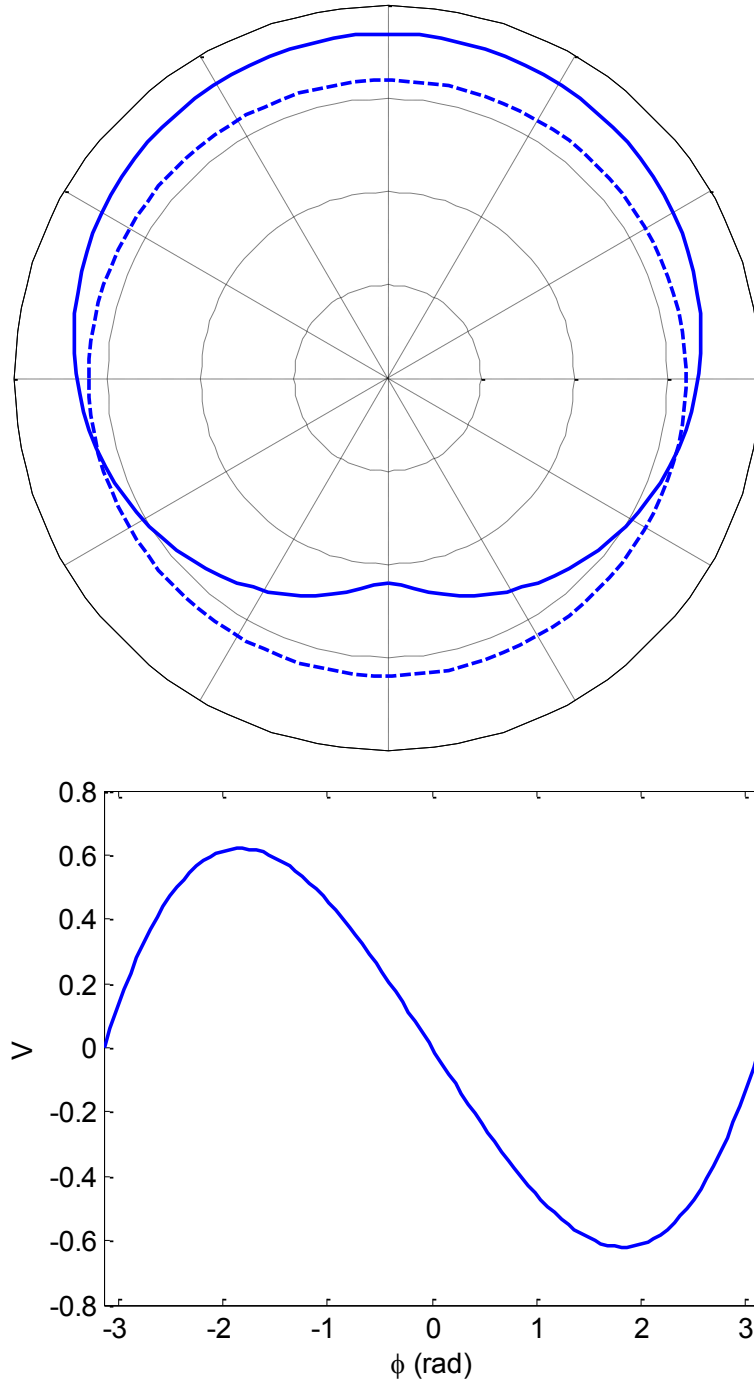


Figure 5.5: The second mode of the hybrid quarter-car model with a non-rotating tire. The radial displacement of the tire U (top) and the tangential displacement of tire V (below). $\omega=52.7044 \text{ rad/s}$, $Z_s=0.0335, Z_u=-1, X_u=0$

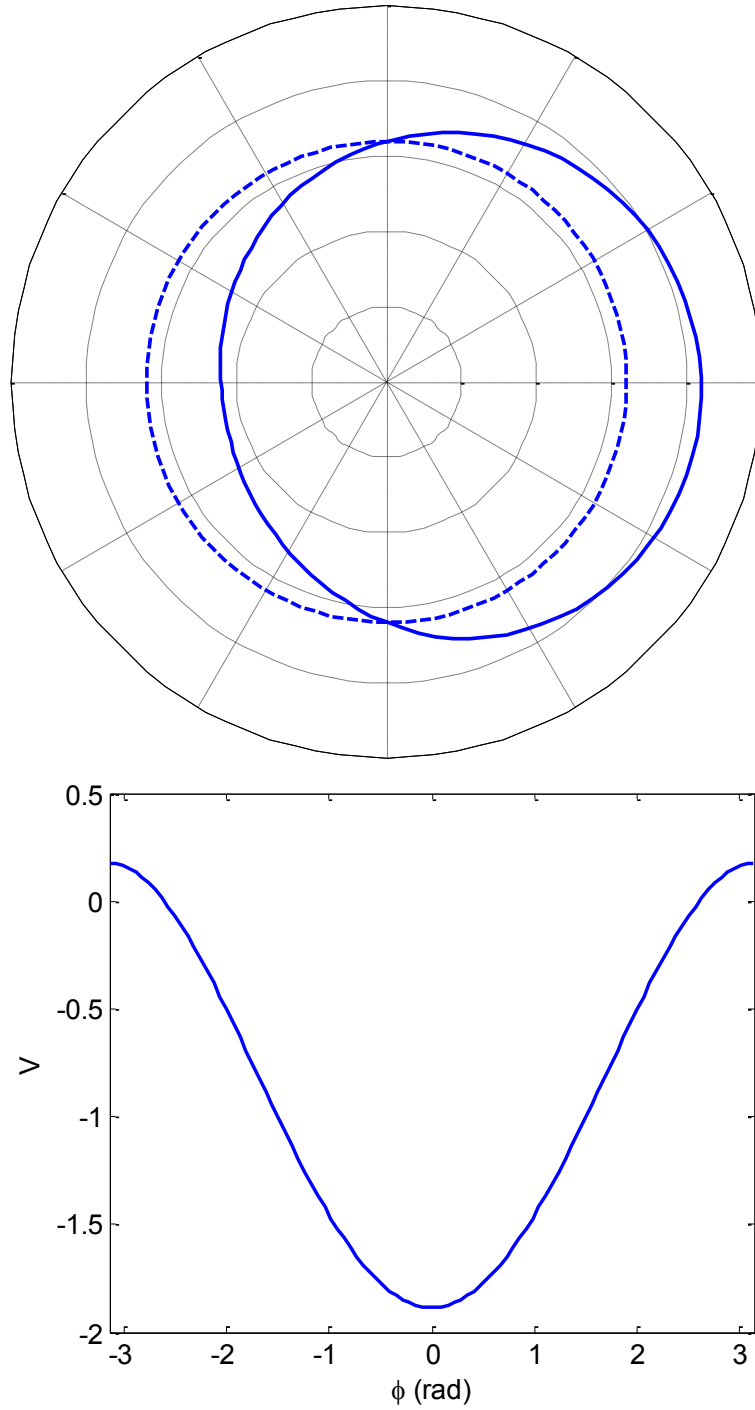


Figure 5.6: The third mode of the hybrid quarter-car model with a non-rotating tire. The radial displacement of tire U (top) and the tangential displacement of tire V (below). $\omega=140.0543 \text{ rad/s}$, $Z_s=0$, $Z_u=0$, $X_u=0.1783$

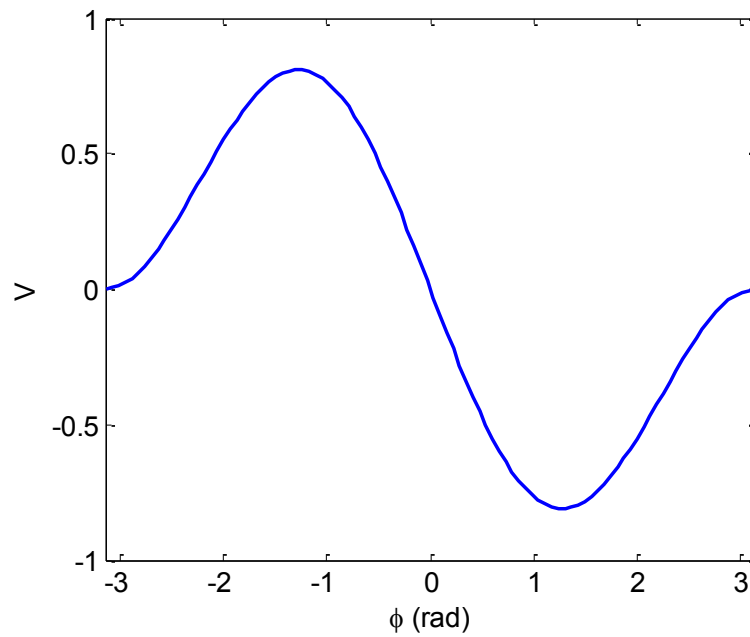
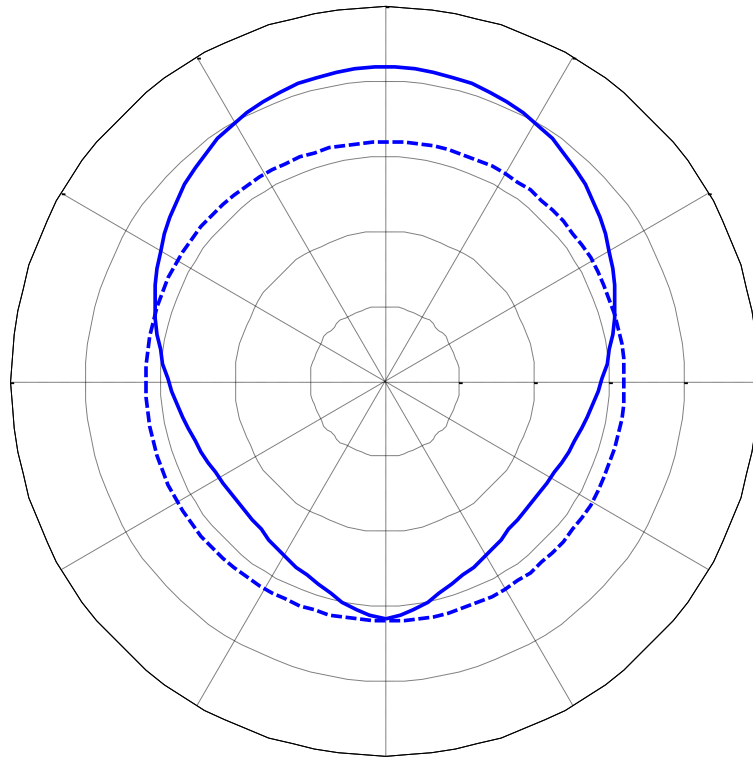


Figure 5.7: The fourth mode of the hybrid quarter-car model with a non-rotating tire. The radial displacement of the tire U (top) and the tangential displacement of the tire V (below). $\omega=282.2011$ rad/s, $Z_s=3.5357\times 10^{-5}$, $Z_u=-0.0313$, $X_u=-2.1152\times 10^{-8}$

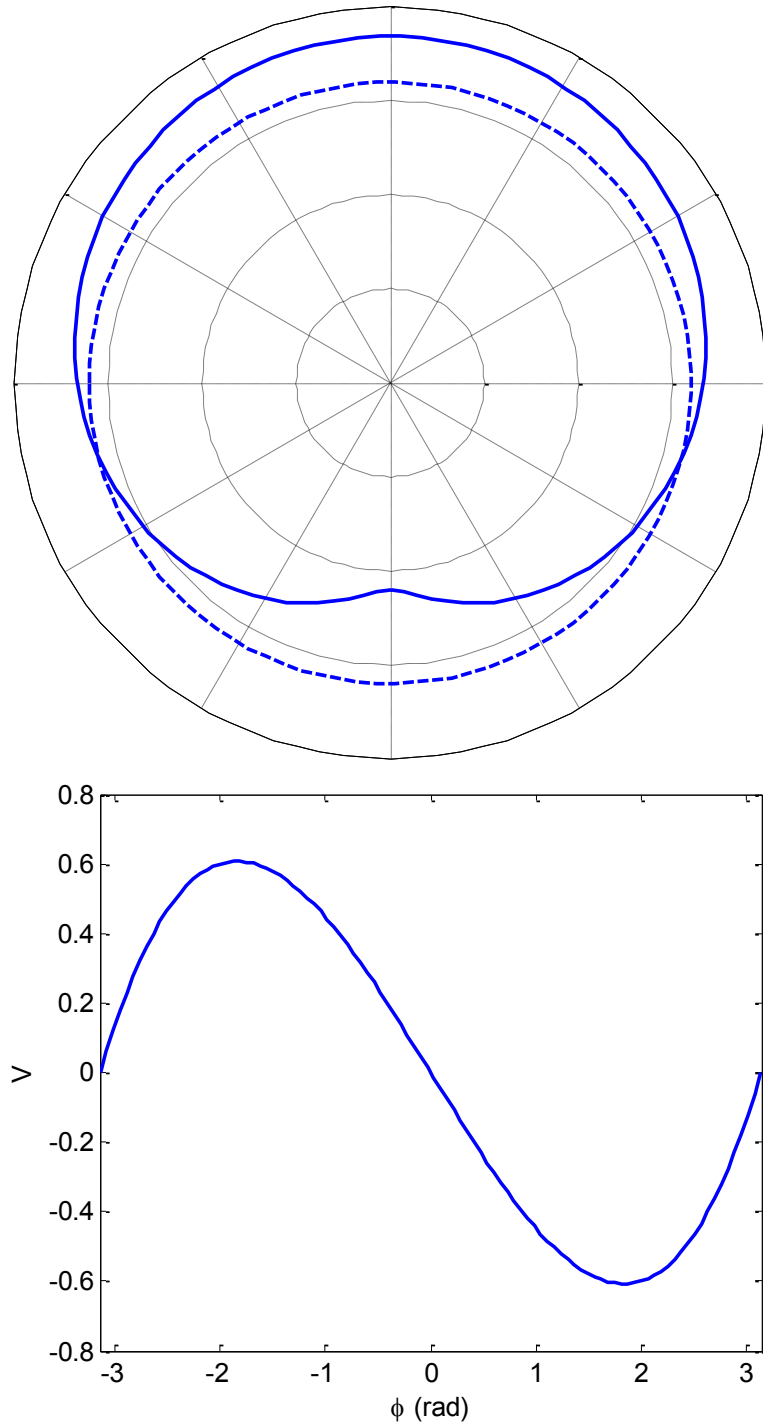


Figure 5.8: The first mode of the hybrid quarter-car model with a rotating tire $\bar{\omega}=100$ rad/s. The radial displacement U (top) and tangential displacement V (below). $\omega=8.4712$ rad/s, $Z_s=-4.9300-0.2114i$, $Z_u=-0.9991-0.0428i$, $X_u \approx 0$

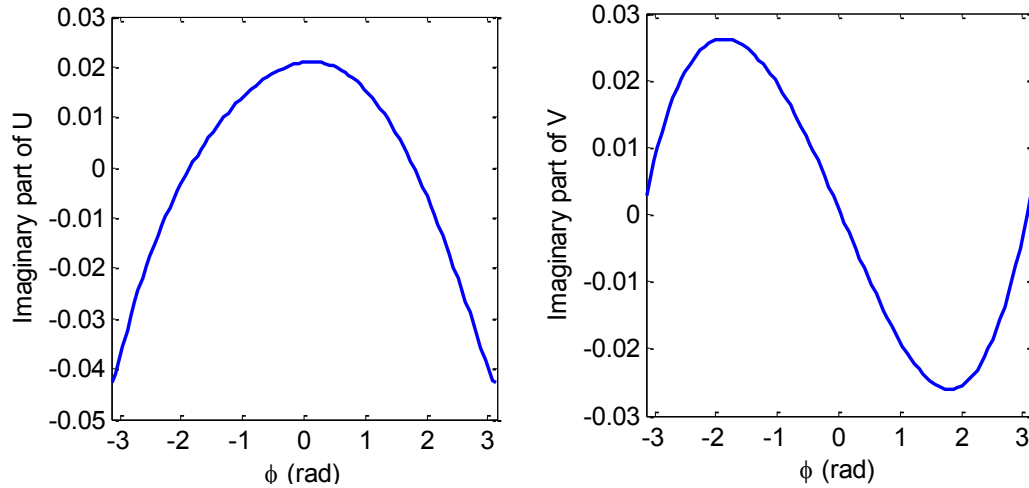


Figure 5.9: The imaginary parts of the displacements of the rotating ring at the first mode $\bar{\omega}=100$ *rad/s*. $\omega=8.4712$ *rad/s* radial displacement (left) and tangential displacement (right)

Figure 5.8 demonstrates the first mode of the hybrid quarter-car model with a rotating ring ($\bar{\omega}=100$). The radial and tangential displacements are similar to those of the model with a non-rotating ring (Figure 5.4). The difference is that the modes become complex when there is rotation. Figure 5.8 shows only the real parts of the radial and tangential displacements of the ring. Figure 5.9 demonstrates the imaginary parts of U and V at the first mode. The maximum of the imaginary parts reaches 4% of the maximum of the real parts for the first natural frequency. Similar to the results for the model with a non-rotating ring, the amplitude of the sprung mass vibration is larger than the amplitude of Z_u . Both displacements are in phase.

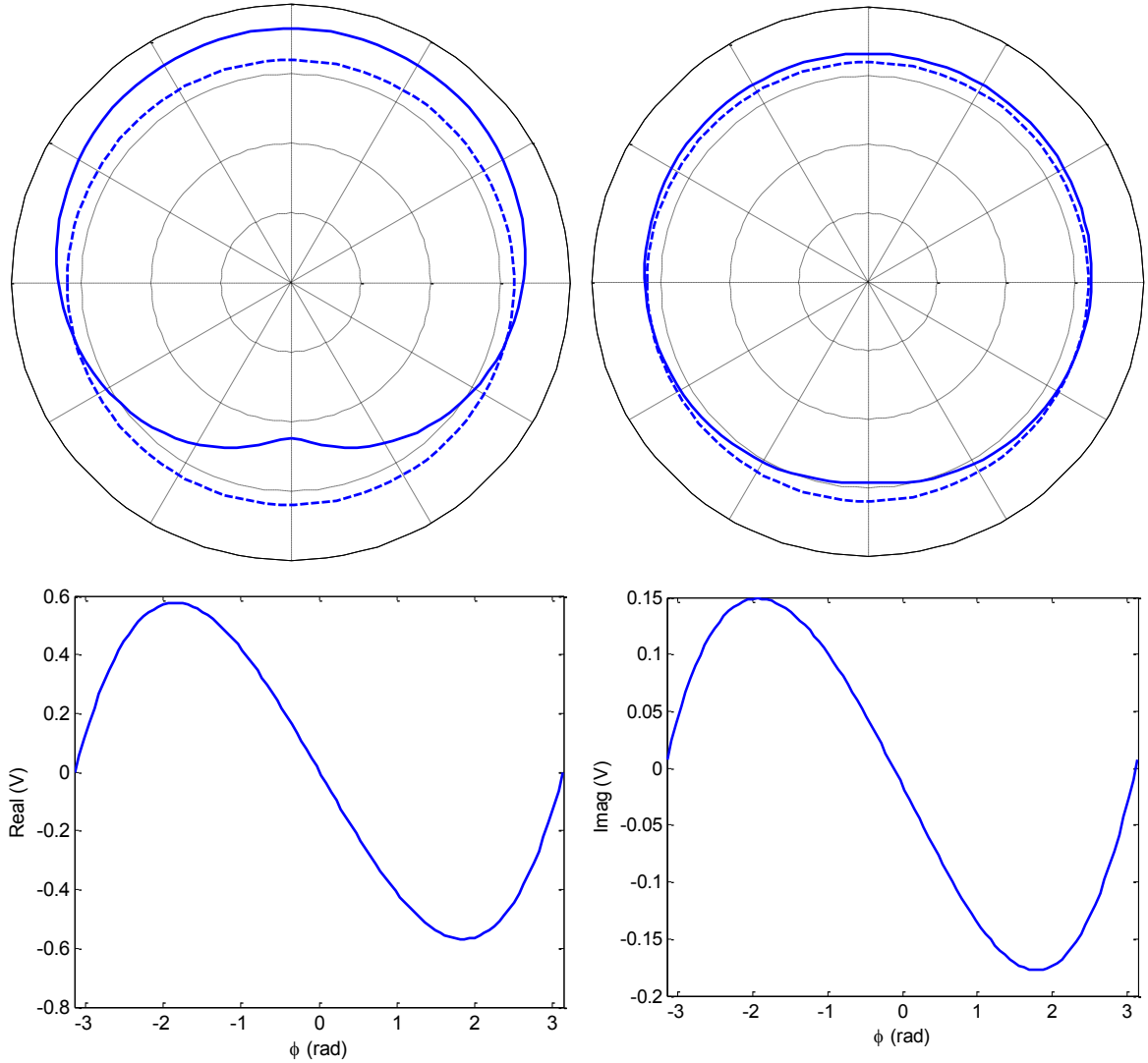


Figure 5.10: The second mode of the hybrid quarter-car model with a rotating tire $\bar{\omega}=100$ rad/s. The real and imaginary parts of the radial displacement of the ring U (top) and real and imaginary parts of the tangential displacement of the ring V (below). $\omega=54.7260$ rad/s, $Z_s=0.0298 + 0.0085i$, $Z_u= -0.9618 - 0.2736i$, $X_u=-0.0021 + 0.0072i$

Figures 5.10 to 5.13 show the higher modes of the hybrid quarter-car model with a rotating ring. The ratio of the imaginary part of the mode to real part becomes considerable as the natural frequency increases. It should be noted that the complex modes are to be multiplied by $e^{j\omega t}$. The modes appear to an observer as the combination

of the real and the imaginary parts. Apparently, at the higher modes, the magnitudes of the radial and tangential displacements that occur at the ring are larger than the displacement of the sprung mass or those of the unsprung mass.

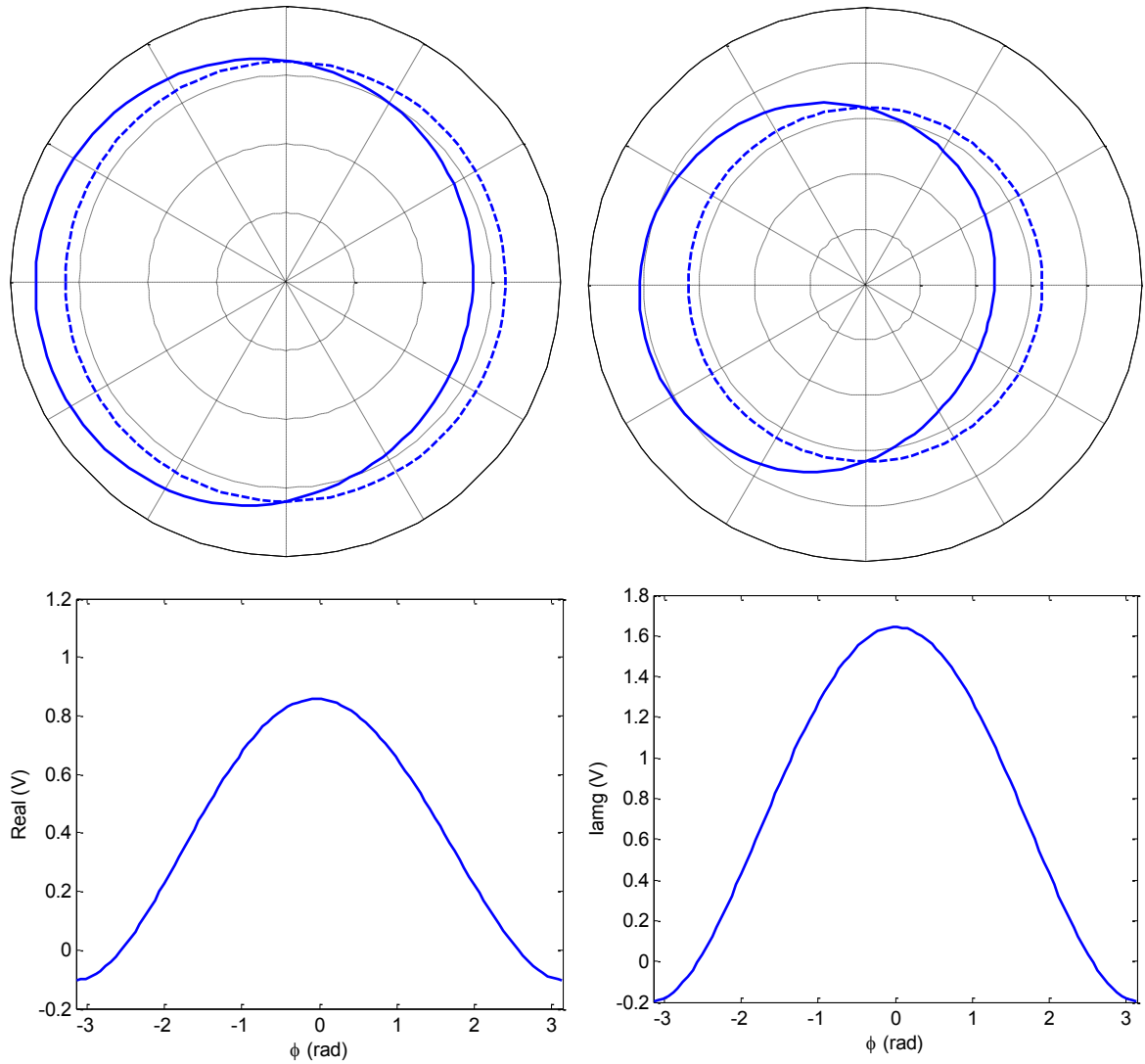


Figure 5.11: The third mode of the hybrid quarter-car model with a rotating tire $\bar{\omega}=100 \text{ rad/s}$. The real and imaginary parts of the radial displacement of the ring U (top) and the real and imaginary parts of the tangential displacement of the ring V (below). $\omega=134.5266 \text{ rad/s}$, $Z_s=1.6857 \times 10^{-5} - 8.7983 \times 10^{-6}i$, $Z_u= -0.0034 + 0.0018i$, $X_u= -0.1028 - 0.1970i$

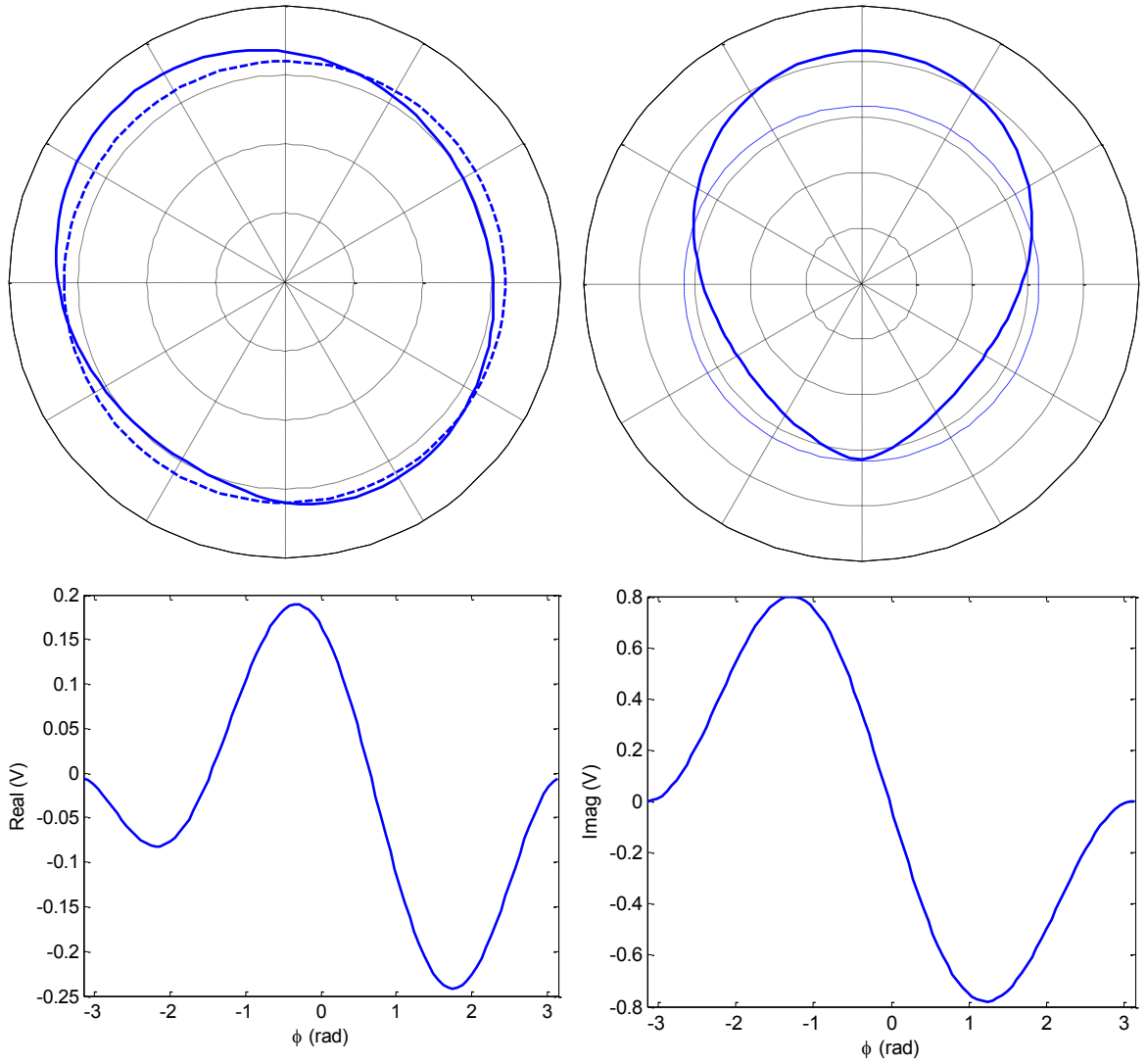


Figure 5.12: The fourth mode of the hybrid quarter-car model with a rotating tire $\bar{\omega}=100$ rad/s. The real and imaginary parts of the radial displacement U (top) and the real and imaginary parts of the tangential displacement V (below). $\omega=283.9394$ rad/s, $Z_s=5.5252\times 10^{-6} - 3.8434\times 10^{-5}i$, $Z_u= - 0.0049 - 0.0344i$, $X_u= -0.0061 + 0.0009i$

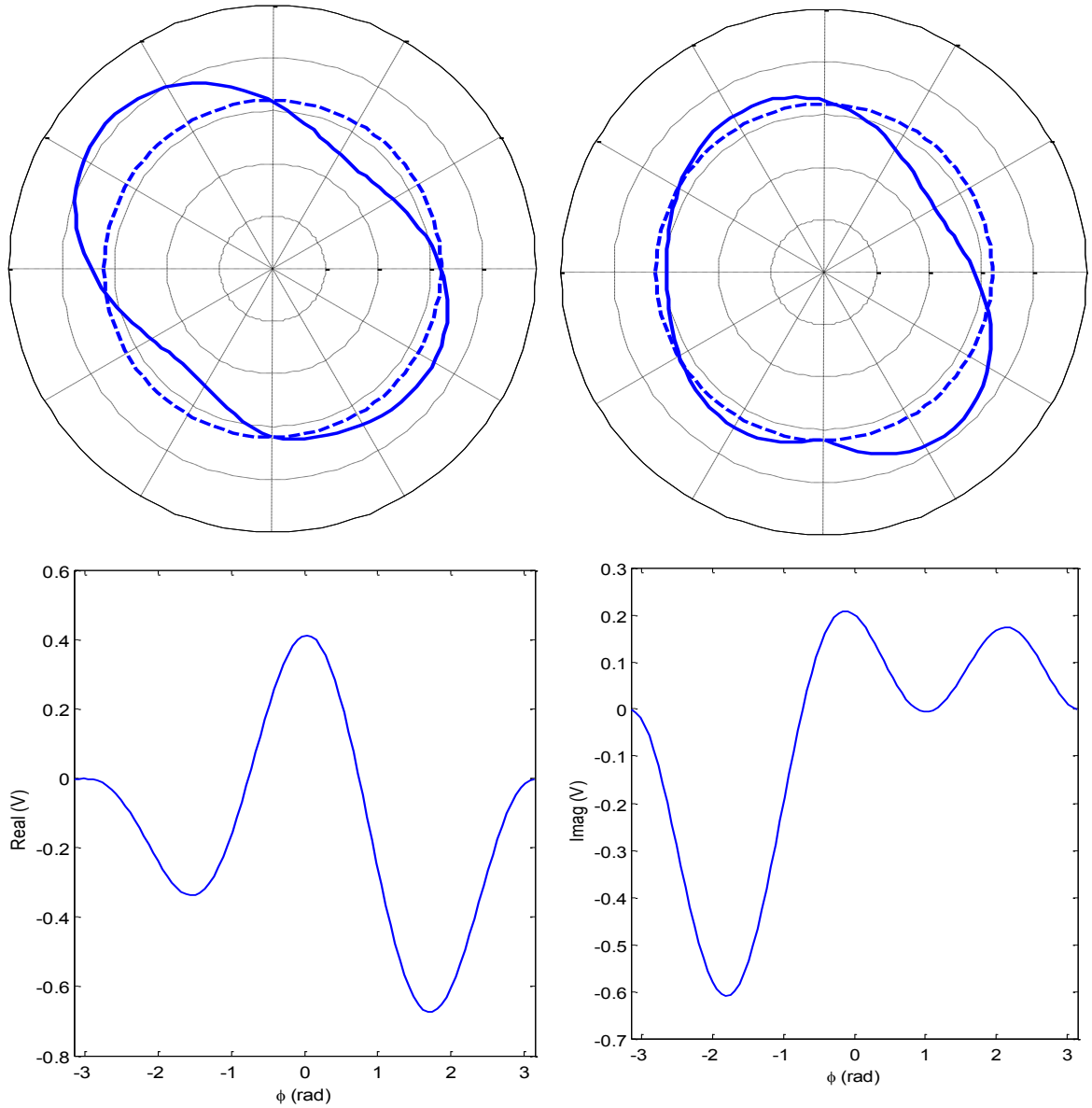


Figure 5.13: The fifth mode of the hybrid quarter-car model with a rotating tire $\bar{\omega}=100$ rad/s. The real and imaginary parts of the radial displacement U (top) and the real and imaginary parts of the tangential displacement V (below). $\omega=416.7889$ rad/s, $Z_s=1.3268\times 10^{-6}-2.7162\times 10^{-6}i$, $Z_u=-0.0026+0.0052i$, $X_u=-0.0033-0.0016i$

The real parts of the radial and tangential displacements of the ring in Figure 5.10 are similar to the displacement at the first mode. The difference is that the sprung mass

displacement is larger in the first mode, moving in phase, whereas in the second mode, the vertical displacement of the sprung mass is smaller and it moves out of phase with respect to the unsprung mass.

5.4. CONCLUDING REMARKS

The analytical solution of a hybrid quarter-car model was obtained. The significance of the solution is that, unlike the rings that are fixed at the center, the center of the ring was free to move horizontally and vertically. The constraint was located at the contact point. This ring represented the model of a tire as a part of the hybrid quarter-car model. The ring is in contact with the road at all times, and the dynamic forces are applied through the contact area. The natural frequencies were obtained and compared with those obtained by using the approximate methods. The modes were presented. It was shown that the modes become complex when the ring rotates. This phenomenon was discovered in the experiments performed by Kindt et al. [78, 81]. Also the sprung mass displacement reduces at the higher modes, indicating that at the higher modes the tire displacements are more dominant.

In the next chapter, a mode summation solution is presented using the natural frequencies and the mode shapes obtained in this chapter. The purpose of the mode summation is to find the frequency response of the quarter-car model to harmonic road excitation. The frequency response is used to investigate the response of the vehicle system with a rotating tire to a random road excitation.

CHAPTER 6 VEHICLE RESPONSE TO ROAD EXCITATION

6.1. INTRODUCTION

The response of the hybrid quarter-car model of a vehicle to the excitation applied by the road is studied in this chapter. The road roughness Z_r is taken into account and its effects on the boundary conditions of the ring and on the kinetics of the tire are included. Also, the damping of the suspension system, which was neglected in previous chapters, is added. In the following sections, first the response of the hybrid quarter-car model to an external excitation is obtained by using the mode summation method. Then, by using these results, the frequency response of the system is obtained. Finally, the spectral densities of the contact forces and the displacement response of the model are studied when subjected to random road excitations corresponding to a standard road profile.

6.2. MODAL ANALYSIS

Figure 6.1 shows the hybrid quarter-car model subjected to road roughness. The vertical position of the center of the tire is introduced as Z'_u , which is equal to the sum of the displacements caused by the road roughness and by the tire deflection. In other words, the vertical position of the unsprung mass can be written as:

$$Z'_u(t) = Z_u(t) + Z_r(t) \quad (6.1)$$

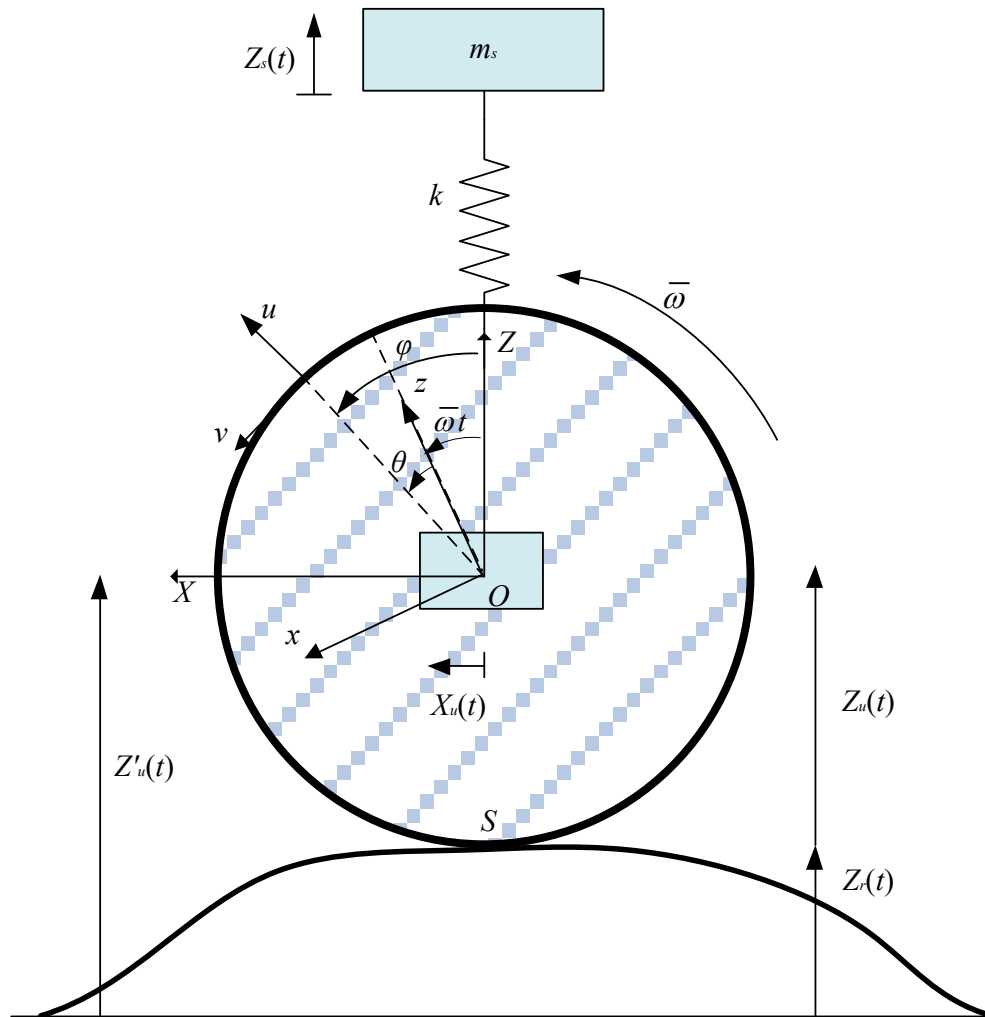


Figure 6.1: Schematic of a hybrid quarter-car model of a vehicle subjected to road roughness

where $Z_r(t)$ is the road profile and $Z_u(t)$ is the vertical displacement at the center of the tire caused by the radial displacement of the ring:

$$Z_u(t) = U(\pi, t) \quad (6.2)$$

By replacing Equation (6.1) in the equations of motion, the following equations are obtained.

$$\begin{aligned} \frac{EI}{a^4} \left(\frac{\partial^4 U}{\partial \varphi^4} - \frac{\partial^3 V}{\partial \varphi^3} \right) + \frac{EA}{a^2} \left(\frac{\partial V}{\partial \varphi} + U \right) - \frac{N_0}{a^2} \frac{\partial^2 U}{\partial \varphi^2} \\ + \rho A \left(\frac{D^2 U}{Dt^2} - 2\bar{\omega} \frac{DV}{Dt} - \bar{\omega}^2 U + \ddot{Z}_u \cos \varphi + \ddot{X}_u \sin \varphi \right) = -\rho A \ddot{Z}_r \cos \varphi \end{aligned} \quad (6.3)$$

$$\begin{aligned} \frac{EI}{a^4} \left(\frac{\partial^3 U}{\partial \varphi^3} - \frac{\partial^2 V}{\partial \varphi^2} \right) - \frac{EA}{a^2} \left(\frac{\partial^2 V}{\partial \varphi^2} + \frac{\partial U}{\partial \varphi} \right) \\ + \rho A \left(\frac{D^2 V}{Dt^2} + 2\bar{\omega} \frac{DU}{Dt} - \bar{\omega}^2 V - \ddot{Z}_u \sin \varphi + \ddot{X}_u \cos \varphi \right) = \rho A \ddot{Z}_r \sin \varphi \end{aligned} \quad (6.4)$$

$$\begin{aligned} m_w \ddot{Z}_u + m_t \ddot{Z}_u + k(Z_u - Z_s) + c(\dot{Z}_u - \dot{Z}_s) \\ + a \rho A \int_{-\pi}^{\pi} \left(\frac{\partial^2 U}{\partial t^2} \cos \varphi - \frac{\partial^2 V}{\partial t^2} \sin \varphi \right) d\varphi - T_z = -(m_w + m_t) \ddot{Z}_r - kZ_r - c\dot{Z}_r \end{aligned} \quad (6.5)$$

$$m_w \ddot{X}_u + m_t \ddot{X}_u + a \rho A \int_{-\pi}^{\pi} \left(\frac{\partial^2 U}{\partial t^2} \sin \varphi + \frac{\partial^2 V}{\partial t^2} \cos \varphi \right) d\varphi - T_x = 0 \quad (6.6)$$

$$m_s \ddot{Z}_s + k(Z_s - Z_u) + c(\dot{Z}_s - \dot{Z}_u) = kZ_r + c\dot{Z}_r \quad (6.7)$$

Since the road excitation is an input to the system, nonhomogeneous terms Z_r and its derivatives appear on the right-hand side of the equations above. Also, the damping of the suspension system is added.

In order to use the mode summation method, the solutions of Equations (6.3)–(6.7) are expressed as:

$$Z_u(t) = \sum_{n=1}^{\infty} Z_{un} q_n(t) \quad (6.8)$$

$$X_u(t) = \sum_{n=1}^{\infty} X_{un} q_n(t) \quad (6.9)$$

$$Z_s(t) = \sum_{n=1}^{\infty} Z_{sn} q_n(t) \quad (6.10)$$

$$U(\varphi, t) = \sum_{n=1}^{\infty} U_n(\varphi) q_n(t) \quad (6.11)$$

$$V(\varphi, t) = \sum_{n=1}^{\infty} V_n(\varphi) q_n(t) \quad (6.12)$$

where Z_{un} and X_{un} are the vertical and horizontal displacements of the center of the tire in the n^{th} mode of the system. Z_{sn} is the displacement of the vehicle body for the n^{th} mode, and U_n and V_n are the radial and tangential displacements of the n^{th} mode of the ring, respectively. The series above are truncated at the N^{th} terms and then substituted in Equations (6.3)–(6.7). After some mathematical operations, the equations are cast in the matrix form as:

$$[\mathbf{M}]\{\ddot{\mathbf{q}}\} + [\mathbf{C}]\{\dot{\mathbf{q}}\} + [\mathbf{K}]\{\mathbf{q}\} = \{\mathbf{F}\} \quad (6.13)$$

in which $[\mathbf{M}]$, $[\mathbf{C}]$, and $[\mathbf{K}]$ are $N \times N$ matrices. The external excitation on the right hand side of the equations consists of the forces caused by the road excitation as follows:

$$\begin{aligned} \{\mathbf{F}_m\} = & -\rho A \ddot{Z}_r \int_{-\pi}^{\pi} U_m(\varphi) \cos \varphi d\varphi + \rho A \ddot{Z}_r \int_{-\pi}^{\pi} V_m(\varphi) \sin \varphi d\varphi & m = 1, 2, \dots, N \\ & - \left(\frac{m_w + m_t}{a} \right) \ddot{Z}_r Z_{um} - \frac{k}{a} Z_r Z_{um} - \frac{c}{a} \dot{Z}_r Z_{um} + \frac{k}{a} Z_r Z_{sm} + \frac{c}{a} \dot{Z}_r Z_{sm} \end{aligned} \quad (6.14)$$

Solving Equation (6.13) will provide us with the radial and the tangential displacements of the ring and the displacements of the center of the tire (unsprung mass) and the vehicle body (sprung mass). Moreover, the damped frequencies of the hybrid quarter-car model can be obtained by equating the right-hand side of Equation (6.13) to zero. Table 6.1 tabulates the damped frequencies of the hybrid quarter-car model at different angular velocities. The first column refers to the model with a non-rotating ring. In other words, it means the frequencies of a vehicle that is not moving. The first, second, and the fourth frequencies are complex because of the addition of the damping. At the other frequencies, the real parts of the frequencies are negligible. As the angular velocity of the ring is increased, the real parts also increase. Also the damped frequencies are lower than the natural frequencies. For example, the fifth and sixth natural frequencies of the model with $\bar{\omega} = 100 \text{ rad/s}$ are 416.789 rad/s and 542.084 rad/s but the corresponding damped natural frequencies are $-21.14 \times 10^{-3} \pm j 399.56 \text{ rad/s}$ and $-1.07 \times 10^{-3} \pm j 472.13 \text{ rad/s}$.

Table 6.1: Comparison of the damped frequencies of the hybrid quarter-car model at different velocities

$\bar{\omega}=0$ (rad/s)	$\bar{\omega}=20$ (rad/s)	$\bar{\omega}=40$ (rad/s)	$\bar{\omega}=60$ (rad/s)	$\bar{\omega}=80$ (rad/s)	$\bar{\omega}=100$ (rad/s)
-2.62 ±j 8.27	-2.62 ±j 8.27	-2.64 ±j 8.28	-2.66 ±j 8.29	-2.69 ±j 8.30	-2.74 ±j 8.31
-27.62 ±j 41.45	-27.62 ±j 41.56	-27.59 ±j 41.88	-27.55 ±j 42.40	-27.49 ±j 43.11	-27.42 ±j 43.99
-1.46×10^{-12} ±j 140.05	-6.92×10^{-5} ±j 139.81	-0.27×10^{-3} ±j 139.10	-0.60×10^{-3} ±j 137.94	-1.40×10^{-3} ±j 136.38	-2.93×10^{-3} ±j 134.45
-0.42 ±j 282.11	-0.42 ±j 282.09	-0.43 ±j 282.04	-0.44 ±j 281.96	-0.46 ±j 281.88	-0.48 ±j 281.71
1.16×10^{-13} ±j 424.46	-0.79×10^{-3} ±j 423.82	-3.08×10^{-3} ±j 421.77	-7.46×10^{-3} ±j 417.86	-13.33×10^{-3} ±j 411.15	-21.14×10^{-3} ±j 399.56
-1.67×10^{-3} ±j 582.36	-1.56×10^{-3} ±j 578.22	-1.62×10^{-3} ±j 566.07	-0.46×10^{-3} ±j 546.23	0.21×10^{-3} ±j 517.54	-1.07×10^{-3} ±j 472.13
5.95×10^{-13} ±j 716.05	-1.57×10^{-3} ±j 713.95	-0.29×10^{-3} ±j 704.35	0.34×10^{-3} ±j 674.78	-0.98×10^{-3} ±j 601.68	0.44×10^{-3} ±j 486.09
-0.107×10^{-3} ±j 875.08	-9.68×10^{-5} ±j 861.63	-8.02×10^{-5} ±j 826.06	-0.11×10^{-3} ±j 772.18	-0.49×10^{-3} ±j 671.14	-1.49×10^{-3} ±j 585.52
-4.46×10^{-13} ±j 1003.37	-5.76×10^{-5} ±j 999.04	-0.17×10^{-3} ±j 966.62	1.95×10^{-3} ±j 869.76	-0.85×10^{-3} ±j 798.27	-1.38×10^{-3} ±j 785.47
-1.46×10^{-5} ±j 1167.30	-8.85×10^{-5} ±j 1138.32	-2.31×10^{-3} ±j 1076.97	-4.35×10^{-3} ±j 1032.55	-1.90×10^{-3} ±j 1009.72	0.92×10^{-3} ±j 1008.46
-7.14×10^{-13} ±j 1293.59	-3.07×10^{-5} ±j 1284.44	-1.91×10^{-3} ±j 1238.74	-1.70×10^{-3} ±j 1182.44	0.38×10^{-3} ±j 1151.64	2.28×10^{-3} ±j 1135.58

6.3. RANDOM VIBRATION ANALYSIS

The modal analysis introduced in the previous section is used to find the frequency response of the hybrid quarter-car model to the road harmonic excitation. Attention is given to the vertical contact forces T_z , the horizontal contact force T_x , the vertical displacement of the unsprung mass (center of the tire-wheel assembly) Z_u , the horizontal displacement of the tire hub X_u , the vertical displacement of the sprung mass (vehicle body) Z_s , and the vertical acceleration of the vehicle body \ddot{Z}_s . The parameters mentioned above are calculated for the frequency range of $\omega = 0 - 1000 \text{ rad/s}$ for the tire angular velocity of $\bar{\omega}=20, \bar{\omega}=40, \bar{\omega}=60, \bar{\omega}=80, \bar{\omega}=100 \text{ rad/s}$. Each angular velocity corresponds to a forward speed of $v = \bar{\omega}a$, where a is the radius of the ring. These forward speeds are 23, 46, 69, 92, and 115 km/h, respectively. The frequency response $H(\omega)$ that is obtained by applying a harmonic excitation in Equations (6.13) and (6.14) will be used in the calculation of the spectral densities. For example, the spectral density of the vertical contact forces T_z is obtained by using the following equation:

$$S_{T_z}(\omega) = |H_{T_z}(\omega)|^2 S_r(\omega) \quad (6.15)$$

where, $S_r(\omega)$ is the spectral density of the road. Many forms of road roughness spectral density models are available, corresponding to the type of the road. The present study uses the spectral density of the smooth road that is used by Sun [4] given by:

$$S_r(\omega) = \frac{1}{v} 3.37 \times 10^{-6} \left(\frac{\omega}{v} \right)^{-2.01} \quad (6.16)$$

where v is the forward speed of the vehicle in m/s . Figure 6.2 shows that the spectral density of the road roughness corresponds to an angular velocity of 60 rad/s and a forward speed of 69 km/h . The spectral density of the road roughness and the frequency response of the hybrid quarter-car model to a harmonic excitation are used to obtain the spectral density of the response of the hybrid model to road excitations. The results are presented in Figures 6.3 to 6.11.

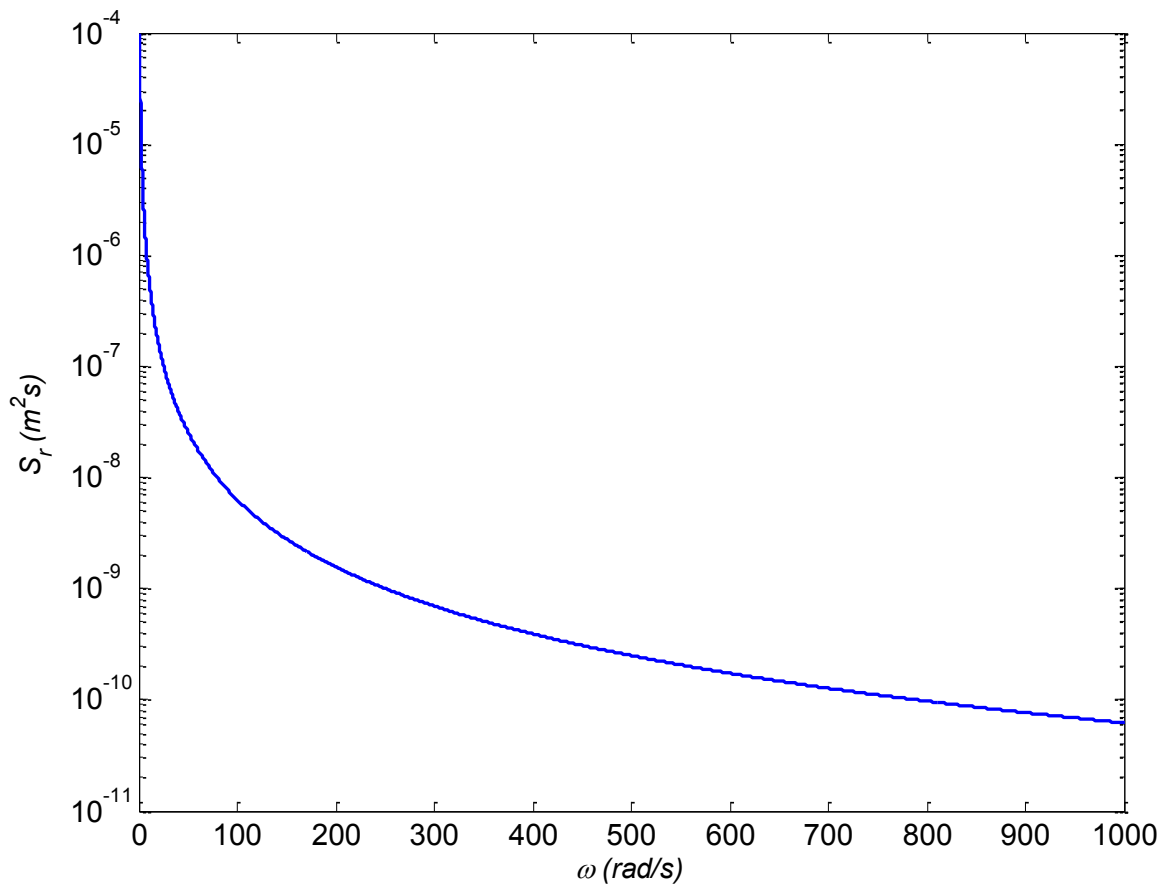


Figure 6.2: The spectral density of road roughness experienced by a passenger of a vehicle moving at $v=69 \text{ km/h}$ and tire angular velocity $\bar{\omega}=60 \text{ rad/s}$

Figure 6.3 shows the spectral density of the vertical contact force, T_z , of the hybrid quarter-car model at different velocities. Also the spectral density of the vertical contact force, T_z , of a traditional two degrees-of-freedom quarter-car model at different velocities is shown in Figure 6.4. Two damped frequencies of the 2DOF model are clear at the spectral density of the vertical contact force. However, Figure 6.3 shows the resonance at all the frequencies of the hybrid model.

Increasing the velocity of the vehicle causes a larger vertical force at the contact area. The magnitude of the mean square of the vertical contact force is tabulated in Table 6.2. Comparison shows that increasing the angular speed of the rotating tire from 20 to 100 rad/s makes the dynamic vertical force at the contact point 10 times larger. Although the vertical contact force for the 2 DOF model increases by increasing the speed, the rate is slower. The reason is that this model does not include the frequencies of the continuous system.

Figure 6.5 shows the horizontal force at the contact point between the rotating tire and the road. Since the 2-DOF system does not provide any results regarding the horizontal force, it is not possible to compare the two different models. The effect of the rotating velocity of the tire on the first five damped frequencies of the hybrid model is negligible. However, the frequencies above 400 rad/s decrease as the angular velocity increases. The mean square of the horizontal force, shown in Table 6.2, illustrates how the horizontal contact force increases at higher velocities.

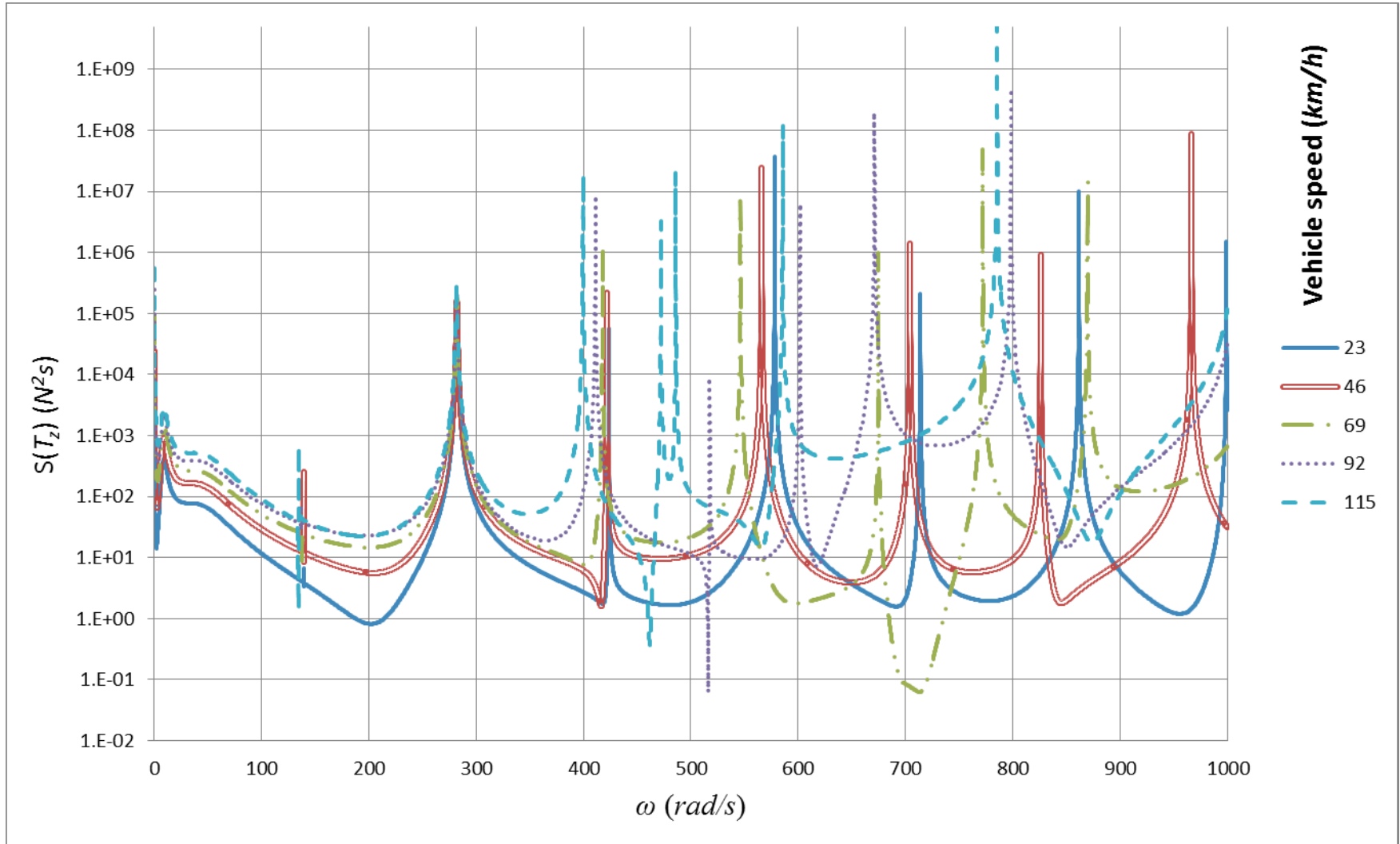


Figure 6.3: The spectral density of the vertical contact force of the hybrid quarter-car model

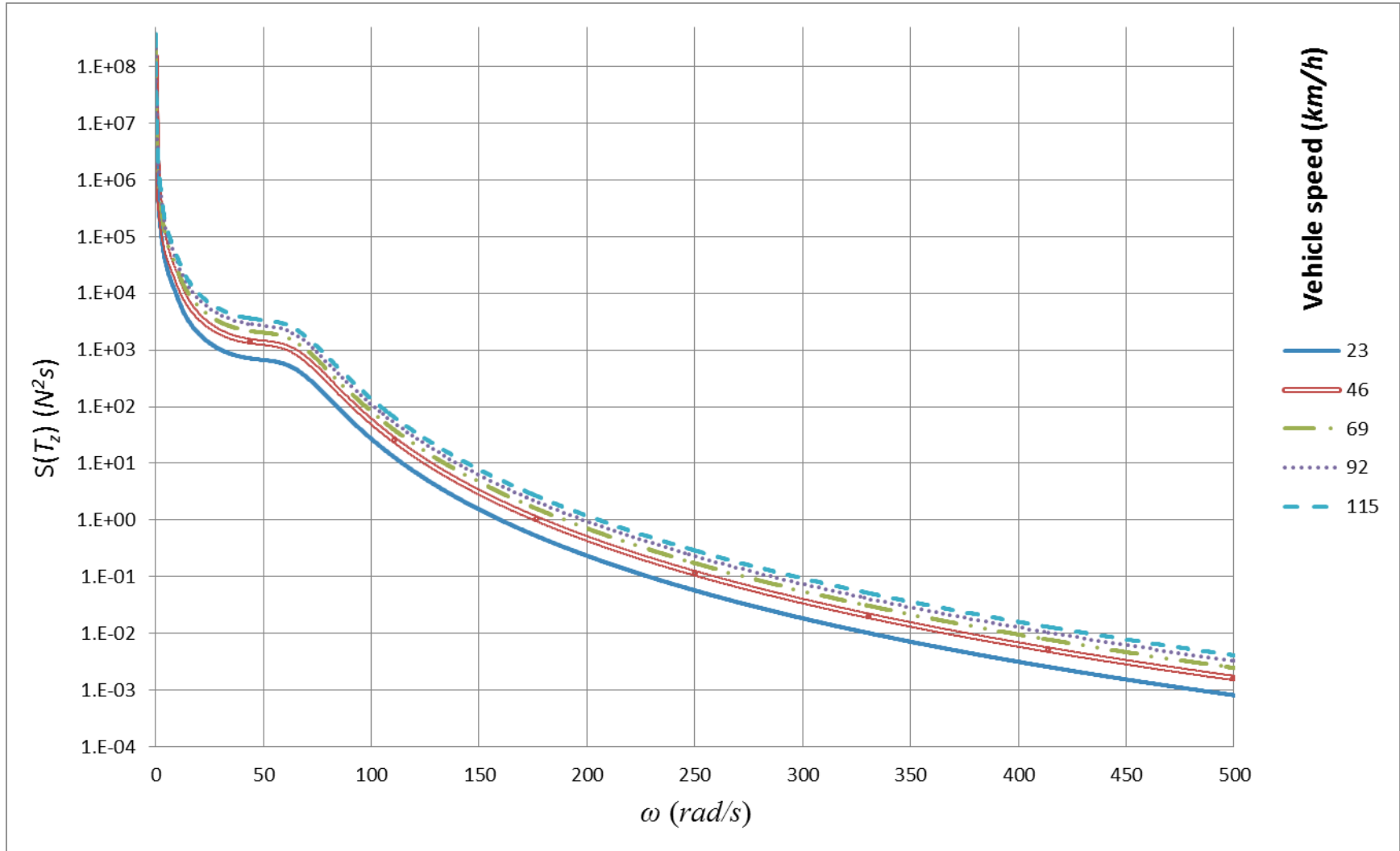


Figure 6.4: The spectral density of the vertical contact force of a 2-DOF quarter-car model

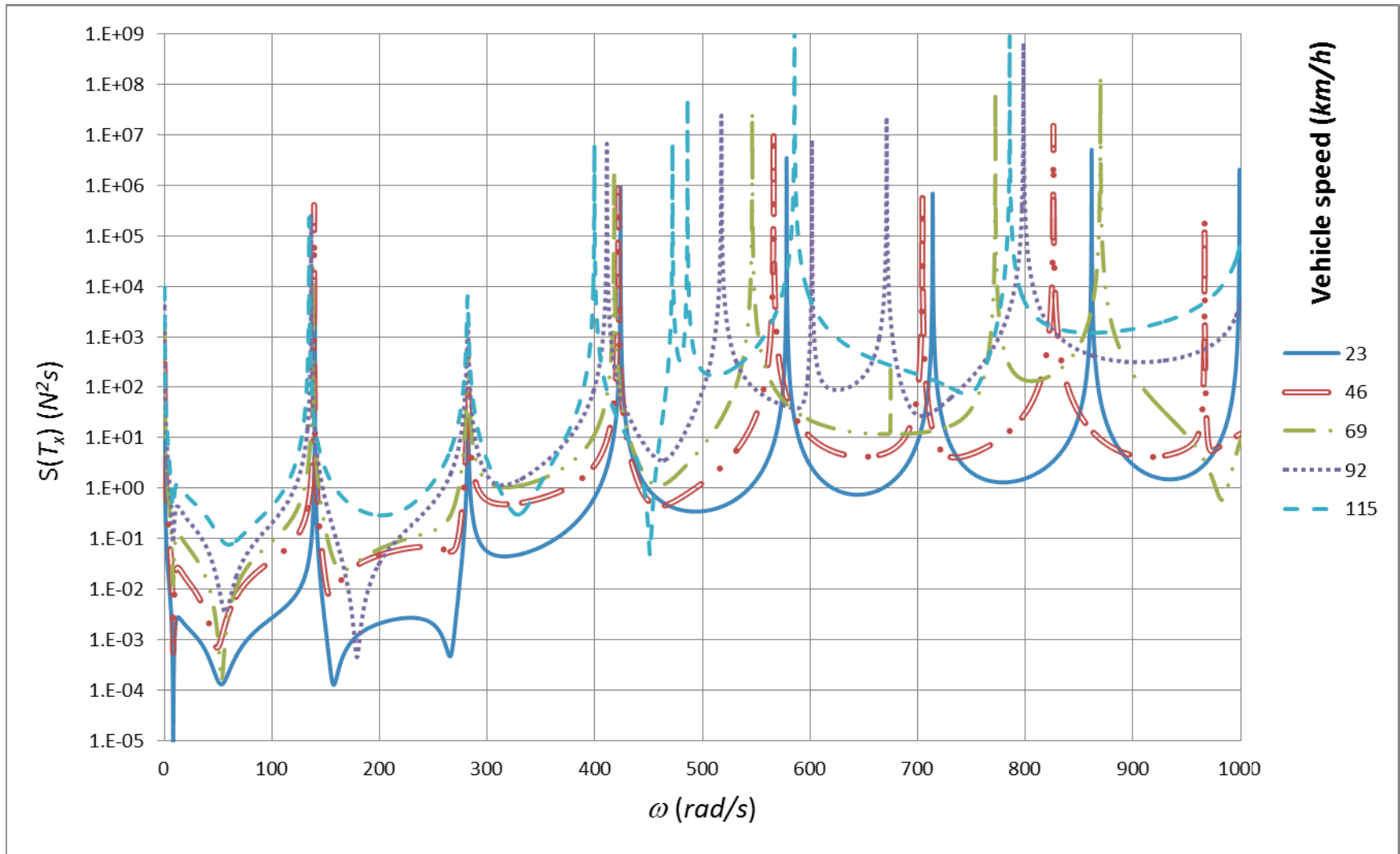


Figure 6.5: The spectral density of the horizontal contact force of the hybrid quarter-car model

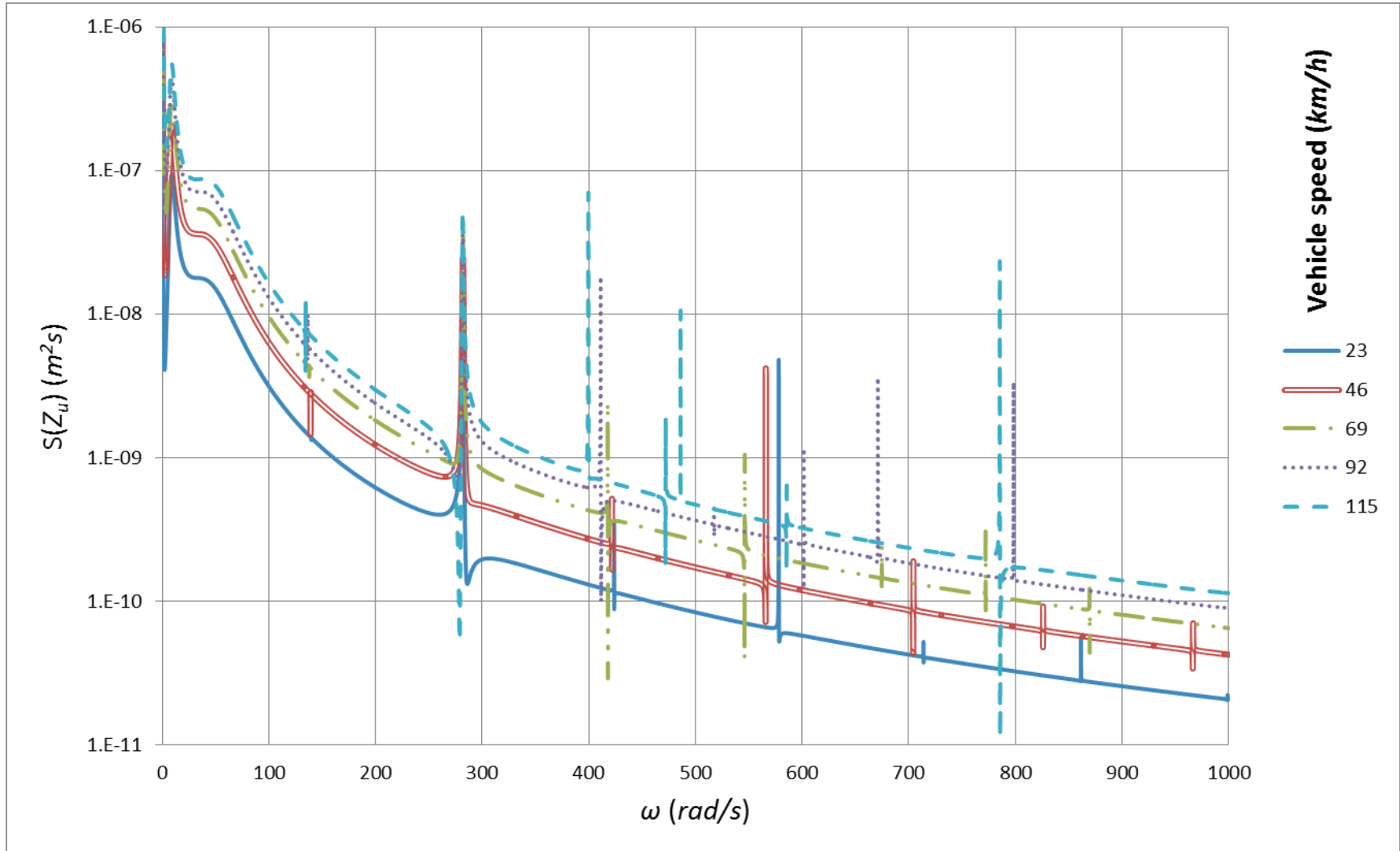


Figure 6.6: The spectral density of the vertical displacement of the center of tire for the hybrid quarter-car model

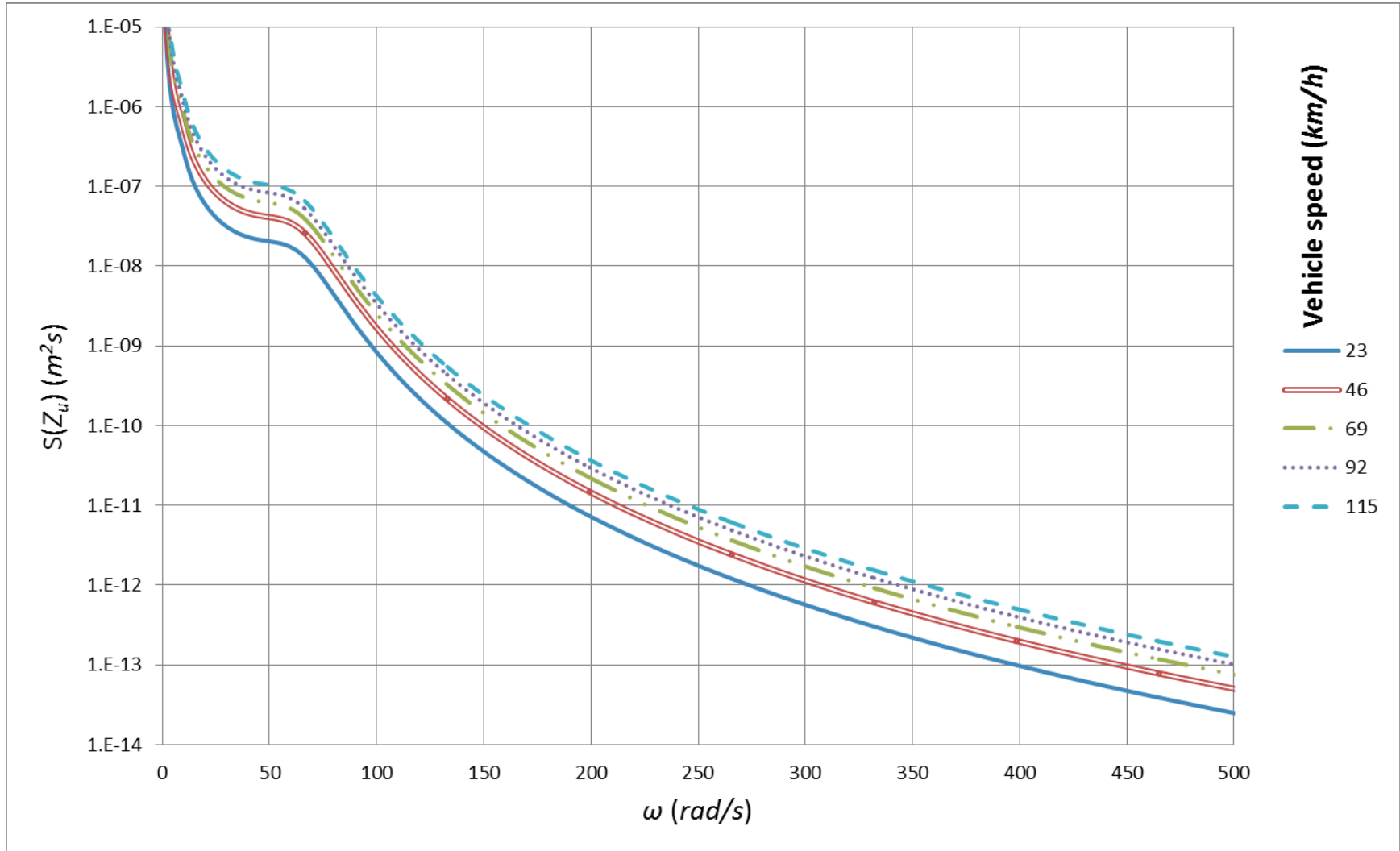


Figure 6.7: The spectral density of the vertical displacement of the unsprung mass (center of tire) for the 2DOF quarter-car model

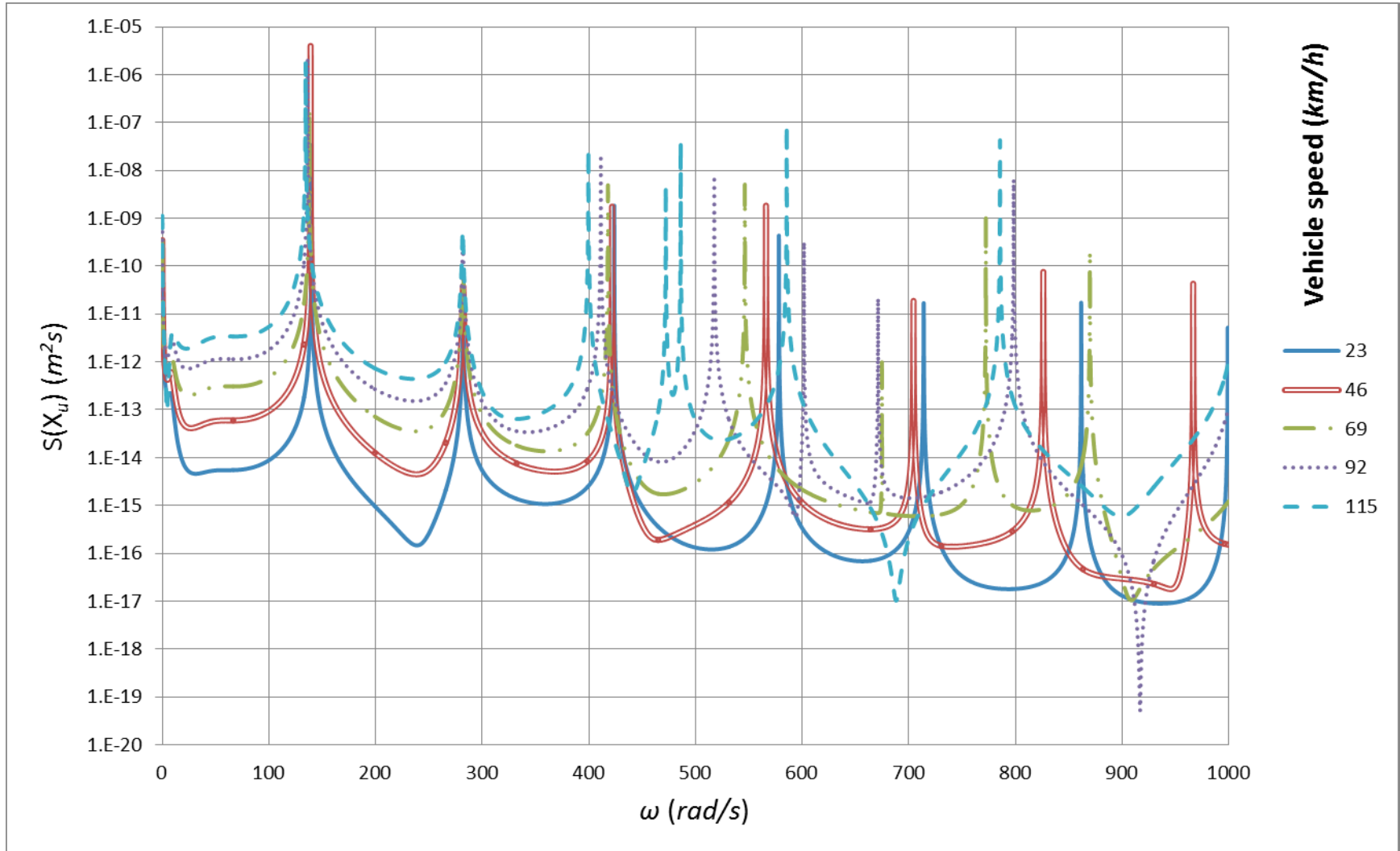


Figure 6.8: The spectral density of the horizontal displacement of the center of the tire for the hybrid quarter-car model

Figure 6.6 and Figure 6.7 show the spectral density of the vertical displacement of the center of the tire for the hybrid model and for the traditional 2-DOF model, respectively. In both figures, the results are shown for five different velocities. The magnitude of the displacement response for the hybrid model is higher than that obtained for the 2-DOF model. However, the mean square of the vertical displacement Z_u , presented in Table 6.2, indicates that the vertical displacement of the unsprung mass for the hybrid model is 100 times smaller, reflecting the effect of the dynamics of the rotating tire at higher frequencies. In other words, Z_u obtained by 2-DOF model is much larger than Z_u of the hybrid model. Figure 6.8 shows the spectral density of the horizontal displacement of the center of the tire for the hybrid model. Figure 6.6 and Figure 6.8, both show how the vehicle encounters higher displacement at higher speeds. Moreover, the magnitude of X_u is smaller than Z_u . There is also a difference between the vertical displacement and the horizontal displacement of the center of the tire. Z_u decreases quite rapidly as the frequency increases, but X_u does not show such behavior. X_u is obtained for a quarter-car model without the spring and the damper in the horizontal direction. In a real vehicle, the tire-road contact area acts like a spring in the horizontal direction. This characteristic is neglected in the present model.

Figure 6.9 and Figure 6.10 show the spectral density of the passenger vertical displacement in the case of the hybrid model with a rotating tire and in the case of the traditional 2-DOF model, respectively. The magnitude of the displacement decreases with increasing the frequency. The peaks at the damped natural frequencies of the hybrid system in Figure 6.9 are visible. There is a chance that these frequencies cause resonance

in the vehicle body. It should be noted that the peaks at a real vehicle are smaller because of the structural damping in the material of the tire.

Figure 6.11 shows the spectral density of the acceleration applied to the passenger in the hybrid quarter-car model. This acceleration directly affects passenger ride comfort. Until $\omega=200 \text{ rad/s}$, the magnitude of the spectral density of the acceleration decreases as ω increases, whereas for the frequencies above 200 rad/s , the spectral density of the acceleration increases. Figure 6.12 shows the spectral density of the acceleration applied to the passenger in the traditional 2 DOF quarter-car model. Compared with the results of the hybrid model, acceleration decreases as the frequency increases. This behavior happens because the 2 DOF model is not able to predict the behavior of the system at higher frequencies. A comparison of the mean square of the passenger acceleration in Table 6.2 shows that the increase of the speed increases the ride discomfort. The increase is more visible in the hybrid model with a rotating tire.

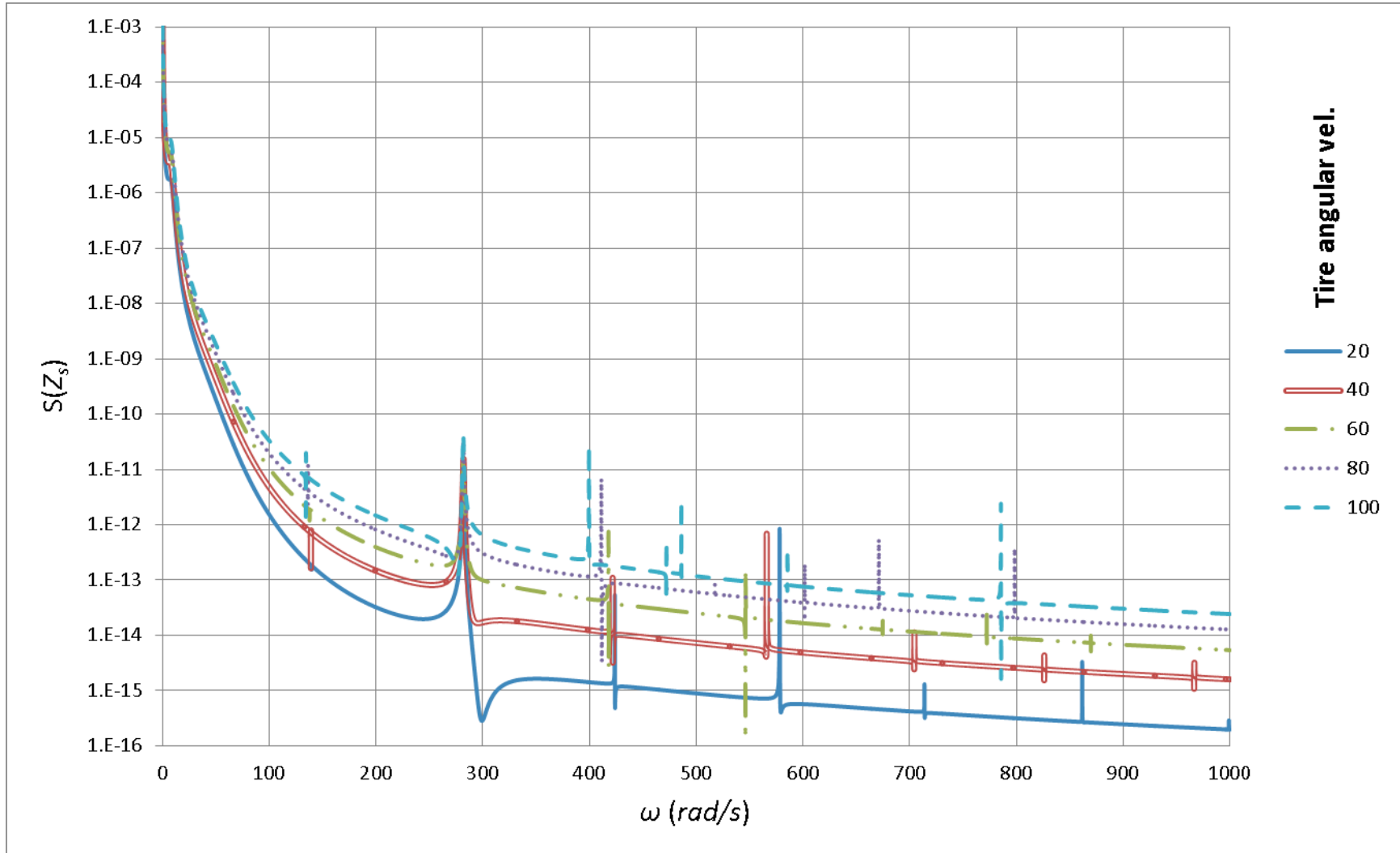


Figure 6.9: The spectral density of the vertical displacement of the passenger for the hybrid quarter-car model

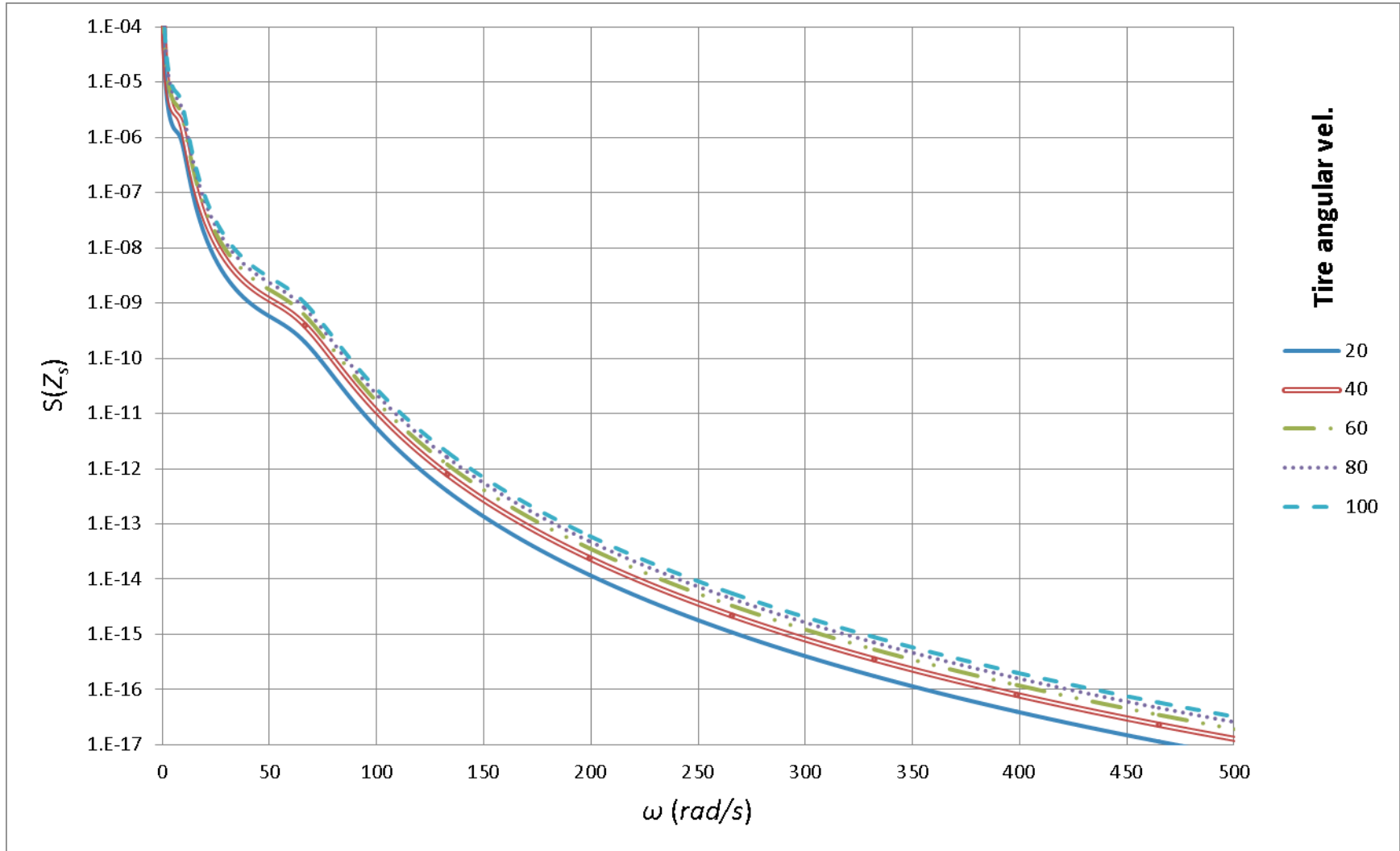


Figure 6.10: The spectral density of the vertical displacement of the passenger for the traditional 2DOF quarter-car model

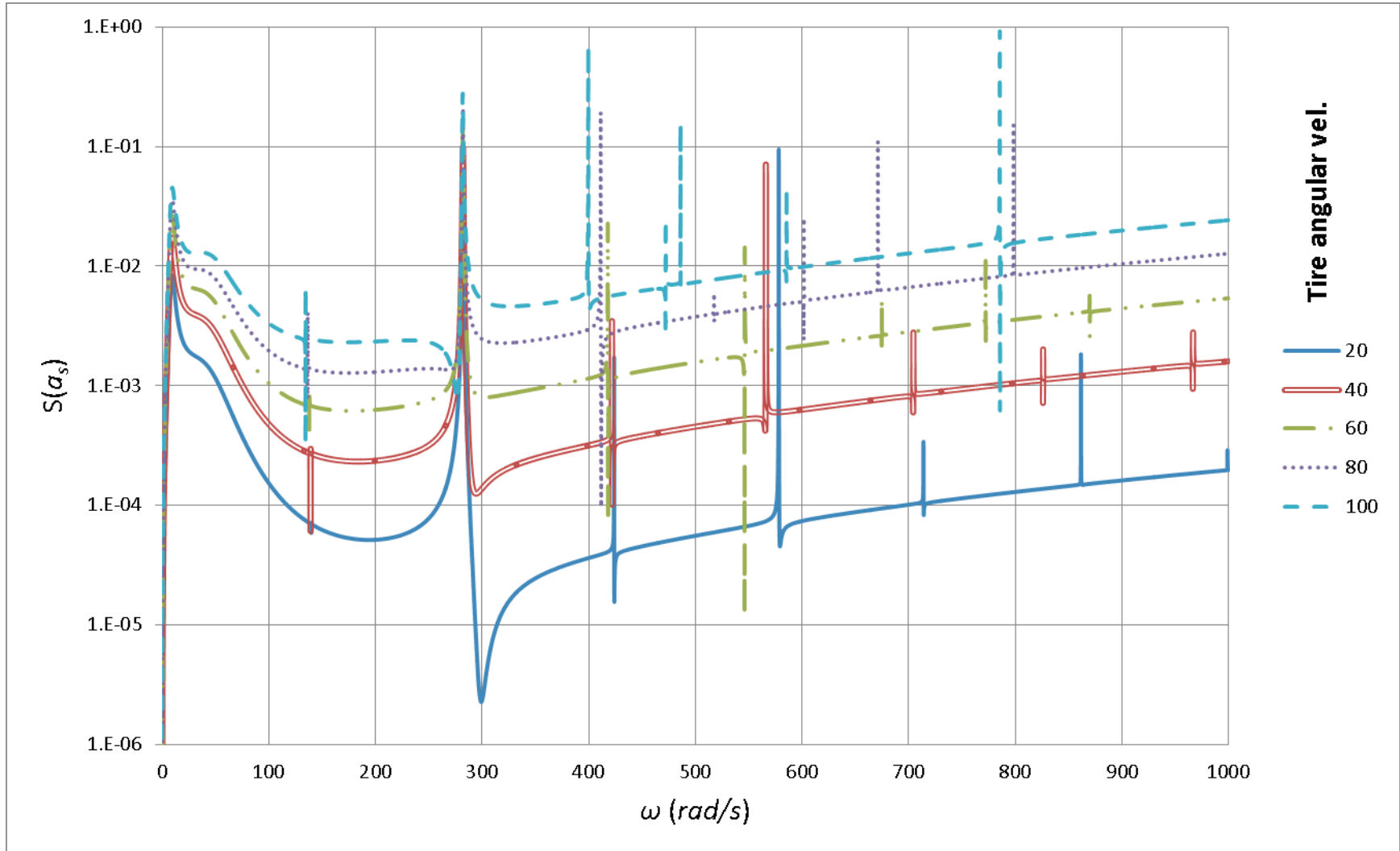


Figure 6.11: The spectral density of the vertical acceleration of the passenger for the hybrid quarter-car model

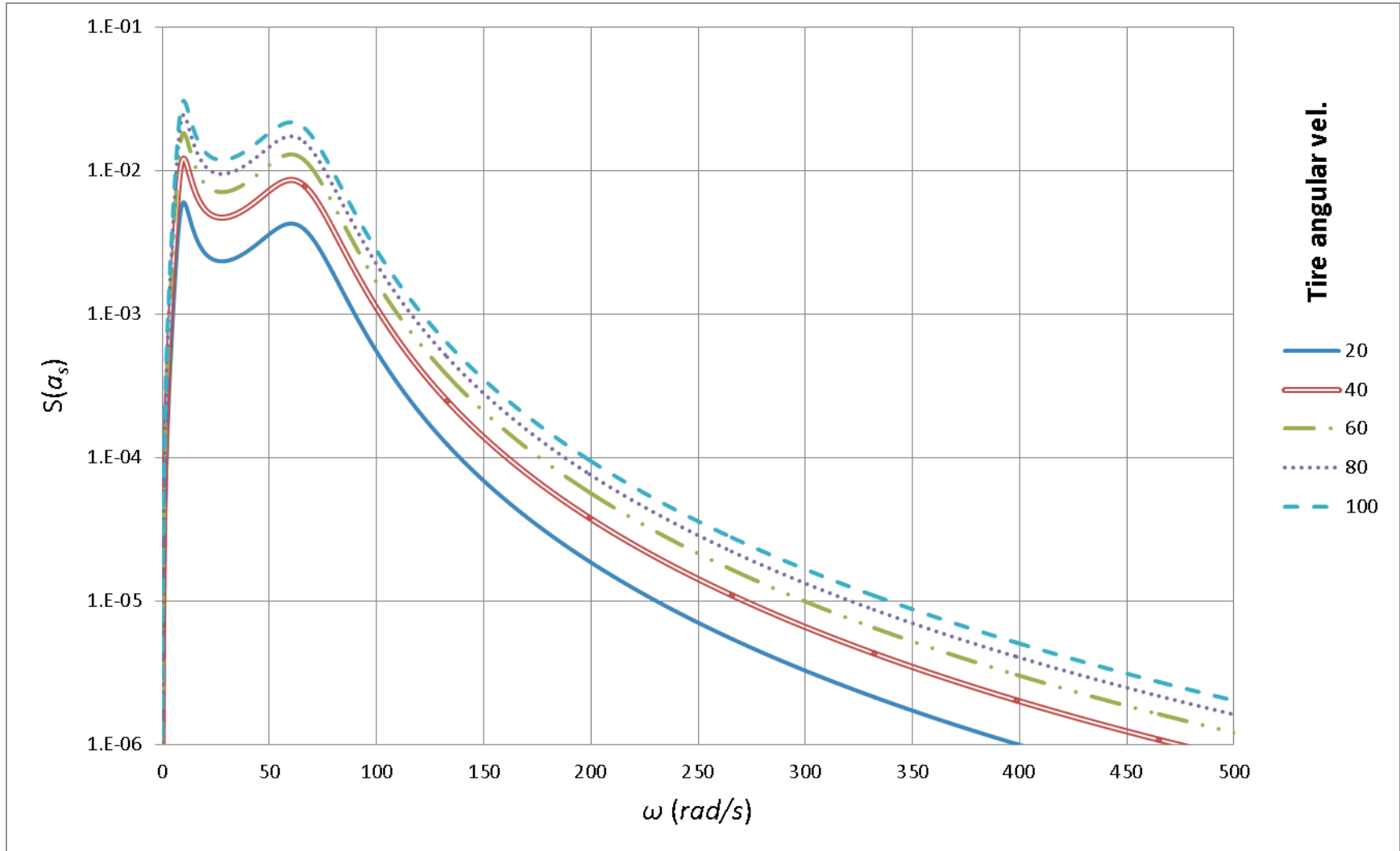


Figure 6.12: The spectral density of the vertical acceleration of the passenger for the traditional 2-DOF quarter-car model

Table 6.2: Comparison of the mean value of the responses to road excitation at different velocities

$\bar{\omega}$ (rad/s)	$E(T_z)$ (N^2)		$E(T_x)$ (N^2)	$E(Z_u)$ (m^2)		$E(X_u)$ (m^2)	$E(Z_s)$ (m^2)		$E(a_s)$ (m^2/s^4)	
	2 DOF	Hybrid Model	Hybrid Model	2 DOF	Hybrid Model	Hybrid Model	2 DOF	Hybrid Model	2 DOF	Hybrid Model
20	1.662×10^7	1.187×10^7	3.245×10^6	5.130×10^{-4}	3.951×10^{-6}	7.912×10^{-9}	5.222×10^{-4}	5.290×10^{-4}	0.5606	0.6051
40	3.348×10^7	2.705×10^7	8.338×10^6	1.033×10^{-3}	9.331×10^{-6}	8.063×10^{-7}	1.052×10^{-3}	1.067×10^{-3}	1.1289	2.1116
60	5.042×10^7	1.972×10^7	7.573×10^7	1.556×10^{-3}	1.712×10^{-5}	8.351×10^{-8}	1.584×10^{-3}	1.610×10^{-3}	1.7002	5.4917
80	6.742×10^7	2.125×10^8	2.055×10^8	2.081×10^{-3}	2.815×10^{-5}	5.493×10^{-7}	2.118×10^{-3}	2.156×10^{-3}	2.2735	11.7902
100	8.446×10^7	1.280×10^9	7.985×10^8	2.607×10^{-3}	4.296×10^{-5}	8.127×10^{-7}	2.653×10^{-3}	2.700×10^{-3}	2.8483	21.5608

6.4. CONCLUDING REMARKS

The effects of the suspension damping were considered in the hybrid vehicle model. The equations of motion were solved using the mode summation method. The damped frequencies were obtained for different angular speeds of the tire. Afterwards, the frequency responses and the spectral densities of the response, including the contact forces in both the vertical and horizontal directions, were studied.

The results showed that the higher frequencies of the tire affect the spectral densities of the response. All the spectral densities show a regional increase at the damped frequencies of the hybrid model. This phenomenon, if considered in combination with the higher frequencies of the body, will affect passenger ride comfort.

The next chapter presents the conclusions arrived at based on the results in this study. Chapter 7 also contains some suggestions for future studies on the dynamics of the rotating tire as well as the dynamics of vehicle systems.

CHAPTER 7 CONCLUSIONS AND SUGGESTIONS FOR FUTURE STUDIES

7.1. SUMMARY

The dynamics of the rotating tire are important from the point of view of the road induced vehicle vibrations, ride comfort, and noise. The tire also transfers the loads from the vehicle to the road. The unevenness of the road, which influences the passenger ride comfort, is applied initially to the tire, as it intervenes between the vehicle and the road. The core of the present study is to present a new dynamic model for a vehicle system, taking into account the effects of the rotating tire. A quarter-car model of the vehicle is used where a rotating ring represented the tire. The center of the ring was connected to the suspension system of the vehicle. The ring was in contact with the road, and the unevenness of the road is applied to the rotating ring.

The conventional model of a tire is a center-fixed ring. The effects of tire-road contact and the deformation at the contact area are not taken into account in the conventional model. At the beginning of this study, the dynamics of a center-fixed ring in both a rotating coordinate system and a non-rotating coordinate system were investigated. The bifurcation of the natural frequencies was discussed. Bifurcation splits the natural frequency of a non-rotating ring into a positive-going wave and a negative-going wave.

In the third chapter, the hybrid vehicle-tire-road model was introduced, and the equations of motion were derived. This model consists of a rotating ring and a spring-mass system that represents the vehicle body and suspension of the vehicle. In contrast to the conventional model, the center of the tire is not fixed. It is free to move in both the vertical and horizontal directions. The contact force, which is a function of both the dynamic response of the vehicle body and of the ring, is applied through the contact point.

The fourth chapter presented the natural vibration response of the model by using two different approximate methods: The Galerkin method and the finite element method. In the Galerkin method, the mass, stiffness, and damping matrices were obtained by using trigonometric admissible functions. On the other hand, in the finite element analysis, non-rotating elements in a non-rotating coordinate system were used. The rate of convergence for both methods was investigated. These approximate solutions have significant importance when the tire is modeled as a rotating shell or when the geometry of the side wall and thread patterns are investigated.

The closed-form solution of the hybrid quarter-car model was also obtained. The radial and tangential displacements of the ring were defined as relative displacements with respect to the center that moves horizontally and vertically. The natural frequencies were obtained and compared with those obtained by using the approximate methods. The complex mode shapes of a rotating ring in contact with the road were presented. The bifurcation of the frequencies does not occur in the hybrid model because of the forces and deformations at the contact point. The displacements of the sprung mass and of the unsprung mass at different modes, obtained for different velocities, showed the significance of the hybrid quarter-car model with a rotating ring.

Moreover, the mode summation method was used to obtain the damped frequencies of the hybrid model at different angular velocities. The functions, used in the mode summation method, were those of the undamped hybrid system obtained by using the analytical method. The spectral density of the response was obtained. The following parameters were investigated:

- The vertical displacement and acceleration of the passenger
- The vertical and horizontal displacements of the center of the tire (unsprung mass)
- The vertical and horizontal forces at the contact point

The responses were compared with the traditional 2 DOF quarter-car model.

It was shown that the road excitation creates large responses while the frequency of the excitation approaches the frequencies of the hybrid model. This phenomenon causes a large displacement, a large acceleration, and consequently considerable fatigue for both

the passenger and the vehicle body. Also the dynamic forces at the contact point affect the handling of the vehicle system.

The results of the present study are summarized as:

1. In both of the approximate solutions, the convergence rates of the response were investigated. It was shown that by using an adequate number of admissible functions in the Galerkin method or by using significant number of elements in the finite element analysis accurate answers are obtained. The maximum error between the results of the approximate methods and those of the closed-form solution is 13 % at the first frequency. However, in most of the cases the error is below 5%. The results can be improved by changing the admissible functions of the Galerkin method or interpolating functions in the finite element method. On the other hand, the analytical solution of a 2-D model is computationally more expensive than the approximate solutions. The approximate solutions are expandable to 3-D problems.
2. The natural frequencies of a rotating center-fixed ring, as a conventional model of the tire, bifurcate. The rate of the bifurcation is a function of the angular velocity of the ring. The symmetry of the rotating ring creates the bifurcation. The bifurcation disappears as the ring is used in the hybrid quarter-car model. There are distinct frequencies unlike the center-fixed ring. The realistic model of a tire carries the vehicle body and suspensions. Due to the weight of vehicle, the tire is deformed at the contact, and the symmetry of the ring is distorted. However, the frequencies of the hybrid quarter-car model show a slender curve-veering behavior.

3. The mode shapes of the hybrid quarter-car model are real only when the tire is stationary. The rotation of tire creates complex modes. The level of complexity increases with the angular velocity of the tire. Also, the higher modes of the vehicle show a larger level of complexity compared to lower modes. Measuring the modes of the tire using a laser instrument, Kindt et al. reported the existence of the complex mode shapes of the tire and the phase lag between the displacements of different points [79–81]. However, the angular velocity of the tire in their test was small, causing insignificant level of complexity. In the present study, it was shown that that the ratio of the real part of the mode to the imaginary part is considerable.
4. The conventional two degree-of-freedom model of a vehicle provides the first two frequencies of the vehicle. In the first frequency, the displacement of the sprung mass is more dominant, while in the second one the displacement of the unsprung mass is more dominant. However, the conventional 2-DOF model does not consider the effects of the rotation. Similarly, the first mode of the hybrid quarter-car model presents the dominance of the vertical displacement of the body while the second mode shows the supremacy of the vertical displacement of the center of the tire. Both of these frequencies are affected by the angular velocity of the tire. Increasing the speed increases the natural frequencies of the hybrid model. Another advantage of the hybrid model is its ability to estimate the frequency response of the displacements of the passenger and the tire at higher frequencies. Comparisons show that at higher frequencies, the spectral densities of these displacements in the hybrid model are larger than those in 2-DOF model. This can be explained by noting that the 2-DOF model does not contain the higher natural frequencies of the vehicle. Consequently,

the mean value of the vertical acceleration felt by the passenger in the hybrid model is greater than that of the conventional 2-DOF model. Moreover, the hybrid model provides more information about the horizontal force at the contact and the horizontal displacement of the center of the tire.

5. All of the damped natural frequencies of the hybrid model are functions of the angular velocity of the tire. The first four frequencies are slightly changed by increasing the angular velocity. However, the variation of the damped natural frequencies by angular velocity of the tire significantly increases at higher frequencies. For instance, a 25 percent increase of the angular velocity of the tire caused a 20 % decrease of the 7th damped natural frequency of the hybrid model. The damping in the suspension of the vehicle only influenced the first and the second frequencies of the hybrid model significantly.
6. The spectral densities of the response for the hybrid model show large amplitudes at the frequencies close to the natural frequencies of the system, influencing the ride comfort and the ride noise considerably. Moreover, the spectral density of the response is larger for a higher angular velocity. However, this increase has significantly more important effect on the contact forces and the vertical acceleration of the passenger, compared to the increase of the displacement of the tire center. For instance, the mean value of the spectral density of the vertical contact force and the acceleration of the passenger at $\bar{\omega}=100 \text{ rad/s}$ are 100 and 35 times as large as those at $\bar{\omega}=20 \text{ rad/s}$, respectively.

7.2. SUGGESTIONS FOR FUTURE STUDIES

In order to study the influence of the rotational dynamics of the tire on the vehicle bounce vibrations, the following investigations are suggested for future study:

- Analyzing the effect of a contact surface instead of a contact point

As explained, the assumption of the contact point between the road and the tire is an ideal assumption that helps to avoid non-linearity. In reality, the tire lies on a contact surface area due to the static deformation of the tire caused by the weight of the vehicle. It is preferable to replace the contact point by a contact surface, as shown in Figure 7.1. The contact patch can be assumed as a beam to which the forces are applied. Then, the equations of the beam and of the ring should be solved simultaneously in order to satisfy the compatibility conditions between the ring and the beam.

- Comparing a 2-D model with an equivalent 3-D model

A shell should be considered as a 3-D model, and then the contact force and constraint would be applied. The contact force could be applied through a line of contact. This would enable an investigation of the effects of the contact force in the third dimension perpendicular to the rotation plane and would enable a comparison of the results with those of a 2-D model. The effect of the lateral vibration and of the lateral force could be investigated.

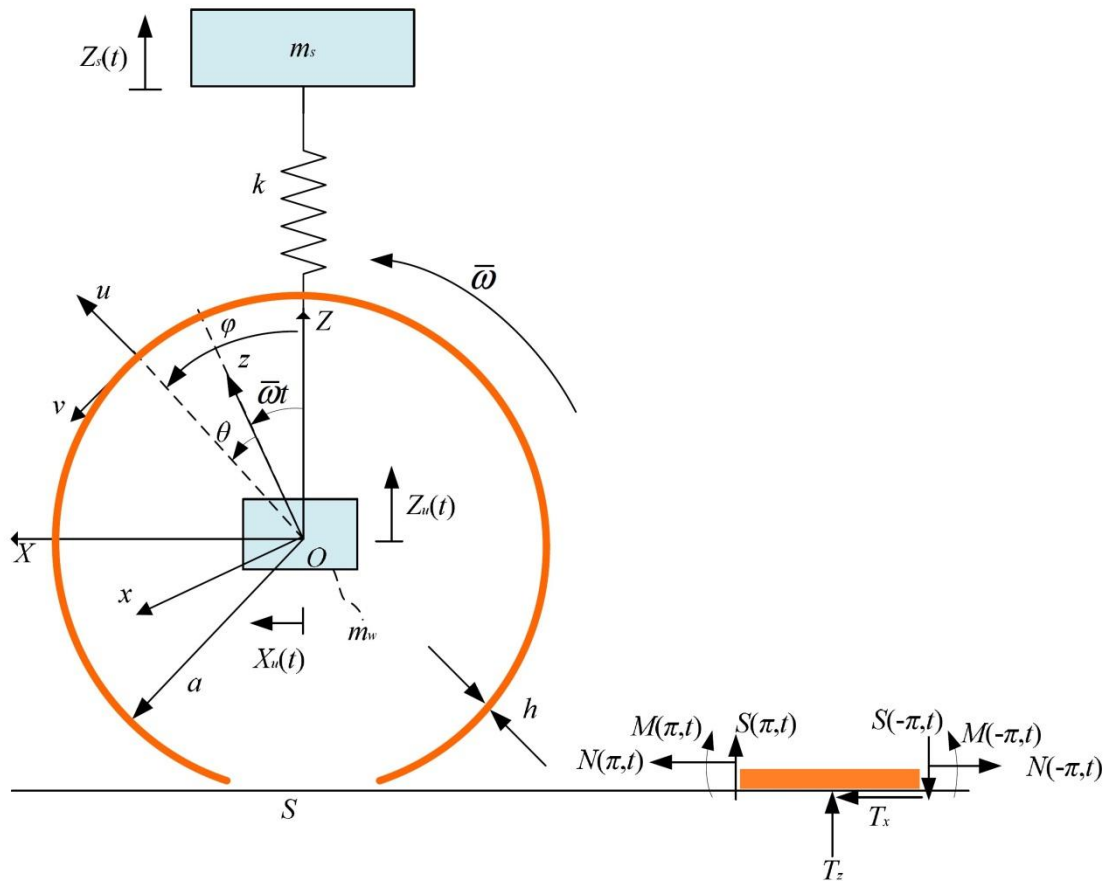


Figure 7.1: Schematic of a 2-D model of a vehicle. The contact area is assumed as a beam

- Modeling a rotating tire with a side wall and a contact patch by using a 3-D finite element analysis

A finite element model of a tire with a road contact could be analyzed. The cross section of a real tire could be modeled, and the effect of the vibration of the side wall could be added. Also the Coriolis and centrifugal accelerations would be taken into account, and a finite element approach in a non-rotating coordinate system would be used to solve the

problem. Similar to this study, the center of the tire should be released so that it could move freely in any direction.

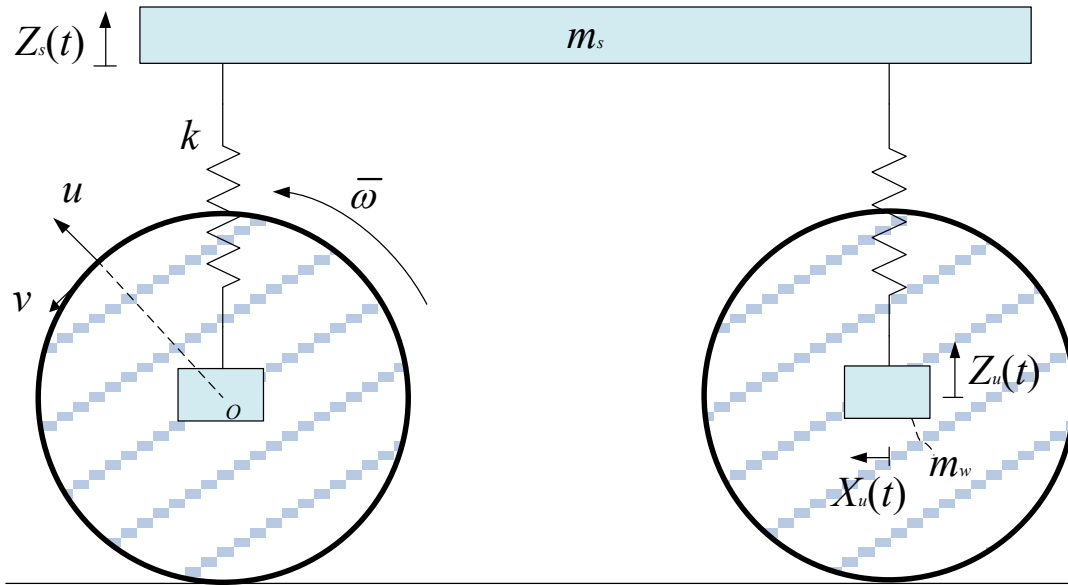


Figure 7.2 Two rotating tires combined with the vehicle body and the suspension system of the vehicle

- Using a half-car model with rotating tires.

The theory explained in the present thesis could be used in a half-car model as shown in Figure 7.2. Two rotating rings present the front and rear tires. The sprung mass could be modeled as a rigid bar with mass and moment of inertia. In an advance model, the rigid bar could be replaced by a flexible beam to take into account the deformations of the vehicle system. A reduced order finite element model of the vehicle body could also be used.

REFERENCES

- [1] K. Yi, J. K. Hedrick, “Observer-based identification of nonlinear system parameters,” *Journal of Dynamic Systems Measurement and Control*, 1995, Vol. 117, pp. 175–182.
- [2] C. Kim, P. I. Ro, “A sliding mode controller for vehicle active suspension systems with non-linearities,” *Proceedings of the Institution of Mechanical Engineers, Part D: Journal of Automobile Engineering*, 1998, Vol. 212, pp. 79–92.
- [3] C. Kim, P. I. Ro, H. Kim, “Effect of the suspension structure on equivalent suspension parameters,” *Proceedings of the Institution of Mechanical Engineers, Part D: Journal of Automobile Engineering*, Vol. 213, 1999, pp. 457–470.
- [4] L. Sun, “Optimum design of 'road-friendly' vehicle suspension systems subjected to rough pavement surfaces,” *Applied Mathematical Modelling*, Vol. 26, 2002, pp. 635–652.

- [5] L. Sun, T. W. Kennedy, "Spectral analysis and parametric study of stochastic pavement loads", *Journal of Engineering Mechanics*, ASCE, Vol. 128, 2002, pp. 318–327.
- [6] L. Sun, "Simulation of pavement roughness and IRI based on power spectral density," *Mathematics and Computers in Simulation*, Vol. 61, 2003, pp. 77–88.
- [7] K. S. Hong, D. S. Jeon, H. C. Sohn, "A new modeling of the Macpherson suspension system and its optimal pole-placement control", *Proceedings of the 7th Mediterranean Conference on Control and Automation (MED99)*, Haifa, Israel, 1999.
- [8] K. S. Hong, H. C. Sohn, J. K. Hedrick, "Modified Skyhook control of semi-active suspensions: A new model, gain scheduling, and hardware-in-the-loop tuning," *Journal of Dynamic Systems, Measurement, and Control*, Vol. 124, 2002, pp. 158–167.
- [9] M. S. Fallah, R. B. Bhat, W. F. Xie, "Influence of different semi-active control strategies on the performance of Macpherson suspension kinematic parameters," *SAE International Journal of Commercial Vehicles*, Vol. 1, 2009, pp. 222–229.
- [10] M. S. Fallah, R. B. Bhat, W. F. Xie, "New model and simulation of Macpherson suspension system for ride control applications," *Vehicle System Dynamics*, Vol. 47, 2009, pp. 195–220.
- [11] M. S. Fallah, R. B. Bhat, W. F. Xie, " H_∞ robust control of semi-active Macpherson suspension system: new applied design," *Vehicle System Dynamics*, Vol. 48, 2010, pp. 339–360.
- [12] M. S. Fallah, "New dynamic modeling and practical control design for Macpherson suspension system," PhD Thesis, 2010, Concordia University, Montreal, QC, Canada.

- [13] M. S. Fallah, R. B. Bhat, W. F. Xie, "Optimized control of semi-active suspension systems using H_∞ robust control theory and current signal estimation," *IEEE/ASME Transactions on Mechatronics*, (Article in Press)
- [14] K. Saeedi, R. J. Alkhoury, R. B. Bhat, A. K. W. Ahmed, "Ride dynamic analysis of a hybrid discrete and continuous vehicle model," *SAE Commercial Vehicle Engineering Congress & Exhibition*, October 2008, Rosemont, IL, USA.
- [15] B. Seba, N. Nedeljkovic, J. Paschedag, B. Lohmann, " H_∞ Feedback control and Fx-LMS feedforward control for car engine vibration attenuation," *Applied Acoustics*, Vol. 66, 2005, pp. 277–296.
- [16] C. Olsson, "Structure flexibility impacts on robust active vibration isolation using mixed sensitivity optimization," *Journal of Vibration and Acoustics*, Vol. 129, 2007, pp. 179–192.
- [17] C. Olsson, "Active automotive engine vibration isolation using feedback control," *Journal of Sound and Vibration*, Vol. 294, 2006, pp. 162–176.
- [18] S. Choi, S. Hong, K. Sung, J. Sohn, "Optimal control of structural vibrations using a mixed-mode magnetorheological fluid mount," *International Journal of Mechanical Science*, 2008, Vol. 50. pp. 559–567.
- [19] K. Saeedi, M. S. Fallah, R. B. Bhat, "Semi-active ride comfort evaluation of heavy vehicles using a hybrid dynamic model," *SAE World Congress*, April 2010, Detroit, MI, USA.
- [20] H. Dekker, "Vibrational resonances of nonrigid vehicles: Polygonization and ripple patterns," *Applied Mathematical Modelling*, Vol. 33, 2009, pp. 1349–1355.

- [21] F. R. Fassbender, C. W. Fervers, C. Harnisch, "Approaches to predict the vehicle dynamics on soft soil," *Vehicle System Dynamics*, Vol. 27, 1997, pp. 173–188.
- [22] S. Park, A. A. Popov, D. J. Cole, "Influence of soil deformation on off-road heavy vehicle suspension vibration," *Journal of Terramechanics*, Vol. 41, 2004, pp. 41–68.
- [23] R. N. Yong, M. A. Foda, "Tribology model for determination of shear stress distribution along the tyre-soil interface," *Journal of Terramechanics*, Vol. 27, 1990, pp. 93–114.
- [24] R. N. Yong, F. Eiyu, "Road surface roughness and tyre performance," *Journal of Terramechanics*, Vol. 27, 1990, pp. 219–239.
- [25] D. M. Xu, A. M. O. Mohamed, R. N. Yong, F. Caporuscio, "Development of a criterion for road surface roughness based on power spectral density function," *Journal of Terramechanics*, Vol. 29, 1992, pp. 477–486.
- [26] W. Soedel, "On the dynamic response of rolling tires according to thin shell approximations," *Journal of Sound and Vibration*, Vol. 41, 1975, pp. 233–246.
- [27] W. Soedel, M. G. Prasad, "Calculation of natural frequencies and modes of tires in road contact by utilizing eigenvalues of the axisymmetric non-contacting tire," *Journal of Sound and Vibration*, Vol. 70, 1980, pp. 573–584.
- [28] S. C. Huang, "Vibration of rolling tyres in ground contact," *International Journal of Vehicle Design*, Vol. 13, 1992, pp. 78–95.
- [29] C. J. Hunckler, T. Y. Yang, W. Soedel, "A geometrically nonlinear shell finite element for tire vibration analysis," *Computers & Structures*, Vol. 17, 1983, pp. 217–225.

- [30] Y. B. Chang, T. Y. Yang, W. Soedel, "Linear dynamic analysis of rotational shells using finite elements and modal expansion," *Journal of Sound and Vibration*, Vol. 86, 1983, pp. 523–538.
- [31] Y. B. Chang, T. Y. Yang, W. Soedel, "Dynamic analysis of a radial tire by finite elements and modal expansion," *Journal of Sound and Vibration*, Vol. 96, 1984, pp. 1–11.
- [32] L. E. Kung, W. Soedel, T. Y. Yang, L. T. Charek, "Natural frequencies and mode shapes of an automotive tire with interpretation and classification using 3-D computer graphics," *Journal of Sound and Vibration*, Vol. 102, 1985, pp. 329–346.
- [33] S. C. Huang, W. Soedel, "Effects of Coriolis acceleration on the free and forced in-plane vibrations of rotating rings on elastic foundation," *Journal of Sound and Vibration*, Vol. 115, 1987, pp. 253–274.
- [34] S. C. Huang, W. Soedel, "Response of rotating rings to harmonic and periodic loading and comparison with the inverted problem," *Journal of Sound and Vibration*, Vol. 118, 1987, pp. 253–270.
- [35] S. C. Huang, C. K. Su, "In-plane dynamics of tires on the road based on an experimentally verified rolling ring model," *Vehicle System Dynamics*, Vol. 21, 1992, pp. 247–267.
- [36] D. S. Stutts, W. Soedel, "A simplified dynamic model of the effect of internal damping on the rolling resistance in pneumatic tires," *Journal of Sound and Vibration*, Vol. 155, 1992, pp. 153–164.

- [37] J. Padovan, "Traveling waves vibrations and buckling of rotating anisotropic shells of revolution by finite elements," *International Journal of Solids and Structures*, Vol. 11, 1975, pp. 1367–1380.
- [38] J. Padovan, Natural frequencies of rotating prestressed cylinders, *Journal of Sound and Vibration*, Vol. 31, 1973, pp. 469–482.
- [39] J. Padovan, I. Zeid, "On the development of traveling load finite elements," *Computers & Structures*, Vol. 12, 1980, pp. 77–83.
- [40] J. Padovan, O. Paramodilok, "Generalized solution of time dependent traveling load problem via moving finite element scheme," *Journal of Sound and Vibration*, Vol. 91, 1983, pp. 195–209.
- [41] J. Padovan, "Finite element analysis of steady and transiently moving/rolling nonlinear viscoelastic structure-I. Theory," *Computers & Structures*, Vol. 27, 1987, pp. 249–257.
- [42] R. Kennedy, J. Padovan, "Finite element analysis of steady and transiently moving/rolling nonlinear viscoelastic structure-II. Shell and three-dimensional simulations," *Computers & Structures*, Vol. 27, 1987, pp. 259–273.
- [43] Y. Nakajima, J. Padovan, "Finite element analysis of steady and transiently moving/rolling nonlinear viscoelastic structure-III. Impact/contact simulations," *Computers & Structures*, Vol. 27, 1987, pp. 275–286.
- [44] R. A. Brockman, J. H. Champion, J. P. Medzorian, "Finite element analysis of tire critical speeds," *Computers & Structures*, Vol. 43, 1992, pp. 581–593.
- [45] P. W. A. Zegelaar, H. B. Pacejka, "In-plane dynamics of tyres on uneven roads," *Vehicle System Dynamics*, Vol. 25, 1996, pp. 714–730.

- [46] K. Iwao, I. Yamazaki, "A study on the mechanism of tire/road noise," *JSAE review*, Vol. 17, 1996, pp. 139–144.
- [47] G. J. Kim, K. R. Holland, N. Lalor, "Identification of the airborne component of tyre-induced vehicle interior noise," *Applied Acoustics*, Vol. 51, 1997, pp. 141–56.
- [48] R. J. Pinnington, A. R. Briscoe, "A wave model for a pneumatic tyre belt," *Journal of Sound and Vibration*, Vol. 253, 2002, pp. 941–959.
- [49] G. Dihua, S. Jin, L. H. Yam, "Establishment of model for Tire steady state cornering properties using experimental modal parameters," *Vehicle System Dynamics*, Vol. 34, 2000, pp. 43–56.
- [50] G. Dihua, F. Chengjian, "Tire modeling for vertical properties including enveloping properties using experimental modal parameters," *Vehicle System Dynamics*, Vol. 40, 2003, pp. 419–433.
- [51] L. H. Yam, D. H. Guan, A. Q. Zhang, "Three-dimensional mode shapes of a tire using experimental modal analysis," *Experimental Mechanics*, Vol. 40, 2000, pp. 369–375.
- [52] F. Chengjian, G. Dihua, "The quantitative analysis and experimental verification of the tire static enveloping model using experimental modal parameters," *Vehicle System Dynamics*, Vol. 44, 2006, pp. 675–688.
- [53] J. M. Muggleton, B. R. Mace, M. J. Brennan, "Vibrational response prediction of a pneumatic tyre using an orthotropic two-plate wave model," *Journal of Sound and Vibration*, Vol. 264, 2003, pp. 929–950.
- [54] S. Bashmal, R. Bhat, S. Rakheja, "In-plane free vibration analysis of an annular disk with point elastic support," *Shock and Vibration*, Vol. 18, 2011, pp. 627–640.

- [55] S. Bashmal, R. Bhat, S. Rakheja, "Analysis of in-plane modal characteristics of an annular disk with multiple point supports," ASME International Mechanical Engineering Congress and Exposition, Proceedings, IMECE2009, Vol. 15, pp. 321–329.
- [56] S. Bashmal, R. Bhat, S. Rakheja, "In-plane free vibration of circular annular disks," *Journal of Sound and Vibration*, Vol. 322, 2009, pp. 216–226.
- [57] S. Bashmal, R. Bhat, S. Rakheja, "Experimental studies on the in-plane vibrations and sound radiation in an annular thick disk," *Canadian Acoustics*, Vol. 37, 2009, pp. 202–203.
- [58] S. Bashmal, R. Bhat, S. Rakheja, "Frequency equations for the in-Plane vibration of circular annular disks," *Advances in Acoustics and Vibration*, Vol. 2010, Article ID 501902, 8 pages.
- [59] J. S. Bolton, H. J. Song, Y. K. Kim, Y. J. Kang, "The wave number decomposition approach to the analysis of tire vibration," *Proceedings of NOISE-CON 98*, 1998, pp. 97–102.
- [60] Y. J. Kim, J. S. Bolton, "Effects of rotation on the dynamics of a circular cylindrical shell with application to tire vibration," *Journal of Sound and Vibration*, Vol. 275, 2004, pp. 605–621.
- [61] L. Jia, Y. Xu, J. Zhang, "Free vibration analysis of radial pneumatic tires using Bézier functions," *Journal of Sound and Vibration*, Vol. 285, 2005, pp. 887–903.
- [62] O. Civalek, "A parametric study of the free vibration analysis of rotating laminated cylindrical shells using the method of discrete singular convolution," *Thin-Walled Structures*, Vol. 45, 2007, pp. 692–698.

- [63] O. Civalek, M. Gürses, “Free vibration analysis of rotating cylindrical shells using discrete singular convolution technique,” *International Journal of Pressure Vessels and Piping*, Vol. 86, 2009, pp. 677–683.
- [64] E. Rustighi, S. J. Elliott, “Stochastic road excitation and control feasibility in a 2D linear tyre model,” *Journal of Sound and Vibration*, Vol. 300, 2007, pp. 490–501.
- [65] E. Rustighi, S. J. Elliott, S. Finnveden, K. Gulyás, T. Mócsai, M. Danti, “Linear stochastic evaluation of tyre vibration due to tyre road excitation” *Journal of Sound and Vibration*, Vol. 310, 2008, pp. 1112–1127.
- [66] B. S. Kim, G. J. Kim, T. K. Lee, “The identification of sound generating mechanisms of tyres,” *Applied Acoustics*, Vol. 68, 2007, pp. 114–133.
- [67] J. C. Delamotte, R. F. Nascimento, J. R. F. Arruda, “Simple models for the dynamic modeling of rotating tires,” *Shock and Vibration*, Vol. 15, 2008, pp. 383–393.
- [68] P. Kindt, P. Sas, W. Desmet, “Development and validation of a three-dimensional ring-based structural tyre model,” *Journal of Sound and Vibration*, Vol. 326, 2009, pp. 852–869.
- [69] F. Wullens, W. Kropp, “A three-dimensional contact model for tyre/road interaction in rolling conditions,” *Acta Acoustica United with Acoustica*, Vol. 90, 2004, pp. 702–711.
- [70] F. Wullens, W. Kropp, “Wave content of the vibration field of a rolling tyre,” *Acta Acoustica United with Acoustica*, Vol. 93, 2007, pp. 48–56.

- [71] J. Périssé, “A study of radial vibrations of a rolling tyre for tyre-road noise characterisation,” *Mechanical Systems and Signal Processing*, Vol. 16, 2002, pp. 1043–1058.
- [72] M. Brinkmeier, U. Nackenhorst, S. Petersen, O. V. Estorff, “A finite element approach for the simulation of tire rolling noise,” *Journal of Sound and Vibration*, Vol. 309, 2008, pp. 20–39.
- [73] U. Nackenhorst “The ALE-formulation of bodies in rolling contact: Theoretical foundations and finite element approach,” *Computer Methods in Applied Mechanics and Engineering*, Vol. 193, 2004, pp. 4299–4322.
- [74] I. Lopez, R. E. A. Blom, N. B. Roozen, H. Nijmeijer, “Modelling vibrations on deformed rolling tyres - a modal approach,” *Journal of Sound and Vibration*, Vol. 307, 2007, pp. 481–494.
- [75] I. Lopez, R. R. J. J. van Doorn, R. van der Steen, N. B. Roozen, H. Nijmeijer, “Frequency loci veering due to deformation in rotating tyres,” *Journal of Sound and Vibration*, Vol. 324, 2009, pp. 622–639.
- [76] Z. Geng, A. A. Popov, D. J. Cole, “Modelling of vibration damping in pneumatic tyres: Appropriate interpretation of complex modes,” *Proceedings of the 2002 International Conference on Noise and Vibration Engineering (ISMA)*, 2002, pp. 485–494.
- [77] Z. Geng, A. A. Popov, D. J. Cole, “Measurement, identification and modelling of damping in pneumatic tyres,” *International Journal of Mechanical Sciences*, Vol. 49, 2007, pp. 1077–1094.

- [78] P. Kindt, F. De Coninck, P. Sas, W. Desmet, "Analysis of tire/road noise caused by road impact excitations," *Proceedings of the International Styrian Noise, Vibration & Harshness Congress*, Graz, Austria, 2008, pp. 113–134.
- [79] P. Kindt, P. Sas, W. Desmet, "Test setup for tire/road noise caused by road impact excitations," *Proceedings of the Tire Technology Expo 2007 Conference*, Köln, Germany, 2007, pp. 13–15.
- [80] P. Kindt, P. Sas, W. Desmet, "Measurement and analysis of rolling tire vibrations," *Optics and Lasers in Engineering*, Vol. 47, 2009, pp. 443–453.
- [81] P. Kindt, D. Berckmans, F. De Coninck, P. Sas, W. Desmet, "Experimental analysis of the structure-borne tyre/road noise due to road discontinuities," *Mechanical Systems and Signal Processing*, Vol. 23, 2009, pp. 2557–2574.
- [82] P. Sabiniarz, W. Kropp, "A waveguide finite element aided analysis of the wave field on a stationary tyre, not in contact with the ground," *Journal of Sound and Vibration*, Vol. 329, 2010, pp. 3041–3064.
- [83] D. Zimmer, M. Otter, "Real-time models for wheels and tyres in an object-oriented modelling framework," *Vehicle System Dynamics*, Vol. 48, 2010, pp. 189–216.
- [84] D. Allaei, W. Soedel, T. Y. Yang, "Natural frequencies and modes of rings that deviate from perfect axisymmetry," *Journal of Sound and Vibration*, Vol. 111, 1986, pp. 9–27.
- [85] D. Allaei, W. Soedel, T. Y. Yang, "Eigenvalues of rings with radial spring attachments," *Journal of Sound and Vibration*, Vol. 121, 1988, pp. 547–561.
- [86] D. Allaei, W. Soedel, T. Yang, "Vibration analysis of non-axisymmetric tires," *Journal of Sound and Vibration*, Vol. 122, 1988, pp. 11–29.

- [87] D. S. Stutts, C. M. Krousgrill, W. Soedel, "Parametric excitation of tire-wheel assemblies by a stiffness non-uniformity," *Journal of Sound and Vibration*, Vol. 179, 1995, pp. 499–512.
- [88] C. H. J. Fox, "A simple theory for the analysis and correction of frequency splitting in slightly imperfect rings," *Journal of Sound and Vibration*, Vol. 142, 1990, pp. 227–243.
- [89] A. K. Rourke, S. McWilliam, C. H. J. Fox, "Multi-mode trimming of imperfect rings," *Journal of Sound and Vibration*, Vol. 248, 2001, pp. 695–724.
- [90] A. K. Rourke, S. McWilliam, C. H. J. Fox, "Multi-mode trimming of imperfect thin rings using masses at pre-selected locations," *Journal of Sound and Vibration*, Vol. 256, 2002, pp. 319–345.
- [91] R. Eley, C. H. J. Fox, S. McWilliam, "Coriolis coupling effects on the vibration of rotating rings," *Journal of Sound and Vibration*, Vol. 238, 2000, pp. 459–480.
- [92] S. McWilliam, J. Ong, C. H. J. Fox, "On the statistics of natural frequency splitting for rings with random mass imperfections," *Journal of Sound and Vibration*, Vol. 279, 2005, pp. 453–470.
- [93] P. Bisegna, G. Caruso, "Frequency split and vibration localization in imperfect rings," *Journal of Sound and Vibration*, Vol. 306, 2007, pp. 691–711.
- [94] B. L. Dillinger, N. Jalili, I. Ul-Haque, "Analytical modelling and experimental verification of tyre non-uniformity," *International Journal of Vehicle Design*, 2008, Vol. 46, pp. 1–22.

- [95] L. E. Kung, W. Soedel, T. Y. Yang, "Free vibration of a pneumatic tire-wheel unit using a ring on an elastic foundation and a finite element model," *Journal of Sound and Vibration*, Vol. 107, 1986, pp. 181–194.
- [96] L. E. Kung, W. Soedel, T. Y. Yang, "On the dynamic response at the wheel axle of a pneumatic tire," *Journal of Sound and Vibration*, Vol. 107, 1986, pp. 195–213.
- [97] L. E. Kung, W. Soedel, T. Y. Yang, "On the vibration transmission of a rolling tire on a suspension system due to periodic tread excitation," *Journal of Sound and Vibration*, Vol. 115, 1987, pp. 37–63.
- [98] S. C. Huang, B. S. Hsu "An approach to the dynamic analysis of rotating tire-wheel-suspension units," *Journal of Sound and Vibration*, Vol. 156, 1992, pp. 505–519.
- [99] J. Padovan, A. Kazempour, "Multibody instantly centered moving lagrangian observer schemes-Part I. Formulation," *Computers & Structures*, Vol. 32, 1989, pp. 93–100.
- [100] A. Kazempour, J. Padovan, "Multibody instantly centered moving lagrangian observer schemes-Part II. Application to vehicular simulations," *Computers & Structures*, Vol. 32, 1989, pp. 101–111.
- [101] J. Padovan, A. Kazempour, F. Tabaddor, B. Brockman, "Alternative formulations of rolling contact problems," *Finite Elements in Analysis and Design*, Vol. 11, 1992, pp. 275–284.
- [102] C. R. Dohrmann "Dynamics of a tire wheel suspension assembly," *Journal of Sound and Vibration*, Vol. 210, 1998, pp. 627–642.
- [103] T. K. Lee, B. S. Kim, "Vibration analysis of automobile tire due to bump impact," *Applied Acoustics*, Vol. 69, 2008, pp. 473–478.

- [104] M. J. MohdNor, M. H. Fouladi, H. Nahvi, A. K. Ariffin, "Index for vehicle acoustical comfort inside a passenger car," *Applied Acoustics*, Vol. 69, 2008, pp. 343–353.
- [105] H. Nahvi, M. H. Fouladi, M. J. MohdNor, "Evaluation of whole-body vibration and ride comfort in a passenger car," *International Journal of Acoustics and Vibrations*, Vol. 14, 2009, pp. 143–149.
- [106] M. H. Fouladi, M. J. Mohd Nor, O. Inayatullah, A. Kamal, "Evaluation of seat vibration sources in driving condition using spectral analysis," *Journal of Engineering Science and Technology*, Vol. 6, 2011, pp. 342–358.
- [107] V. N. Nguyen, S. Inaba, "Effects of tire inflation pressure and tractor velocity on dynamic wheel load and rear axle vibrations," *Journal of Terramechanics*, Vol. 48, 2011, pp. 3–16.
- [108] W. Soedel, "Vibration of Shells and Plates", Third Edition, Marcel Dekker Inc., New York, 2004.
- [109] W. T. Thomson, M. D. Dahleh, "Theory of Vibration with Applications," Fifth Edition, Prentice Hall, New Jersey, 1998.
- [110] K. S. Hong, D. S. Jeon, W. S. Yoo, H. Sunwoo, S. Y. Shin, C. M. Kim, B. S. Park, "A new model and an optimal pole-placement control of the Macpherson suspension system," SAE International Congress and Exposition, Detroit, MI, SAE paper No. 1999-01-1331, pp. 267–276.
- [111] W. L. Cleghorn, B. Tabarrok, T. W. Lee, "Vibration of rings with unsymmetrical cross sections: a finite element approach," *Journal of Sound and Vibration*, Vol. 168, 1993, pp. 93–113.